Towards the Development of a Prototype Ion Mobility Spectrometer

by

Daniel Rickert

A thesis

presented to the University of Waterloo

in fulfillment of the

thesis requirement for the degree of

Doctor of Philosophy

in

Chemistry

Waterloo, Ontario, Canada, 2024

Examining Committee Membership

The following served on the Examining committee for this thesis. The decision of the examining committee is by majority vote.

External Examiner	Prof. Brian Clowers Professor Department of Chemistry, Washington State University
Supervisor	Prof. Janusz Pawliszyn University Professor Department of Chemistry, University of Waterloo
Supervisor	Prof. W. Scott Hopkins Associate Professor Department of Chemistry, University of Waterloo
Internal Member	Prof. Germán Sciaini Associate Professor Department of Chemistry, University of Waterloo
Internal Member	Dr. Larry Campbell Adjunct Professor Department of Chemistry, University of Waterloo
Internal/External Member	Prof. Jim Martin Associate Professor Department of Physics, University of Waterloo

Author's Declaration

I hereby declare that I am the sole author of this thesis. This is a true copy of the thesis, including any required final revisions, as accepted by my examiners.

I understand that my thesis may be made electronically available to the public.

Abstract

Ion mobility spectrometry (IMS) is an analytical technique that separates ions in the gas-phase based on differences in their mobility under the influence of an electric field. In traditional drift-tube IMS systems, an axial DC electric field pushes ions through a static bath gas, and the different ion subpopulations achieve averaged steady-state drift velocities that are dependent on their shape and size. Mobility separation is achieved due to multiple collisions between the molecular ions and gas molecules. Smaller, more compact ions will collide less frequently with the buffer gas in comparison to larger, more elongated ions. Consequently, the smaller ions have higher mobilities and therefore reach the detector faster. One of the most recent developments in IMS, which is referred to as trapped ion mobility spectrometry (TIMS) was reported first in 2011 by Park and coworkers. In contrast to the conventional drift tube approach described above, in the TIMS configuration, ions are trapped axially by balancing an applied DC electric field gradient against a parallel flow of neutral carrier gas flowing towards the detector. A radiofrequency induced quadrupolar field radially confines ions in the center of the TIMS separation region. Trapped ions are focused first and then eluted towards the mass analyzer from the separation region based on differences in their mobility by gradually reducing the electric field strength.

The research described in this thesis covers the development and characterization of a prototype ion mobility spectrometer designed to improve upon the existing TIMS platform. This instrument, referred to as a variable flow trapped ion mobility spectrometer (vfTIMS), has a segmented mobility separation region comprised of four sectors with decreasing inner diameter. A gas flow velocity gradient that is generated through the decreasing sectors of the mobility region can be harnessed for high-resolution separations. Another improvement compared to the conventional TIMS is instead of a quadrupolar radially confining field, the vfTIMS employs a hexapolar field for improved ion focusing and increased ion capacity. Additionally, the DC electric field gradient that traps the ions is completely customizable by utilizing individually addressable electrodes, so the profile is not limited to a simple linear field gradient.

The main research objectives of this thesis are as follows:

1. Construct a prototype ion mobility spectrometer, combining multiple commercial and in-house components.
2. Implement an improved electrical layout to drive the instrument, with the added ability to define all the electric fields within the analyzer.
3. Fully characterize the performance of the prototype instrument for ion trapping and ion mobility separation.

In summary, this thesis aims to address the above objectives described in the chapters that make up its content. Chapter 2 and Chapter 3 focus on the design and construction of the vfTIMS. More specifically, Chapter 2 outlines the various hardware components of the vfTIMS that were either designed and built in-house or purchased commercially and modified. Chapter 3 details the design and testing of the electronics that power the system, along with the development of the user interface to control the instrument. Chapter 4 presents the extensive experimental optimization that was completed to get the instrument operational. Additionally, Chapter 4 also covers the experimental results that establish a baseline set of instrumental conditions that should be used for more complex experiments. Chapter 5 describes the first two proof of concept studies that demonstrate the feasibility of ion mobility separation experiments on the vfTIMS, building on the knowledge gleaned from the experiments in Chapter 4. Lastly, Chapter 6 serves as a roadmap for what must be done next to advance the project, in both the short term as well as the longer term.

Acknowledgements

I would like to take this opportunity to express my immense gratitude and appreciation to all who have supported and helped me throughout my PhD.

Firstly, I would like to thank my supervisors, Professor Janusz Pawliszyn and Professor Scott Hopkins. Professor Pawliszyn – you gave me the resources and opportunity to work on a unique project, and always pushed me to think critically and systematically. Thank you for your constructive feedback and support throughout my PhD. Scott – you have been an amazing mentor, role model, and supervisor. Thank you for all of your guidance and patience. Your steadfast support when I was struggling through the tough times with this project was so vital for me to reach this point. You have played a crucial role in shaping the scientist I am today.

Next, I would like to thank the members of my PhD advisory committee, Prof. Terry McMahon, Prof. Germán Sciaini, Dr. Larry Campbell, and Prof. Jim Martin. Your time, energy, and valuable advice over the past five years have been instrumental. A special thanks to my external examiner, Prof. Brian Clowers, for accepting the invitation to evaluate my work and review my thesis.

To my friends and colleagues in the Pawliszyn and Hopkins research groups, your support has meant the world to me. Dr. Neville Coughlan, Dr. Victor Galievsky, Dr. Alexander Haack, Dr. Christian Ieritano, Dr. Khaled Murtada, Dr. Emir Nazdrajic, Dr. Nando Rosales, Chris Ryan, Dr. Varoon Singh, Cailum Steinstra, Patrick Thomas, and others – thank you so much.

I am especially grateful to Hiruy Haile and Krunomir Dvorski from the University of Waterloo Science Technical Services Electronics Shop and Machine Shop for their invaluable help and assistance throughout my degree. Thanks also to Gordon Anderson and the GAA Custom Electronics team; without your guidance and the many Friday update meetings, this project would not have been possible.

My deepest appreciation goes to my amazing parents, Andrew and Jennifer; my brothers, Stephen and Brian; my dearest friends, Mack, Shayan, Jeremy, and Aaron; and my in-laws, Mary and Paul. Your love and unwavering support have been my anchor throughout this journey, and I am truly grateful.

Finally, a special thank you to my wife, Maggie. Your encouragement, reassurance, and belief in me are just some of the reasons why I was able to persevere and make it to the finish line. Reflecting on our journey from the tiny 1-bedroom apartment on Albert Street at the start of my PhD to where we are now is truly remarkable. I am so excited about the next chapter in our lives. I love you more than words can express.

And of course, I can't forget about my dog, Marvin – equal parts menace and marvel. Marvin sat in my office every day and kept me company while I wrote this dissertation. Going to the park to play fetch with his favourite orange ball, or out for a walk in our neighbourhood watching him try to hunt squirrels, proved to be the best way to clear my mind and come up with new ideas for my thesis.

Thank you everyone for playing your part in my PhD – it truly does take a village.

Dedication

This thesis is dedicated to my family, my friends, and my wife, Maggie. Thank you for everything you have done for me. Without all of you, this thesis would not have been possible.

"Made weak by time and fate, but strong in will

To strive, to seek, to find, and not to yield"

– Alfred, Lord Tennyson

Table of Contents

List of Figures

List of Tables

List of Abbreviations

ADC	analog to digital converter
APPI	atmospheric pressure photoionization
CCS	collision cross section
CID	collision induced dissociation
CIU	collision induced unfolding
DTIMS	drift tube ion mobility spectrometry
EFG	electric field gradient
ESI	electrospray ionization
FFT	fast Fourier transform
FTICR	Fourier transform ion cyclotron resonance mass spectrometry
GUI	graphical user interface
I.D.	inner diameter
IMS	ion mobility spectrometry
LC	liquid chromatography
LIT	linear ion trap
MALDI	matrix assisted laser desorption ionization
MeOH	methanol
MIPS	modular intelligent power source
MS	mass spectrometry

nanoESI	nanoelectrospray ionization
O.D.	outer diameter
PCB	printed circuit board
QIT	quadrupole ion trap
QTOF	quadrupole – time of flight
RF	radio frequency
SID	surface induced dissociation
SLPM	standard litres per minute
TAA	tetraalkylammonium
TAA12	tetradodecyl ammonium
TAA5	tetrapentyl ammonium
TAA8	tetraoctyl ammonium
TIMS	trapped ion mobility spectrometry
UV	ultraviolet
UVPD	ultraviolet photodissociation
vfTIMS	variable flow trapped ion mobility spectrometry

Chapter 1: Introduction/Literature Review

1.1 Preamble

This thesis describes the design, development, and characterization of a prototype ion mobility spectrometer designed to improve upon the existing trapped ion mobility spectrometry (TIMS) platform. In conventional ion mobility spectrometry (IMS) instruments, such as drift tubes, ions are propelled through a static buffer gas by an electric field, with the ion's velocity dependent on its orientationally averaged projection cross section (*e.g.*, collision cross-section). TIMS on the other hand, inverts this approach. A flowing buffer gas pushes the ions through a linearly increasing electrical field gradient, and the ions are trapped axially when the force of the gas balances the equal and opposite force applied by the electric field. To "elute" the trapped ions, the field strength is incrementally decreased, such that the force exerted by the buffer gas can eventually overcome the trapping force exerted by the field.

A PhD research project concentrated on instrument development is somewhat unconventional in the sense that the instrument must be designed and built before experiments can be performed. This dissertation is structured in such a way that the examining committee can follow the journey from the initial conception of the idea behind the instrument, to building the physical prototype in the lab, the extensive testing, troubleshooting, and experimental optimization, before finally closing with a perspective on the steps that need to be taken to continue to advance the project. The thesis is organized as follows: Chapter 1 begins by delving into the historical background and the fundamental principles that underpin IMS. This is followed by a comprehensive examination of the core fundamentals of TIMS, different calibration strategies for experimentally determining mobilities and collision cross-sections, various instrumental configurations that have been reported, and a curated review of recent literature featuring different applications that utilize the TIMS technology. Chapter 2 provides a detailed account of the commercial and in-house hardware used to construct the instrument accompanied by an *in-silico* assessment of the gas dynamics and flow profiles. Chapter 3 outlines the electrical components driving the system and includes a second *in-silico* study

focusing on the electric fields generated within the instrument. Chapter 4 presents the results of experimental optimization and the characterization of the prototype's performance, while Chapter 5 outlines two proof-of-concept studies that provide initial evidence of ion mobility separation. The final chapter begins with the short-term and medium-term "next steps" that are essential for advancing the project, before concluding with a broad discussion of the future perspectives and possibilities once the instrument has been fully developed.

1.2 Introduction to Ion Mobility Spectrometry

The earliest report describing the motion of ions through gas was published by Rutherford and Thomson in 1896.[1] Several years later, Thomson published a mathematical treatment detailing how ions move through a gas.[2] Following this breakthrough, in 1905, the French physicist Paul Langevin published a more comprehensive study of the motion of ions in an electric field.[3–5] His early research laid the groundwork for Langevin's kinetic theory and became the foundation of IMS as it is known today.[6] Nearly 70 years after Langevin first considered the problem of diffusion and applied it to the mobility of ions, Cohen and Karasek introduced the first commercial IMS instrument in 1970, under the name plasma chromatography.[7] Their technology, which was partly developed at the University of Waterloo in the Department of Chemistry, demonstrated that gas phase ions could be mobilized, and ultimately separated, through a neutral buffer gas, via an applied electric field. Since then, and particularly over the last 20 years, IMS has become one of the preeminent techniques, behind only mass spectrometry, for analyzing ions in the gas phase.

In a traditional IMS instrument, referred to as a drift tube, ions are exposed to a linear and constant weak electric field that drives them axially through a static bath gas (Figure 1-1).[8,9] The different ion subpopulations achieve averaged steady-state drift velocities that are dependent on their shape and size. Separation is achieved due to multiple collisions between the molecular ions and gas molecules. Smaller, more compact ions will collide less frequently (and also less energetically) with the buffer gas than larger, more elongated ions.[10,11] Consequently, the smaller ions are more mobile and reach the detector faster. In a drift tube IMS (DTIMS) instrument, ions are pulsed into the drift region using an electrostatic gate (or series

of gates), and the duration of time for ions to reach the detector (Faraday plate, mass spectrometer, *etc*.) is measured. The ion's drift velocity (v_d) as it travels through the buffer gas in the drift cell is the product of the weak electric field (E, V cm^{-1}) and the proportionality factor (K, cm^2 s^{-1} V^{-1}) which is the ion mobility.[9]

$$\boldsymbol{v_d = KE} \qquad \textbf{(1-1)}$$

Alternatively, K can also be considered as the measurement of the friction force exerted from collisions between the bath gas and the ion that is linked by an observable quantity: the time needed for an ion to traverse the length of the drift region driven by the electric field. [10]

A first approximation of the ion mobility is achieved by normalizing K to the reduced mobility K_0, where T (K) is the absolute temperature and P (Torr) is pressure. The mobility of an ion is directly linked to the rate at which it collides with the bath gas, so it is necessary to integrate the standard temperature (273.15 K) and pressure (760 Torr) into the reduced mobility expression since the rate of collisions scales linearly with the bath gas number density. By normalizing K to K_0, comparisons can be made between mobility measurements taken on different instruments.[10]

$$\boldsymbol{K_0 = K\left(\frac{P}{760\ Torr}\right)\left(\frac{273.15\ K}{T}\right)} \qquad \textbf{(1-2)}$$

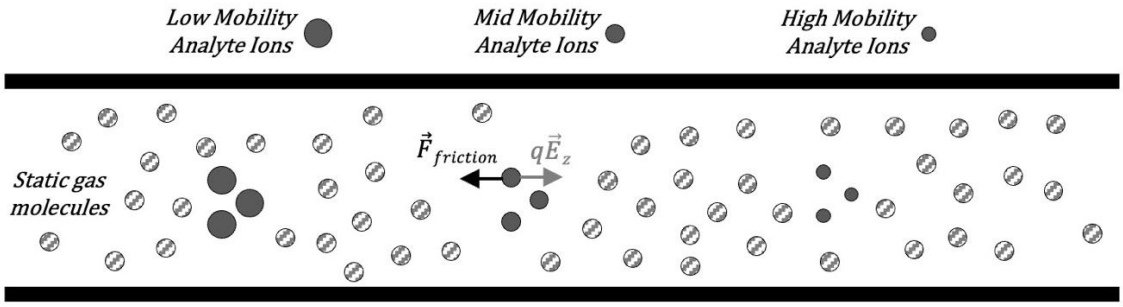

Figure 1-1. Simplified schematic of a DTIMS instrument. The drift force applied to the ions by the electric field propels them through the static bath gas with a drift velocity proportional to the ion mobility. A drift tube operates at a constant electric field strength ($\boldsymbol{E_z}$). The friction ($\boldsymbol{F_{friction}}$) forces exerted by collisions with the gas molecules result in separation of different ions based on differences in their mobility ($\boldsymbol{K}$).

The mobility can also be derived from the momentum transfer collision integral ($\Omega(T)$), which is more commonly referred to as the collision-cross section (CCS).[12,13] The collision integral considers the

momentum transfer between the ion and the gas molecules averaged over all gas-ion relative thermal velocities.[10,12–15] The Mason-Schamp equation defines how *K* can be calculated using the momentum transfer collision integral ($\Omega(T)$, $Å^2$) for atomic species:

$$\boldsymbol{K = \frac{3ze}{16N}\sqrt{\frac{2\pi}{\mu k_B T}}\left(\frac{1}{\Omega(T)}\right)} \qquad \textbf{(1-3)}$$

Where *z* is the number of elementary charges on the ion, *e* is the electronic charge, *N* is the number density of the bath gas, μ is the reduced mass of the ion and the gas ($\mu = \frac{Mm}{M+m}$; *m* is the mass of the bath gas, *M* is the mass of the ion), k_B is Boltzmann's constant, and *T* is temperature. If the mobility of the molecular ion is known, then the Mason-Schamp equation can be rearranged to solve for the CCS. The CCS can be considered the physical encoding of the three-dimensional shape of the ion and is dependent on the molecular structure and the composition of the bath gas.[9–11] This is a unique descriptor of an ion and can be used to differentiate two isobaric (*e.g.*, same mass to charge ratio (*m/z*)) species that cannot be resolved by a mass spectrometric measurement alone. An important caveat to the Mason-Schamp equation is that the relationship only holds true when the field induced kinetic energy is much lower than the thermal energy of the ions. In other words, the thermal velocities of the ions follow a Maxwell-Boltzmann distribution set by the temperature of the bath gas.[16,17] This is referred to as the low-field limit. However, as the ion's drift velocity increases, either by increasing the magnitude of the electric field or reducing the pressure in the analyzer (*e.g.*, decreasing the number of gas molecules which decreases the number of collisions), the field-induced kinetic energy increases and becomes more significant. The low-field limit means that the reduced electric field (*E/N*), represented in Townsends (Td), is low enough that the reduced mobility, K_0, is independent of *E/N*. Generally, the low-field limit is < 10 Td.[11] A discussion regarding the impact of the low-field limit on calibrating IMS measurements for different instruments such as the TIMS will be covered in Section 1.4.

1.3 Fundamentals of Trapped Ion Mobility Spectrometry

As the IMS technology became more widespread throughout the 1990's, more complex IMS instruments were developed that hybridized the IMS analyzer with conventional mass spectrometers (MS). By coupling an IMS analyzer "in series" before the MS detector, isobaric/isomeric ions that cannot be distinguished solely by *m/z* will be initially separated based on differences in their mobility (*K*), prior to mass spectrometric detection. For example, this hybridized approach is can be very useful in situations where a background interference ion has the same *m/z* as an analyte of interest. Using the MS on its own, there is no way to discriminate between the two species. However, if the IMS cell can separate the two ions first in the mobility dimension, the analyte of interest can be accurately detected by the MS. Many of these hybrid instruments began to incorporate radio-frequency (RF) confinement in the ion optics (*i.e.*, ion funnel) that guide ions through the differential vacuum pumping stages of the instrument, and to minimize the effects of radial diffusion on the ion cloud.[18–22] Not long after, RF-confining DTIMS instruments, more commonly referred to as electrodynamic DTIMS, began to utilize this new technology to radially focus ions during mobility analysis.[23] However, limitations still existed since the diffusion coefficient is inversely proportional to the pressure, and simultaneously, the pressure directly affects whether the instrument can operate below the low field limit.[23,24] In 2011, Park and co-workers introduced the TIMS, which built on many of these instrumental advances over the preceding 20 years.[25,26] The operating principle in TIMS is that ions are pushed through the mobility region by a flowing column of gas and are trapped when the force exerted by the gas matches the opposing force applied by the electric field. Ions with differing mobilities are trapped axially at different locations in the analyzer, and as the magnitude of the electric field is decreased, the ions "elute" and transit to the detector.[27] Somewhat simplistically, the TIMS can be considered as an inverted DTIMS.[28] In both instruments, separation is achieved due to collisions between the carrier gas and the ions. This is denoted in Figure 1-1 and Figure 1-2 as the friction force ($F_{friction}$). However, in the case of the TIMS, the ions are trapped by the electric field (E_z) while being pushed by the gas, as opposed to the drift tube which uses the electric field to propel the ions through the static bath gas.

Interestingly, the idea of using opposing forces to separate ions was first described in 1898 by John Zeleny.[29] Zeleny built an apparatus to hold ions with different mobilities stationary against a counter flow of gas, however, his work was abandoned and forgotten for nearly a century. More recently, throughout the 1990s, several capillary electrophoresis (*e.g.,* liquid-phase IMS) techniques were reported that used a similar "opposing forces" approach to focus and separate ions in the solution-phase. For example, a capillary electrophoresis experiment using a tapered channel with whole column imaging detection was reported in literature. This system was able to investigate the focusing and separation process of proteins by using pH and electric field gradients created in the Tris buffer solution contained in a conical capillary.[30,31] Another capillary electrophoresis method that applied electric fields gradients similar to TIMS, referred to as electric field gradient focusing, employed a similar concept by using an electric field to hold charged protein ions stationary against a flowing buffer solution.[32] However these approaches were not very practical as the electric field gradients generated temperature gradients in the system which led to convection currents that broaden the separation zone resulting in poor resolution and reproducibility.

1.3.1 General Overview of TIMS

The TIMS analyzer is comprised of a series of segmented ring electrodes that form three regions: the entrance funnel, the TIMS tunnel, and the exit funnel. All three regions are enclosed in a vacuum chamber interfaced in the first pumping stage of a MS, and for most applications the TIMS analyzer is operated at a pressure of ~ 3 mbar.[27,33] Ions are generated at atmospheric pressure through a variety of mechanisms, including electrospray ionization (ESI),[34] nanoelectrospray ionization (nanoESI), matrix assisted laser desorption ionization (MALDI),[35] or atmospheric pressure photoionization (APPI),[36] however, most applications employ nanoESI.[18] Following ionization, molecular ions exiting the transfer capillary are pulsed by an electrostatic deflector plate into the entrance funnel that radially focuses the ion beam prior to entry into the TIMS tunnel. The flow of gas exiting the end of the transfer capillary is also directed through the TIMS tunnel where it is pumped away by a vacuum port installed in the exit funnel region. By varying the degree of pumping between the port in the exit funnel region, and an additional pumping port in the

entrance funnel region, the velocity of the gas and the pressure differential are accurately controlled. Since the reduced electric field relies on the gas number density, the *E/N* can be tuned with a high degree of accuracy within the TIMS analyzer. It has been reported in literature that it is possible to operate the TIMS at similar gas velocities and pressures to produce identical *E/N* values to those in DTIMS instruments. However optimal performance is achieved when operating at higher gas velocities with *E/N* values in the range of 45 to 150 Td.[10,11,18]

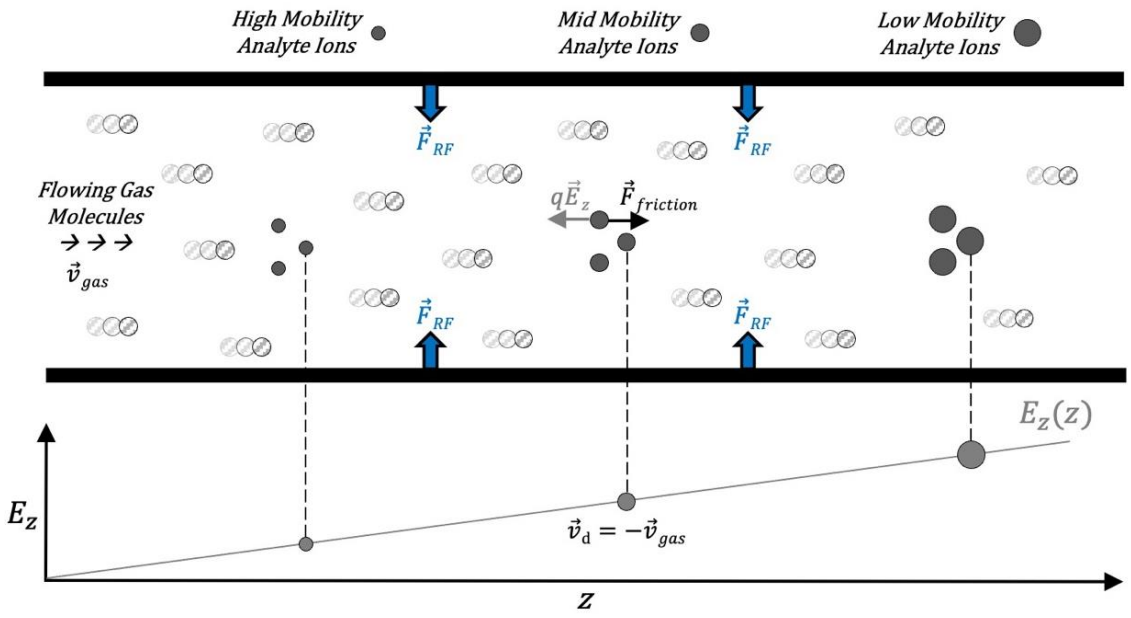

Figure 1-2. Visualization of the ion trapping mechanism utilized in a TIMS instrument. Ions are pushed through the analyzer by the friction force ($\boldsymbol{F_{Friction}}$) exerted by the flowing gas, while the force exerted by the electric field opposes the ion's forward movement. Ions are trapped along the axial electric field gradient when the drift velocity ($\boldsymbol{v_d}$) is equal and opposite to the gas velocity ($\boldsymbol{v_{gas}}$). The force exerted by the RF field ($\boldsymbol{F_{RF}}$) confines the ions radially in the TIMS tunnel and minimizes diffusion of the ion cloud.

As the flow of gas and the negative pressure differential drive the ions through the TIMS tunnel, an axial electric field gradient (EFG) is produced by the applying DC potentials to the ring electrodes (Figure 1-2). The DC potentials that define the EFG are set via a resistive divider. As the EFG slows the ion's drift velocity, the ion eventually reaches an equilibrium position when the drift velocity ($\vec{v}_d$) is equal and opposite to the gas velocity ($\vec{v}_{gas}$).

$$\vec{v}_d = -\vec{v}_{gas} \quad \textbf{(1-4)}$$

Simultaneously, an RF voltage is superimposed onto the ring electrodes to produce a radially confining quadrupolar pseudopotential (Figure 1-3). In theory, the RF field only confines the ions in the radial dimension and has essentially no axial component that could interfere with ion trapping in the tunnel. There has been considerable discourse in the literature about the effects of the RF field on the overall performance of the TIMS analyzer.[18,23,24,37–40] The undeniable fact is the radial confinement process is very complex, and several factors must be carefully considered to obtain optimal results. Firstly, sufficient ion confinement from the RF field is needed to maximize ion transmission and minimize losses of the total ion population.[41] Next, if the force exerted by the RF field is too strong (*i.e.,* large RF amplitude and/or high RF frequency), the ion cloud will begin to exhibit space charging effects. This leads to ion diffusion in the axial dimension caused by long range ion-ion repulsion that limit the extent that the ions can be confined in the center of the TIMS tunnel.[37] Finally, the total number of ions injected into the analyzer must be carefully controlled. Overfilling the TIMS tunnel with too many ions will also contribute to long range ion-ion repulsion and limit resolution. This can be regulated by decreasing the injection pulse time or reducing the electrospray voltage.[37]

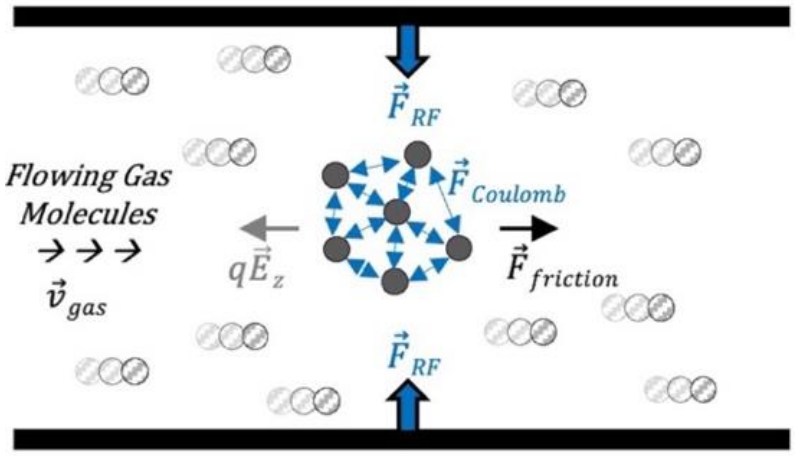

Figure 1-3. RF Confinement in the TIMS mobility region. The force exerted by the RF induced pseudopotential ($\boldsymbol{F_{RF}}$) confines ions along the central axis of the TIMS tunnel. When too many ions are injected into the analyzer, Coulombic repulsion ($\boldsymbol{F_{Coulomb}}$) forces cause the ions to diffuse axially.

1.3.2 Stages of a Typical TIMS Experiment

A TIMS experiment consists of three distinct instrumental phases (Figure 1-4): 1) Accumulation; 2) Trapping; and 3) Elution.[27] In the accumulation phase, a repulsive potential is applied to the deflector plate to push ions into the entrance funnel. The duration of time that the deflector pushes ions into the entrance funnel can be varied to increase or decrease the number of ions that are analyzed. The ions are then focused through the entrance funnel and enter the TIMS tunnel.

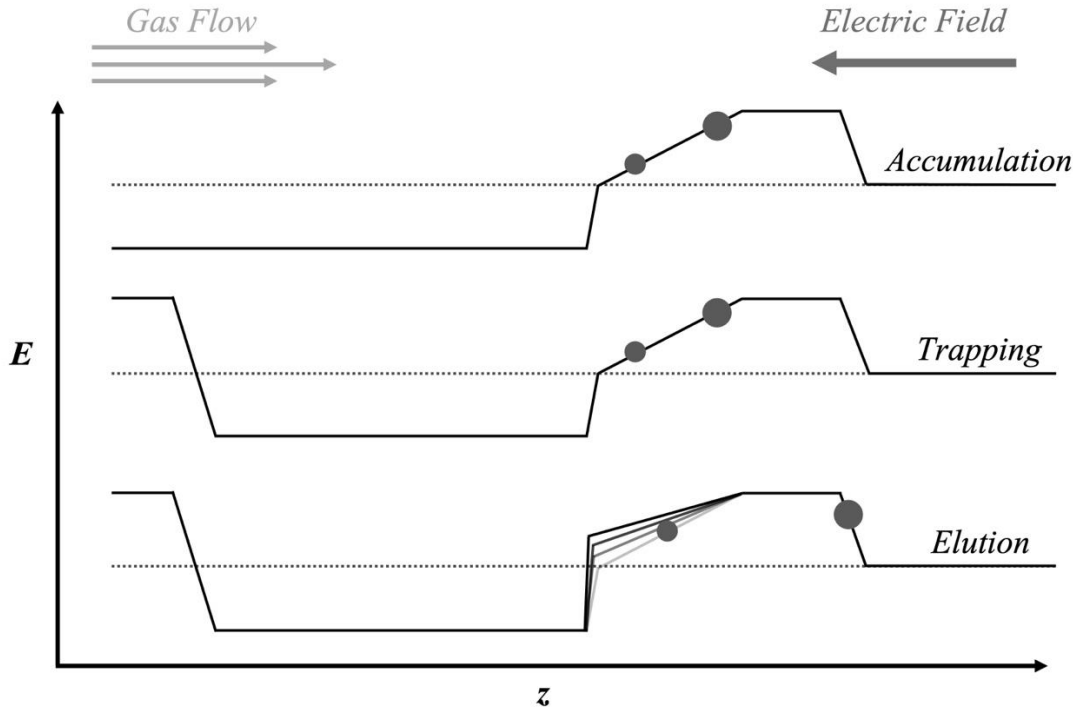

Figure 1-4. Stages of a typical TIMS experiment. ***E*** represents the electric field, and ***z*** corresponds to the axial position across the TIMS instrument.

As ions are pushed through the TIMS tunnel by the gas, they eventually reach an equilibrium position along the EFG where the magnitude of the field strength is large enough that the ions become trapped. Large ions (low *K*/large CCS) are trapped higher along the EFG ramp, since it takes a larger magnitude of the electric field to fully oppose the driving force of the gas on a low mobility ion. Smaller ions (high *K*/small CCS) will be trapped lower along the EFG ramp where the magnitude of the electric field is much smaller.[27] The profile of the EFG across the TIMS tunnel has two distinct segments, a linearly increasing voltage ramp

followed by a plateau. The DC potential across the plateau to the end of the TIMS tunnel is kept constant, while the DC potential at the entrance is variable. The resistive divider across the electrodes ultimately determines the step size of the gradient between successive electrodes, while the DC potentials applied to the front and end of the TIMS tunnel define the slope. Since the overall "shape" of the EFG doesn't change, the DC potential across the tunnel is considered directly proportional to the electric field strength on the plateau segment.[27,42]

In the trap phase, the potential on the deflector is switched to an attractive potential. This causes the ions exiting the transfer capillary to strike the deflector plate and neutralize. Since the electrospray ionization source is continuous, it is much more effective to use the deflector as an ion gate to modulate the total number of ions entering the analyzer as opposed to switching on and off the electrospray voltage. The ions that have already transited through the entrance funnel equilibrate along the EFG and are trapped inside the TIMS tunnel for several milliseconds. Depending on the characteristics of the analyte and the type of experiment (*e.g.*, kinetic studies, protein folding/unfolding, ion activation/dissociation, etc.), the trap time can be extended.

In the last phase, ions of increasing mobility are eluted from the TIMS analyzer through the exit ion funnel towards the detector as the magnitude of the EFG is decreased. Larger or more elongated ions with large CCS's will elute first, and smaller or more compact ions with smaller CCS's will elute later. Experimentally, the electric field strength is decreased by scanning the DC potential applied at the start of the TIMS tunnel from an initial DC potential (*e.g.*, –170V) to a smaller magnitude final potential (*e.g.*, +20V) at a user defined scan rate.[43] Different voltage ramps, step sizes, and scan rates can be implemented depending on the experimental needs. For example, to trap a wide range of ions with sizeable differences in mobility (*e.g.*, untargeted -omics applications), a large potential difference between the front and end of the TIMS analyzer is needed. On the other hand, if differentiation of two analytes with very similar mobilities is desired, a shallower potential difference is used to define the "shape" of the EFG profile, and the voltage is scanned with a much slower scan rate to separate the analytes. Using the latter approach, the

resolving power ($K/\Delta K$) of the TIMS can reach as high as 400.[34] The scanning event which elutes the trapped ions is one of the main differences between TIMS and other IMS instruments such as drift tube or travelling wave.[10,23] In a drift tube or travelling wave IMS, all ions pulsed into the drift region will be observed under the same experimental conditions. In a TIMS instrument, the main variable parameter, the EFG, must be changed to detect all the ions pulsed into the analyzer. Fortunately, the flexibility this approach affords is what makes TIMS so selective and enables high-resolution separations.

1.3.3 Analytical and Numerical Modelling of the TIMS

Significant effort has been spent developing analytical and numerical models that link the dependence of analyzer performance (*i.e.*, resolving power, time of elution, etc.) on experimental parameters, analyzer properties, and characteristics of the ions being studied.[18,24,33,37,41,42] To summarize, a quantitative theory was derived from ion mobility first principles that proves that the "analytically useful work" done on an ion as it is trapped and eluted over the electric field gradient plateau ultimately determines the resolving power. To maximize the analytical work done on the ion experimentally, the pressure (or pressure differential) can be increased across the tunnel. This will increase the gas velocity, and conversely decrease the ion's mobility. Additionally, slow scan rates or a narrow potential difference range across the electric field gradient will also boost the resolving power. Finally, controlling the magnitude of the RF field that radially confines the ions, and not overfilling the TIMS analyzer are other parameters that need to be carefully controlled to achieve optimal performance.

Numerical models developed with computational software such as COMSOL Multiphysics have also provided insight into the underlying gas dynamics in the TIMS. Most of these models have focused on understanding how the bath gas flow profile and pressure differential affect performance and operation of the instrument. These numerical models have demonstrated that the gas velocity flow profile through the central region of the analyzer is near homogenous, and only decreases towards the walls of the TIMS tunnel. This decrease, and the resulting parabolic flow profile, has been attributed to friction of the gas molecules with the inner wall.[24,41] To further understand the ion dynamics inside the TIMS cell, additional ion

trajectory modelling has been done using SIMION. As expected, these simulations confirmed that RF confinement is essential for stabilizing the ion cloud in the center of the flow axis.[41] In the axial dimension of the TIMS tunnel, the ions are relatively well confined along the flow axis by the electric field and drag forces from the bath gas. The RF field is critical for minimizing diffusion of the ions towards the walls, and if an insufficient RF pseudopotential is applied, over time the ion population will decrease as ions diffuse and neutralize during collisions with the walls. Interestingly, the model also demonstrated that too large of an RF pseudopotential will lead to axial diffusion as the ions compensate for the Coulombic repulsion imparted by the ion cloud.[37,41] Therefore, the overall size of the ion cloud is determined by both the radial and axial fields, as well as the number of charges (*i.e.*, ions) that are confined within the TIMS cell.[18,41]

1.4 TIMS Calibration Strategies

IMS instruments are primarily used in the laboratory to rapidly separate ions in the gas phase, however they also provide the means to measure an ion's mobility and calculate its CCS. DTIMS instruments can measure the reduced mobility (K_0) and by extension, calculate the CCS directly from first principles using the Mason-Schamp equation assuming the drift tube is operated under the low field limit.[10–13,23] Unfortunately, the TIMS cannot directly measure an ion's K_0 since the ions are separated with a dynamic electric field that operates above the low field limit. Additionally, the temperature of the system must be known to calculate the K_0, and while the temperature is assumed to be approximately room temperature in the TIMS cell this has not been accurately verified.[43] Therefore, the TIMS instrument must be externally calibrated using standards with known K_0 values that have been published in the literature.

Three different external calibration strategies have been proposed for accurately calibrating TIMS instruments. In the first method a calibration curve is constructed by plotting the experimental elution voltage relative the voltage applied at the end of TIMS ($V_{elute} - V_{out}$) against the inverse reduced mobility ($1/K_0$) for a series of calibrants.[41] The y-intercept in the external calibration plot corresponds to the voltage applied to the end of the TIMS tunnel and the slope is referred to as the calibration constant (A-term).[41] The second method is more straightforward, and directly links the literature K_0 with the inverse of the elution

voltage. A calibration curve is produced for a series of calibrants and using standard linear regression, the line of best fit equation determines the K_0 for other analytes of interest.[27] In both approaches, the velocity of an ion through the bath gas is directly proportional to the product of the strength of the electric field and the mobility.[9] Consequently, the field strength required to trap the ion must be inversely proportional to the mobility. Since the field strength is also proportional to the potential applied across the tunnel, the mobility will be inversely proportional to the elution voltage.[18] The third method applied a more complex methodology by modelling the TIMS calibration using a Taylor expansion series derived from the Boltzmann transport equation.[44] Out of the three calibration methods, the third method is the only one that is sample independent, however it still requires reference K_0 values. The main limitation to these methods and a large source of error for any K_0 measurements taken on the TIMS is the reliance on literature K_0 values. The challenge to reducing this error is finding suitable K_0 values that most closely match the conditions found in the TIMS; especially since the temperature inside the TIMS is merely an "educated" assumption and can't be precisely measured. This limitation is even more apparent when calibrating the TIMS to measure the K_0 of high mobility ions. Most literature K_0 measurements for these types of ions are measured on DTIMS instruments that operate at higher temperatures and pressures, meaning the instrumental conditions are much different than those used for the TIMS.[45,46]

Most recently, a significantly different approach for calibrating a TIMS has been published. In this work, a custom-built drift tube IMS is interfaced directly with the entrance funnel of the TIMS to experimentally measure the mobilities of the calibrants.[43,47] The DTIMS is operated at ambient temperature to more closely match the instrumental conditions found inside the TIMS cell. To calibrate the TIMS, a similar approach to the first calibration method discussed above is used. A calibration curve is prepared for the selected calibrant ions that plots the TIMS elution voltages relative to $(1/K_0)$ values measured by the drift tube. This approach is advantageous since the measurements are taken directly on the system being calibrated which minimizes instrument specific biases and eliminates the need for literature K_0 values.

1.5 Overview of Different TIMS Instruments

Arguably the biggest advantage of the TIMS, besides the high resolving power, is its versatility and modularity. The small instrumental footprint combined with the ability to interface the TIMS with different MS instruments, along with the hardware capabilities required to perform a wide variety of ion activation/dissociation experiments make the instrument extremely robust. Historically, the TIMS has functioned as a single analyzer coupled to a quadrupole – time of flight (QTOF) MS instrument (Figure 1-5, A).[25,26,48] The fast scan speed (~200 µs) of the QTOF compared to a triple-quadrupole MS or Orbitrap MS is the main reason why the TIMS analyzer is hybridized with the QTOF.[49,50] The average peak width as an ion elutes from the TIMS is on the order of 1 to 2 ms. Therefore, to obtain enough MS scans across the peak, an MS instrument with a fast scan rate such as the QTOF is required.

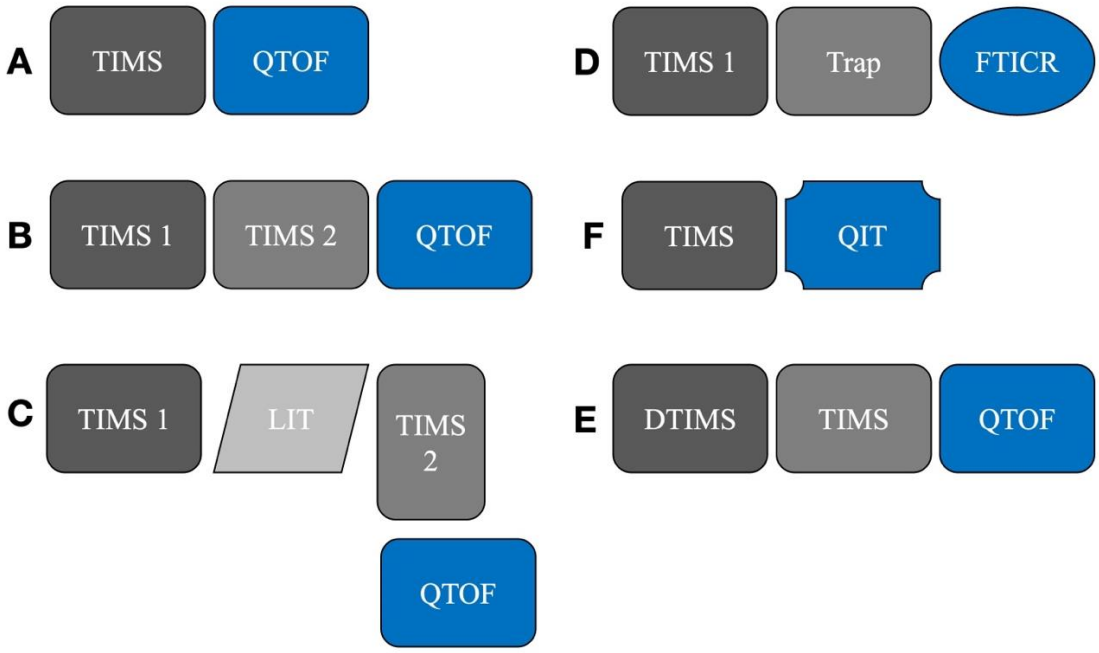

Figure 1-5. Various TIMS hardware configurations. TIMS – Trapped Ion Mobility Spectrometry; QTOF – Quadrupole Time of Flight Mass Spectrometry; LIT – Linear Ion Trap; FTICR – Fourier Transform Ion Cyclotron Resonance Mass Spectrometry; DTIMS – Drift tube Ion Mobility Spectrometry; QIT – Quadrupole Ion Trap.

Building on the success of the first generations of TIMS and other tandem IMS systems,[51,52] a prototype research instrument consisting of two analyzers coupled in parallel and hybridized with a QTOF was

reported in literature (Figure 1-5, B).[53,54] In this configuration, both TIMS cells are differentially pumped in different vacuum chambers and individually controlled. Sequentially coupling two TIMS opens the door for various modes of operation. The most widely used mode is parallel accumulation.[55] In a parallel accumulation experiment, ions are trapped and stored in the first TIMS cell prior to being mobility separated in the second cell. The parallel accumulation mode can also be used in the upgraded commercial version of the instrument that has a single TIMS analyzer with an extended separation tunnel region. Instead of splitting the two analyzers into different chambers like the protype tandem instrument, the TIMS tunnel in the upgraded commercial instrument is extended to be twice as long but still housed in the same vacuum chamber.[54] Using the same parallel accumulation operating principle, ions are accumulated in the first half of the TIMS tunnel before being separated in the second half. In both cases, the parallel accumulation mode vastly increases the duty cycle of the TIMS, since ions are continuously collected in the first TIMS while mobility analysis simultaneously occurs in the second TIMS.[55] Furthermore, configuring the first TIMS cell (or first half of the TIMS tunnel) to accumulate low intensity ions prior to injection into the second analyzer (or second half of the TIMS tunnel) significantly increases the sensitivity.

A unique advantage to the prototype tandem TIMS instrument is if sensitivity isn't required and the experiment necessitates high resolution, tandem mobility separation mode can be used. In this mode, ions are mobility separated under one set of instrumental conditions in the first TIMS cell, before being eluted into the second TIMS cell where they are further separated under a different set of conditions.[54] Another useful feature of the tandem TIMS instrument is the arrangement of several annular electrodes installed at the interface between the two analyzers. Ions can be collisionally activated at this interface, leading to fragmentation through the traditional collision induced dissociation (CID) process.[52,56] As ions elute from the first TIMS, a large DC potential is applied across the interface electrodes, resulting in a strong electric field of up to 800 V/cm that induces fragmentation of the mobility selected ions.[53] The second TIMS then mobility analyzes the CID fragment ions prior to MS detection.

A slightly different iteration of the tandem TIMS configuration has also been reported. Instead of connecting the two analyzers coaxially, the two cells are interfaced orthogonally with a custom linear ion trap (LIT) in between.[37,54,57] The same modes of operation described above for the coaxial tandem TIMS are also employed on the orthogonal tandem TIMS configuration. The LIT is constructed from printed circuit boards and has a fused silica window at the far end where an ultraviolet (UV) laser and optical setup are installed (Figure 1-5, C). After trapping ions eluting from the first TIMS in the LIT, ion activation can be induced through traditional CID by changing the DC potentials on electrodes at the end of the trap.[58] Alternatively, ions can be irradiated with the UV laser, causing ion activation via UV-photodissociation (UVPD).[57,59–61] The resultant CID or UVPD fragments are then mobility separated in the second TIMS before transiting towards the QTOF for MS detection.

There has also been considerable research focused on coupling the TIMS analyzer to a Fourier transform ion cyclotron resonance (FTICR) MS instrument (Figure 1-5, D).[48,62–65] This configuration is very effective when ultra-high resolution MS measurements are desired. To hybridize the TIMS with an FTICR MS, the collision cell of the FTICR was converted into an ion trap to synchronize the TIMS with the slow scan speeds (~1 s) of the FTICR-MS. The trap is configured to accumulate ions eluting with the same mobility from the analyzer over the course of several TIMS cycles before injecting the batch of ions into the FTICR. Then, as the FTICR is mass analyzing that specific batch of ions, the trap is accumulating the next group of ions that were mobility analyzed in the TIMS.

The biggest disadvantage to the QTOF MS, and especially the FTICR MS, are the high costs associated with purchasing and maintaining the instruments, as well as the large instrumental footprint. To address these limitations, a technical report was recently published that described the hybridization of a TIMS analyzer with a Paul quadrupole ion trap (QIT) (Figure 1-5, F).[66] While the benchtop QIT doesn't offer the same *m*/*z* resolving power as the QTOF or FTICR, the price and ease of operation make it an effective alternative. Like the orthogonal tandem TIMS instrument described above, the purpose of this instrument is to first mobility separate ions using the TIMS cell, then irradiate the ions trapped in the QIT using a UV

laser to form UVPD fragments. The main difference between the instruments is that in this configuration, UVPD is induced directly in the mass analyzer, whereas in the orthogonal tandem TIMS, UVPD is induced in an ion trap that has no mass filtering capabilities.

As discussed in Section 1.4, a more unconventional TIMS instrument has been reported in the literature that couples a DTIMS operating at atmospheric pressure to the front end of the TIMS-QTOF instrument (Figure 1-5, E).[43] Unlike other TIMS configurations described herein, the DTIMS is not operated as a mobility analyzer operating in tandem with the TIMS. Instead, the DTIMS serves as an onboard calibration system to measure the mobilities of calibrant ions that are then used to generate the reduced mobility calibration curves for the TIMS. By directly measuring the mobilities of the ions on the same platform, many of the inaccuracies stemming from comparisons with literature mobility values are eliminated, and there are no limitations on the series of calibrants that can be used.

1.6 Ion Activation/Dissociation Strategies Coupled to TIMS

Alternative ion activation/dissociation (*e.g.,* UVPD) strategies coupled to TIMS provide more comprehensive datasets for structural characterization and/or identification of proteins/peptides when compared to collisional activation on its own. The advantage to these approaches is that mobility selected ions eluting from the TIMS analyser can be probed individually, followed by high-resolution mass analysis of the resultant fragments. The most ubiquitous ion activation technique, CID, is employed on every tandem mass spectrometer in the collision cell.[49,67,68] Ions are energetically activated through multiple low energy collisions with a gas, and the CID fragments are mass filtered in the third quadrupole before being detected.[49,67,68]

A similar approach is implemented in the TIMS. A strong electric field generated between adjacent lenses at the exit orifice of the TIMS tunnel combined with the relatively high pressure inside the analyzer (1-3 mbar) readily generates CID fragments.[48,54] Similarly, collision induced unfolding (CIU) is also possible with this configuration.[56,69] Unlike CID where the ion is fragmented, CIU measures how the CCS of a

protein or peptide changes when the ion is vibrationally activated by collisions with the gas. These collisions ultimately lead to cleavage of non-covalent bonds that hold the protein in its three-dimensional conformation. CIU is usefully for studying the tertiary structures of proteins, however, for large protein systems, the CIU process often results in the loss of the higher order structure of the subunits.[70] In both cases, the main advantage is that the ion activation event occurs prior to the ions reaching the mass analyzer, so the full tandem mass filtering capabilities of the MS instrument can be utilized for further characterization and analysis.

The drawback to CID/CIU for top-down proteomic studies or structural characterization experiments is that CID is a low energy, multi-step process.[70,71] In most cases, only the peptide bond (N-C) in the protein/peptide is accessible for cleavage by CID and there is no cleavage of disulfide/thioether bonds.[71,72] This leads to limited sequence coverage and increases the potential for misidentification of the protein. Alternative ion-activation techniques coupled to the TIMS such as UVPD mitigate these drawbacks by targeting specific linkages in the protein sequence that readily absorb UV light, inducing unique fragmentation patterns that cannot be generated through the CID process.[59,71] UVPD has been implemented in a variety of different TIMS platforms for various applications and described in several comprehensive reviews.[54,57,73] In summary, the overarching theme is that utilizing the TIMS first to mobility select species of interest prior to UVPD, followed by a second mobility separation prior to MS analysis significantly improves the quality of the data and increases the number of unique fragments that can aid in protein identification. An alternative to CIU is surface induced dissociation (SID). The SID process hybridized to the TIMS operates in a much different manner to other ion activation techniques. Mobility selected ions eluting from the TIMS are accelerated into a highly charged surface at the interface between the end of the TIMS tunnel and the entrance ion optics of the MS.[70,74] The result of this collision is a rapid increase in the internal energy of the macromolecular complex, leading to cleavage of non-covalent bonds while still retaining the native structure of the protein subunits. This high energy process occurs incredibly quickly, and unlike CIU, generates low charge state products that retain their native conformation.

1.7 Summary of Applications utilizing TIMS

TIMS has demonstrably proven to be a valuable tool for a range of analytical applications due to its high sensitivity, modular design, high resolving power, and separation speed. Due to these advantages, TIMS has had a major impact on the broader scientific community. It has been extensively used as a pre-separation step in targeted and untargeted metabolomic, lipidomic, and proteomic workflows. It has also been instrumental in the characterization of higher order structure of peptides, intact proteins, and macromolecules.

For targeted and untargeted small molecule -omics experiments (*e.g.*, lipidomics and metabolomics), the TIMS-QTOF instrument is often hybridized with standard liquid chromatography (LC) systems. This configuration provides two orthogonal separation stages in the analytical workflow. Compounds are first separated based on their interaction with the stationary phase in the column, followed by gas phase mobility separation in the TIMS. For example, this approach was used to separate co-eluting lipid isomers that have the same interaction with the stationary phase in the LC dimension but slightly different mobilities in the IMS dimension. Due to the high resolving power of the TIMS, the isomers were able to be baseline separated.[73,75,76] Alternatively, in traditional metabolomics studies focused on identifying trace levels of biologically relevant metabolites, the parallel accumulation mode can be used to first accumulate low abundance analytes in the gas phase without the reliance on extensive and time-consuming sample preparation, followed by mobility separation and MS analysis.[77–80] Furthermore, the ability to calculate the CCS of an unknown metabolite using the TIMS provides an additional level of confidence to the fragmentation pattern and high-resolution for accurate analyte identification.

The parallel accumulation mode of the TIMS-QTOF instrument has also been beneficial for increasing the sequencing speed and sensitivity for shotgun proteomics studies.[55,81] In these applications, the TIMS is synchronized with the QTOF to sequentially release precursor ions of the same mobility to be fragmented in the collision cell prior to high-resolution TOF-MS analysis. All the peptide ions sharing the same mobility are compressed into a narrow peak, vastly increasing the number of peptide fragment spectra that

are obtained by the MS. Simultaneously, the overall sensitivity is increased since interfering background ions or other matrix interferences are separated from target compounds by ion mobility. This technology has seen immense success in rapid proteome profiling, which is a key attribute in clinical proteomics, and the sensitivity makes it well suited for chemical analysis of single cells.[82] As discussed in Section 1.5 and Section 1.6, TIMS can incorporate alternative ion activation methods such as UVPD to generate unique peptide fragments for protein identification and sequencing in top-down proteomics. While the UVPD-TIMS shows immense potential, it is not as widespread and have been mostly limited to research labs aiming to demonstrate the feasibility and potential of the technique.[83]

Studying the higher order structure of proteins and protein complexes is a difficult task that requires specialized MS instrumentation and a large degree of biochemical intuition. Under most conventional instrumental conditions, intact proteins "unravel" and denature, completely losing their tertiary structure.[84,85] Only under very specific buffer and instrumental conditions do the ions retain their native conformation, which is vital for characterizing the three-dimensional structure of the molecule.[86] Besides this, most instruments, with TOF MS being the exception, do not have the upper mass range required to detect the low charge states of the molecule that are characteristic of the intact full form of the molecule. Several IMS techniques have been successfully used to characterize the structure of proteins and other biomolecules.[85] More specifically, TIMS has been very effective for this challenging application since the duration of trapping in the TIMS analyzer can be varied and precisely controlled. The rate at which a protein unfolds and its stability in the gas phase can be studied by comparing the mobilities and charge state distributions of the native versus denatured ion populations.[73,87–90] Improvements have also been made to the electrode geometry of the TIMS to aid in retaining the higher order protein structure for large intact proteins and macromolecular complexes. The conventional concave electrodes were modified to a convex shape, which increases the penetration of RF field for adequate radial confinement of large proteins and protein complexes at lower RF amplitudes.[73,91,92] Furthermore, incorporating ion activation techniques such

as SID with TIMS provides biologically useful information about the higher order structures of a protein or peptide by retaining the native conformation of the subunits after dissociation of the larger complex.[54,70,71]

1.8 Research Objectives

Since its release almost 15 years ago, the TIMS technology has become increasingly popular due to its versatility and high resolving power. Most of the significant technical advances have been accomplished by modifying the auxiliary hardware surrounding the TIMS analyzer, hybridizing multiple analyzers/traps into one combined instrument, as well as improvements to the electronics and software for additional modes of operation. However, there has been minimal research focused on characterizing alternative designs to the tunnel section (*i.e.*, mobility region) where the ions are separated; or how changes to the way the gas flow profile is established through the tunnel can improve performance. Minimal emphasis has also been placed on the electrical design that defines the trapping EFG. Redesigning the electronics for complete user-definition of the shape and operability of the trapping EFG through individualized control of each electrode that comprises the mobility region is a requisite next step. Summarily, there are two research questions that underpin the entirety of the research contained in this thesis: 1) Does introducing higher multipolar radial RF confinement enhance trapping capacity and improve resolution; 2) Does introducing a gas flow velocity gradient through the mobility region improve resolution of a TIMS analyzer. Thus, the singular underlying motivation for this thesis can be distilled into the following hypothesis:

Can a multi-sector IMS instrument, referred to as the variable flow trapped ion mobility spectrometer (vfTIMS) be designed, and built, as a new tool for high resolution ion mobility separations?

The goal of the prototype vfTIMS is to combine enhanced ion focusing and ion accumulation with the unique capability to separate ions in multiple sections of the instrument with an entirely customizable EFG. The segmented mobility region of the vfTIMS with four sectors of decreasing inner diameter creates a gas flow profile where the velocity of the gas increases uniformly through each sector, resulting in ions experiencing a driving force that increases proportionally as they transit through the system. By fine tuning

the electric field strength through the various sectors of the mobility region it is expected that high-resolution separations will be achievable on the vfTIMS. The three research objectives needed to achieve this goal are as follows:

1. Construct a prototype ion mobility spectrometer, combining multiple commercial and in-house components.
2. Implement an improved electrical layout to drive the instrument, with the added ability to define all the electric fields within the analyzer.
3. Fully characterize the performance of the prototype instrument for ion trapping and ion mobility separation.

This thesis aims to address these objectives through the chapters that make up its content. Chapter 2 and Chapter 3 cover the design and construction of the vfTIMS. More specifically, Chapter 2 outlines the various hardware components of the vfTIMS that were either designed and built in-house or purchased commercially and modified. Chapter 3 details the design and testing of the electronics that power the system, along with the development of the user interface to control the instrument. Chapter 4 presents the extensive experimental optimization that was completed to get the instrument operational. Additionally, Chapter 4 also covers the experimental results that establish a baseline set of instrumental conditions that should be used for more complex experiments. Chapter 5 describes the first two proof of concept studies to demonstrate the feasibility of ion mobility separation experiments on the vfTIMS, building on the knowledge gleaned from the experiments in Chapter 4. Lastly, Chapter 6 serves as a roadmap for what must be done next to advance the project, in both the short term as well as the longer term.

Chapter 2: Hardware Design/Development

2.1 Preamble

This chapter has not yet been published. Once a vfTIMS ion trajectory model that is currently in development as well as additional experiments that demonstrate the instrument's mobility separation capabilities are finalized, a manuscript that incorporates most of the information described in Chapter 2 through Chapter 5 will be prepared for submission to the Review of Scientific Instruments journal in 2024. Daniel Rickert, and Hiruy Haile from the University of Waterloo Science Technical Services Machine Shop, built the vacuum chamber and all associated hardware components. Daniel Rickert redesigned and improved an existing electrospray ionization source/three-dimensional positioner that was originally built by Daniel Rickert and Hiruy Haile during his MSc in the Pawliszyn Lab. The entire entrance funnel assembly was designed and built by Gordon Anderson at GAA Custom Electronics. The mounting hardware inside the vacuum chamber that holds the entrance funnel and connects it to the mobility region was designed and built by Daniel Rickert and Hiruy Haile. Daniel Rickert, along with Hiruy Haile, and Krunomir Dvorski in the University of Waterloo Science Technical Services Electronics shop, built the mobility region and designed the wiring layout. The Faraday detector and transimpedance amplifier were designed and built specifically for this project by Gordon Anderson. The axial and radial gas flow profile modelling using COMSOL Multiphysics was done by Daniel Rickert and Emir Nazdrajić. Janusz Pawliszyn and Scott Hopkins were responsible for conceptualization of the project, project supervision, and funding acquisition.

2.2 Introduction

Over the past two decades, commercial ion mobility spectrometers have soared in popularity, prompting major mass spectrometry companies to develop their own specialized instruments.[85] One of the newest iterations, the trapped ion mobility spectrometer, has been recently commercialized by Bruker Daltonics. As is the case with all high-performance commercial instruments, the Bruker TIMS comes at a high cost

and lacks certain features that were implemented for the prototype IMS instrument described in this thesis. Therefore, this project largely focuses on the design, construction, development, and characterization of a custom-built variable flow trapped ion mobility spectrometer (vfTIMS).

The main difference between the vfTIMS and the commercial TIMS lies in the mobility region where ions are separated based on differences in their mobility. The mobility region in the commercial TIMS instrument is comprised of a single tunnel of uniform inner diameter (I.D.). In contrast, the mobility region of the vfTIMS is comprised of four discrete sections with progressively decreasing I.D. As the I.D. decreases from one sector to the next, the gas velocity will have a corresponding, yet uniform, increase. This configuration ultimately produces the gas flow velocity gradient through the instrument while also adding the capability for four separate regions where the ions can be trapped, and ultimately separated. Furthermore, due to the design of the electrodes within the mobility region, there is complete flexibility in the application of the DC electric field used to trap the ions. This chapter encompasses both the instrument's design as well as descriptions of the various commercial and home-built components that were integrated to build the instrument. Additionally, an *in-silico* evaluation of the gas dynamics within the system was performed to better characterize the system.

2.3 Instrument Overview

The prototype instrument depicted in Figure 2-1 works as follows: Ions are generated by a continuous flow nanoESI source and pass through a heated transfer capillary before accumulating in the first ion funnel (*i.e.*, entrance funnel). The last lens of the entrance funnel, referred to as the conductance limit, functions as an electrostatic gate that periodically injects ion packets into the mobility region. Once in the mobility region, the ions traverse through the four sectors, where they can be trapped and eluted by varying the DC electric field gradient generated by the embedded stainless-steel electrodes. After passing through the mobility region, the ions proceed through the copper tube lens attached to the last ring of electrodes in the fourth (*e.g.*, smallest I.D.) sector of the mobility region. The tube lens ensures ions pass through the PEEK pressure divider that splits the vacuum chamber into two smaller sub-chambers. A Faraday plate detector with an

integrated DC grid enclosed by a ground plane is affixed to the backside of the pressure divider. A transimpedance amplifier (nA → V) amplifies the current produced by ions discharging onto the Faraday plate. The voltage is measured and recorded by connecting the amplifier to an oscilloscope and/or the built-in analog to digital converter (ADC) installed in the modular intelligent power supply unit.

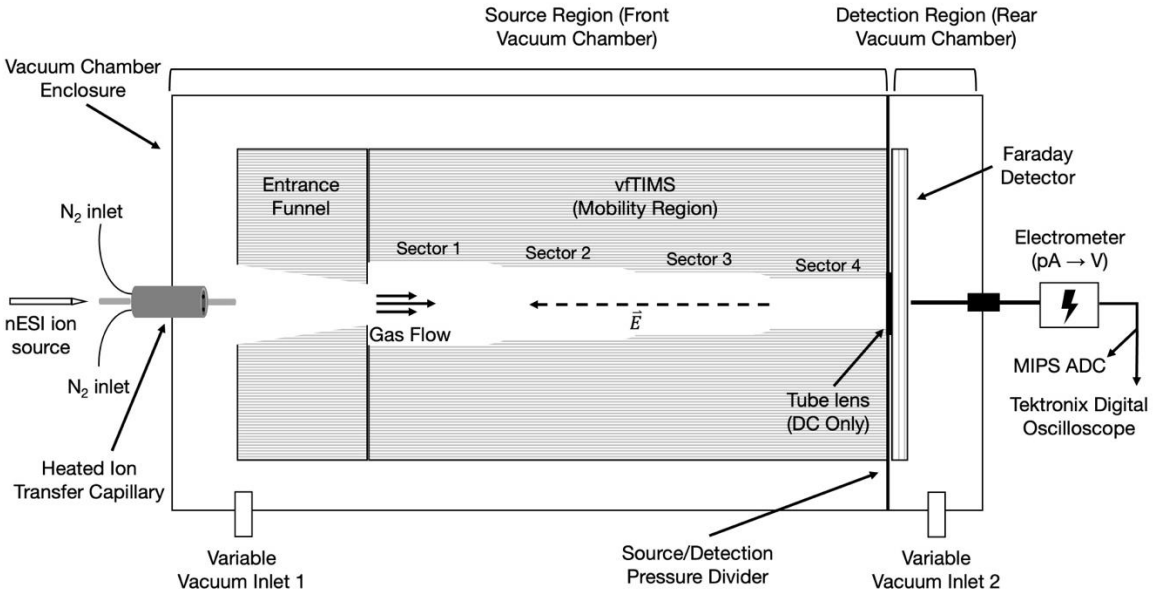

Figure 2-1. Schematic diagram of variable flow ion mobility spectrometer (Diagram not shown to scale).

2.3.1 Vacuum Chamber

As depicted in Figure 2-1 and Figure 2-2, the entrance funnel, mobility region, and detector are contained in a repurposed vacuum chamber that was modified with the assistance of the University of Waterloo Science Technical Services Machine Shop. The cylindrical body of the vacuum chamber is constructed from 3.175 mm thick stainless steel, with internal dimensions of length = 470 mm, and diameter = 267 mm. Aluminum caps on either end of the chamber can be removed and are sealed with an O-ring. Most of the electrical wiring feeds through another removable aluminum plate in the center of the vacuum chamber that is also sealed with an O-ring.

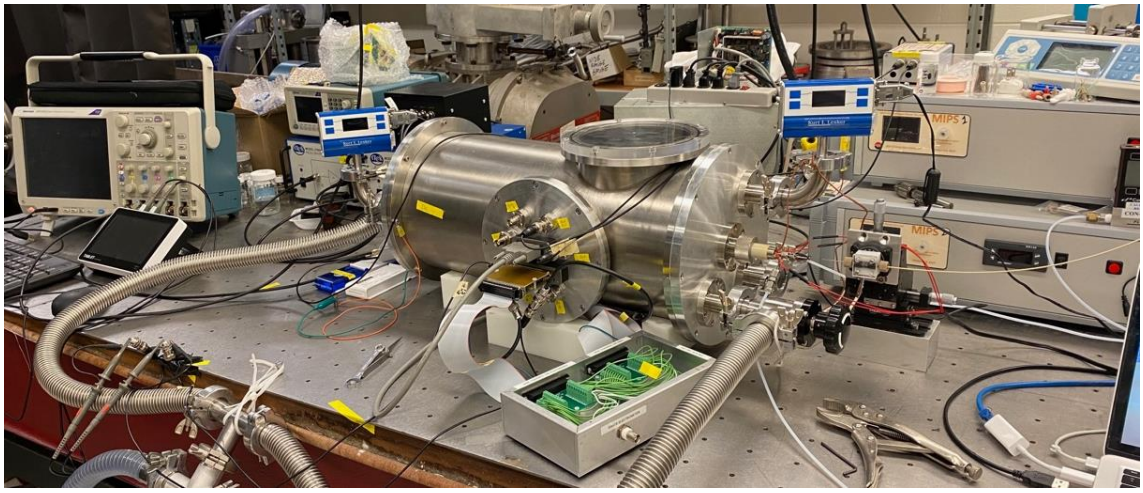

Figure 2-2. Exterior view of vfTIMS in the Hopkins Laboratory.

The chamber is pumped by two E2M30 30 m³/hr dual-vane rotary pumps (Edwards; Massachusetts, USA), connected via an aluminum tee, before splitting off and connecting to the flange on each end plate of the vacuum chamber. Installed inside the vacuum chamber is a custom-built PEEK pressure divider apparatus that seals against the inner surface of the walls of the vacuum chamber and isolates the front section from the back. The pressure divider essentially splits the vacuum chamber into two smaller chambers: the source region chamber and the detection region chamber. Mounted through the center of the pressure divider is a DC-only copper tube lens with an inner diameter of 7.9 mm. The tube lens is attached to the last set of electrodes at the end of the mobility region and transmits ions exiting the mobility region towards the detector, which is mounted to the backside of the divider. The magnitude of the negative pressure differential (*e.g.*, slightly higher pressure in the source region (*i.e.*, front chamber) versus the detection region (*i.e.*, rear chamber)) is controlled by a combination of varying the degree of pumping on either side of the vacuum chamber using angle valves (Kurt J Lesker; Pennsylvania, USA) connected to the end caps and adjusting the flow rate of the N_2 carrier gas. The pressure inside the vacuum chamber (900 millitorr (mTorr) to 3 Torr) is continuously monitored by a convection enhanced Pirani vacuum gauge (Kurt J Lesker; Pennsylvania, USA) that is installed on each end plate.

2.3.2 Ion Source & Sample Introduction

The ion source for the vfTIMS is a nanoESI unit.[93] The entire nanoESI assembly is shown in Figure 2-3. The analytes are dissolved in MS grade Methanol (MeOH) and delivered to the glass nanoESI capillary by a Fusion 100 syringe pump (Chemyx; Texas, USA), at a flow rate of 0.5 to 2 μL/min. QuartzTip nanoESI emitters (1.0 mm outer diameter (O.D.), 0.58 mm I.D.) with tip size of 2 ±1 μm are used for all experiments (New Objective; Massachusetts, USA). An in-house ionization source is used to accurately position the nanoESI emitter in front of the transfer capillary.[94,95] To generate the electrospray, a potential of +1200V to +2500V is applied by an alligator clip connected to either the conductive coating on the outer surface of the glass capillary or the metal union that joins the emitter to the PEEK tubing from the syringe (Figure 2-3, Left). Both approaches do not require the insertion of a platinum electrode inside the capillary which can introduce carryover between samples. As recommended in literature, nanoESI emitters with tip sizes of < 5 μm are specifically chosen to ensure that ions are sufficiently desolvated before transiting through the transfer capillary into the entrance funnel.[96]

The tip of the nanoESI emitter is aimed directly at the opening of a 15 cm long, 1.6 mm O.D., 0.762 mm I.D. stainless steel transfer capillary. The transfer capillary is inserted into a stainless-steel inlet block and secured with a Swagelok fitting. The capillary is heated to 160°C with two cartridge heaters installed on either side of the inlet block that further aid in ion desolvation. An outer heat-stable thermoplastic sleeve electrically isolates the capillary from the rest of the chamber (Figure 2-3, Right). The entire assembly is sealed into the vacuum chamber with a 19.05 mm I.D. stainless-steel Quick Connect Coupling (Kurt J Lesker; Pennsylvania, USA) and can be easily removed when the chamber is not under vacuum for cleaning or other required maintenance. The temperature of the transfer capillary is controlled with a proportional integral derivative controller that monitors the inlet block temperature with a type K thermocouple (Model CN142, Omega Engineering; Connecticut, USA) that is secured in a small hole drilled into the front of the block. A second alligator clip connected to the transfer capillary is used to apply a DC potential (*ca.*, + 50

to + 60 V) to improve transmission of ions into the entrance funnel and further reduce neutral solvent molecules from entering the system.

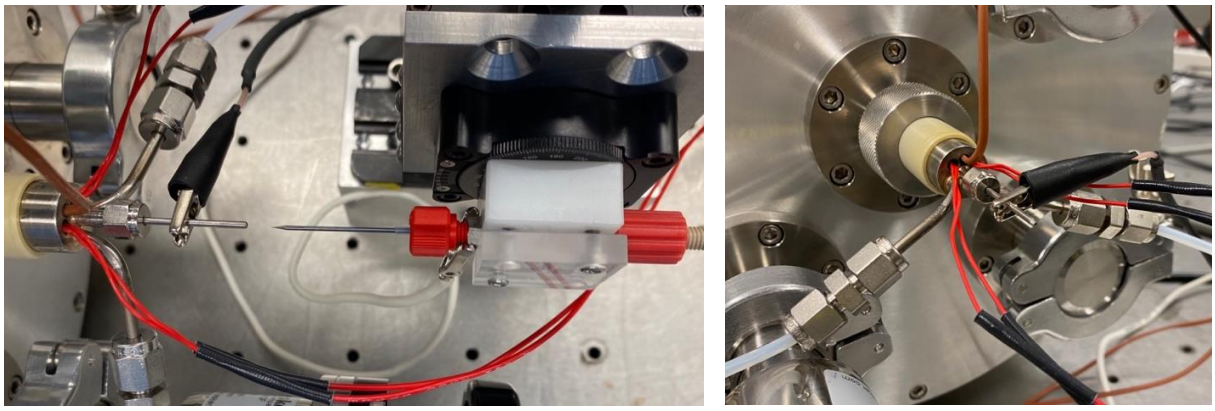

Figure 2-3. (Left) Continuous flow nanoESI source interfaced with heated transfer capillary. **(Right)** Heated transfer capillary assembly with thermocouple and barrel heaters installed.

Two co-axial gas lines are also installed in the inlet block and introduce N_2 carrier gas into the front section of the vacuum chamber. An ultra-high purity N_2 (Linde; Ontario, CA) gas cylinder with a needle valve installed after the regulator controls the flow of N_2 to the vacuum chamber. The gas flow is monitored with an in-line flowmeter (Cole-Parmer; Quebec, CA), with the flow rate typically between 0.1 to 0.5 standard liters per minute (SLPM).

2.3.3 Entrance Ion Funnel

The electrodynamic entrance funnel was designed and manufactured by GAA Custom Electronics (Washington State, USA) and is constructed using stacked FR-4 printed circuit boards (PCB). The entrance funnel focuses the ions as they exit the transfer capillary and transmit them towards the central mobility region.[22,97] This funnel is comprised of two main sections, a 74 mm long tunnel with a uniform I.D. of 25.4 mm, followed by a 27 mm long funnel section with a decreasing I.D. from 25.4 mm to 9.9 mm (Figure 2-4 – Left). A schematic of one of the PCB lenses is shown in Figure 2-4 – Right. The boards and spacers that make up the funnel are held together by four PEEK rods that run the length of the funnel and screw into place. In the vfTIMS, an additional modification was made to the standard ion funnel shown in Figure 2-4 – Center. Larger external spacer plates were added at the front and back to allow for aluminum

mounting rods to hold the funnel inside the vacuum chamber. These mounting rods screw onto the inner surface of the cover on the front of the chamber and connect to the PEEK pressure divider.

Each PCB lens is fabricated by depositing a thin layer of gold-coated copper onto the dielectric material. This forms a thin, 2 mm ring on the inner surface, ensuring ions are only exposed to conductive surfaces.[98] Mounted on the outer left and right sides of the ion funnel are the coupling boards containing the resistors and capacitors needed to supply the DC voltage and RF waveform to the lenses. These boards, along with two additional boards with no electrical components seal the four sides of the funnel so ions cannot escape through gaps in the individual PCBs. As shown in Figure 2-4, the DC and RF coupling boards are connected to the individual PCB lenses with conductive tabs that extend outwards from the gold-coated inner edge to the outer edge of the PCB. A DC potential is applied to each lens to produce a linear DC gradient that is set by a voltage divider running along the entire length of the entrance funnel on the DC coupling board. The RF potential is superimposed onto the PCB lenses via the RF coupling board and is configured such that opposite phases are applied to alternating lenses creating a dipolar RF induced pseudopotential. The DC potential gradient drives the ions towards the mobility region, while the dipolar RF field confines them to the center of the funnel away from the walls. The last lens of the entrance funnel (*e.g.*, the conductance limit) is not connected to the voltage divider, and the DC potential can be switched independently from the rest of the funnel. This allows it to act as an electrostatic gate, transmitting ions when set to a certain DC potential, but accumulating ions in the funnel when held at a significantly higher or lower DC potential. A detailed explanation of the power supplies that drive the entrance funnel can be found in Chapter 3.

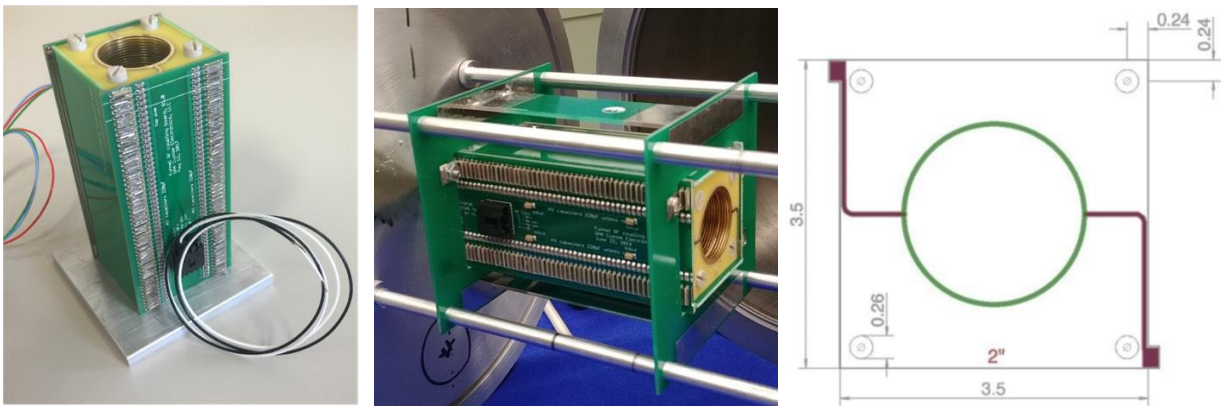

Figure 2-4. (Left) Printed circuit board electrodynamic ion funnel. **(Center)** Custom entrance funnel assembled on mounting rods inside vacuum chamber. **(Right)** Schematic of an ion funnel PCB lens (measurements in inches).

2.3.4 Mobility Region

The body of the mobility region (Figure 2-5) is constructed from a high-grade polyoxymethylene thermoplastic (Delrin, Dupont; Delaware, USA) and secures the steel pin electrodes that protrude into the inner cavity. The inner cavity has been precision machined with four sectors of decreasing I.D. along the direction of gas flow: 14 mm, 12 mm, 10 mm, and 8 mm (Figure 2-6 – Left). The total length of the mobility region is 120 mm. Each sector is 28 mm long, with a 2 mm, 27° inward taper as the I.D. decreases between adjacent sections.

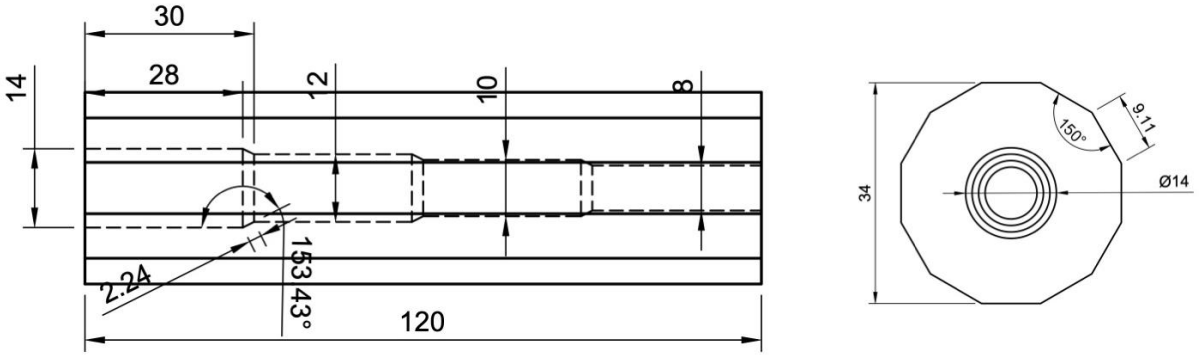

Figure 2-5. (Left) vfTIMS mobility region schematics (measurements in millimeters). **(Right)** Z-axis cross section of vfTIMS mobility region.

Introducing a taper rather than a 90° step-change reduces gas flow turbulence and is expected to improve performance of the vfTIMS instrument. Evenly spaced holes were drilled along the entire length of the

mobility region on all twelve sides to accommodate 1.5875 mm stainless steel pins. The pins serve as electrodes and are embedded into the body of the mobility cell, protruding 1 mm into the inner cavity. After inserting the pins, Agilent TorrSeal (California, USA) was applied in a recessed groove around the outer surface of the pin hole to immobilize the electrodes at the correct depth. This also ensures that all the carrier gas must pass through this section and cannot leak through the holes where the pins are inserted. As shown in Figure 2-6 – Right, the pin electrodes are arranged radially such that in each cross-sectional "slice", six electrodes are dedicated to supplying the DC potential, while the other six electrodes supply the RF waveform. The RF electrodes are also wired such that alternating RF electrodes in each radial "slice" have opposite phases. Sectors one and four have nine sets of radial electrodes, while sectors two and three have eight.

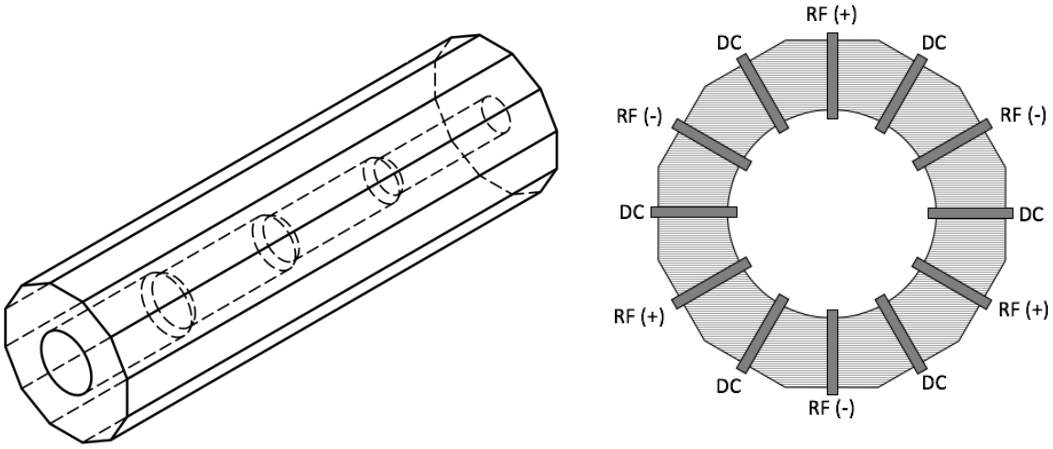

Figure 2-6. (Left) Cross section view of mobility region showing increasing diameter inner sectors. **(Right)** Schematic of mobility region electrode arrangement.

A crucial feature of the mobility region is the wiring of the electrodes that supply the DC potential. Thin, rectangular PCBs were custom built and designed with pogo pin connectors that are soldered to the bottom side of the rectangular board. The boards run the entire length of the mobility region, and the connectors are press fit into holes drilled in the top of the electrodes. (Figure 2-7). Contrasting to the entrance funnel which uses a single voltage divider, each radial set of six DC electrodes are individually addressable as one group and have a dedicated channel in the DC power supply. This allows independent potentials to be

applied to the electrodes across all four sectors, meaning non-linear DC field gradients can be generated. This also adds the capability of sequentially trapping ions in a particular sector, followed by elution and subsequent trapping further downstream. The RF waveform is also supplied to the electrodes using the same concept, with the three RF (+) and three RF (–) sets of radial electrodes connected in parallel to ensure uniform ion confinement within the hexapolar field. To simplify the wiring complexity and eliminate the need for independent RF power supplies for each sector, it was decided that the same RF waveform would be consistently applied throughout the mobility region. The electrical components and theory are discussed in more detail in Chapter 3.

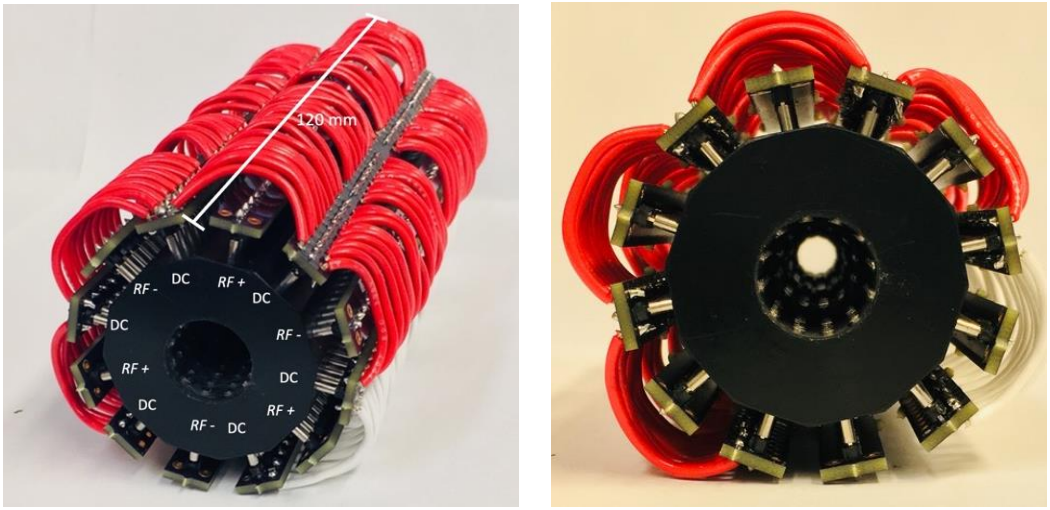

Figure 2-7. Mobility region wiring overview. **(Left)** Alternating pin electrodes for DC and RF components. **(Right)** Zoomed-in view of the pin electrodes and custom designed PCBs.

The mobility region is mounted inside the vacuum chamber using the same set of guide rods that secure the entrance funnel to the front cover of the chamber (Figure 2-8). An aluminum chassis with PEEK screws was machined to hold the mobility region in the vacuum chamber and ensure proper alignment with the funnel and transfer capillary. A recessed groove is cut into the back face of the mobility region and a FKM O-ring seals the two components. Adjustable PEEK bushings are installed to secure the entrance funnel and mobility region chassis onto the guide rods, ensuring sufficient pressure on the O-ring for a tight seal.

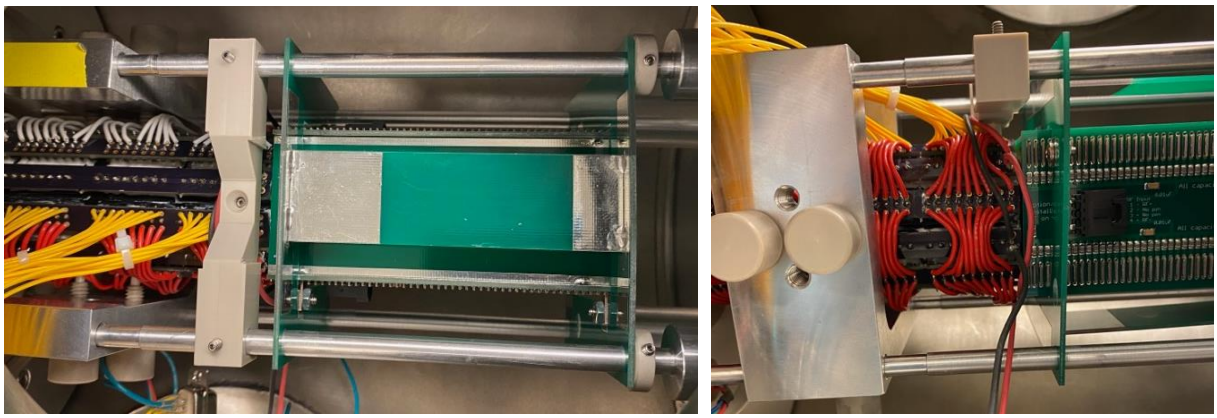

Figure 2-8. Entrance funnel mated to mobility region in front half of vacuum chamber.

2.3.4.1 COMSOL Modelling – Understanding Gas Dynamics in the Mobility Region

To better understand the gas dynamics and flow profile in the vfTIMS, COMSOL Multiphysics (v.5.6) was used to model the axial and radial gas flow profiles through the instrument. Two models were evaluated: 1) The mobility region only (Figure 2-9); and 2) The entrance funnel connected in-line before the mobility region (Figure 2-12). The simulations used the time-dependent single-phase laminar flow module in COMSOL Multiphysics that utilized the Navier-Stokes equations (Equations 2-1 to 2-3) for conservation of momentum and the continuity equation for conservation of mass for a weakly compressible flow. The system was isothermal at 293.15 K and the vfTIMS tunnel walls were given slip conditions.

$$\boldsymbol{\rho \frac{\partial \vec{u}}{\partial t} + \rho(\vec{u} \cdot \nabla)\vec{u} = \nabla \cdot \left[-p\vec{I} + K\right] + \vec{F}} \qquad \textbf{(2-1)}$$

$$\boldsymbol{\frac{\partial \rho}{\partial t} + \nabla \cdot (\rho \vec{u}) = 0} \qquad \textbf{(2-2)}$$

$$\boldsymbol{K = \mu\left(\nabla \vec{u} + (\nabla \vec{u})^T\right) - \frac{2}{3}\mu(\nabla \cdot \vec{u})\vec{I}} \qquad \textbf{(2-3)}$$

Where ρ is fluid density (kg m^{-3}), $\vec{u}$ is fluid velocity (m s^{-1}), μ is fluid dynamic viscosity (Pa s), t is time (s), p is pressure (Pa), $\vec{I}$ is the identity matrix, and $\vec{F}$ represents body forces (N m^{-3}). Fluid properties values of ρ and μ were taken from the COMSOL Multiphysics Library. Pressure constraints at the inlet/entrance of the tunnel region are set to 3.0 Torr and pressure at the outlet/exit of the tunnel was set to 1.50 Torr, which were chosen based on a combination of reports from literature and pressure measurements taken from the vacuum chamber.[41] Initial conditions (t = 0 s) considered a pressure of 3.0 Torr in the whole system

and fluid flow velocity of 0 m s^{-1}, after which a time dependent study was conducted. Once the solution of the time-dependent study stabilized, those results are considered as the steady-state conditions of the vfTIMS system. See Appendix D for a complete summary of the input parameters used for the COMSOL Multiphysics model builder wizard.

The COMSOL simulation for the first model (Figure 2-9) demonstrate that the axial and radial gas flow profiles throughout the mobility region is consistent and symmetric through each of the four sectors. As expected, the gas velocity increases as the I.D. of the sector decreases. It is worthwhile to note that in sector four, there are some inconsistencies in the axial gas flow profile closer to the walls of the tunnel (Figure 2-10). However, in the region of the cylindrical volume that the ions are expected to be confined, the flow profile remains highly consistent.[33] Inspection of the radial gas velocity profile (Figure 2-11) also suggests that velocity in the central region (±4 mm) of each sector is near homogenous, while the gas velocity decreases in magnitude near the walls. This results in a parabolic radial flow profile because of the increased friction of the gas molecules near the walls. Ultimately, the basis of the mobility separation lies in compensating the drag force (which is proportional to the gas velocity) with the opposing force exerted by the electric field. To ensure the best resolution and minimize the spread of ions in the analyzer, axially, the gas flow should be near constant through each of the four sectors. Radially, the gas velocity in the central region of each sector is expected to be uniform.

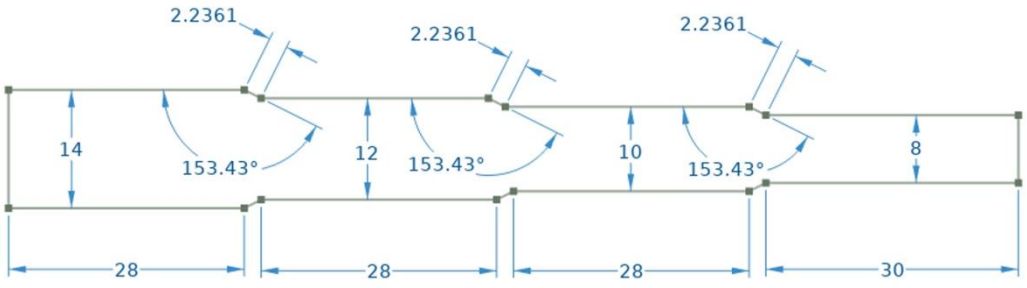

Figure 2-9. vfTIMS mobility region COMSOL model dimensions. All dimensions in mm.

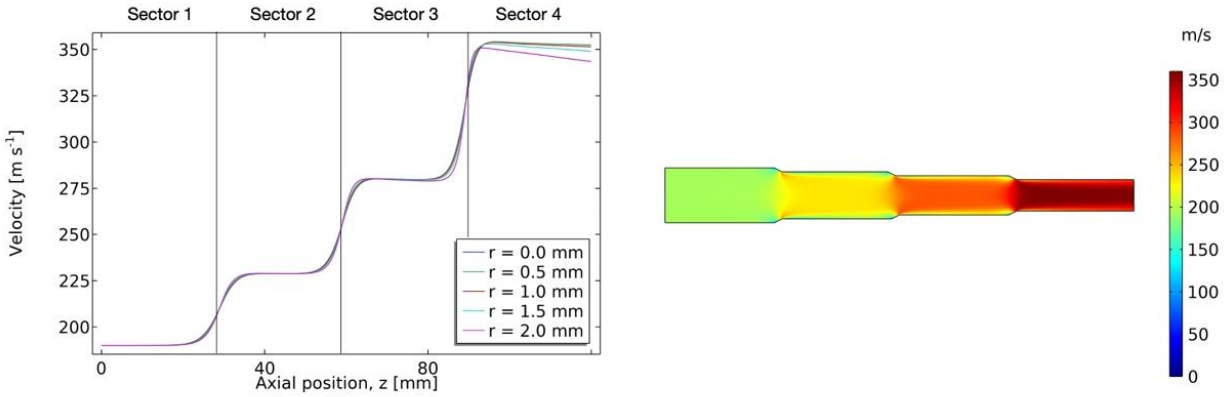

Figure 2-10. COMSOL simulation for the axial gas velocity through the mobility region.

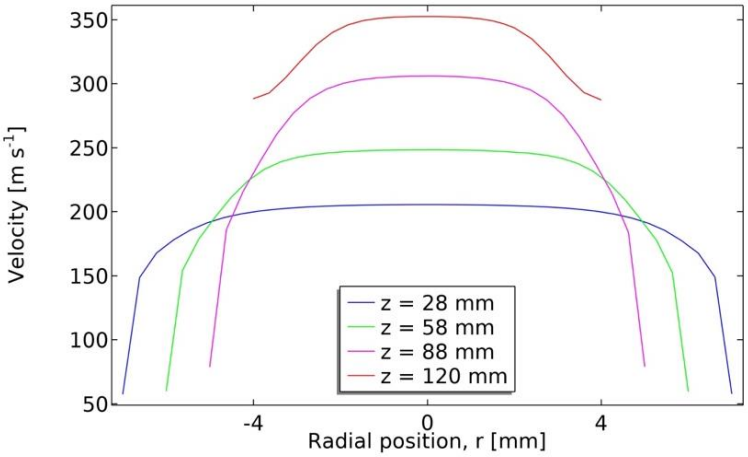

Figure 2-11. COMSOL simulation for the radial gas velocity through the mobility region.

The COMSOL simulation for the second model (Figure 2-12) incorporates the entrance funnel prior to the mobility region and provides more information about the complexity of the gas velocity profile generated inside the instrument. Specifically, the main challenge to generating the same uniform flow profile as depicted in the first COMSOL model is the slight offset between the I.D. of the last ring electrode at end of the entrance funnel, and the I.D. of the first sector of the mobility region. This offset leads to a perturbation of the axial gas flow at the front of the mobility analyzer caused by the gas velocity initially increasing before significantly decreasing due to gas expansion through the exit of the entrance funnel into the first two sectors of the mobility region (Figure 2-13). Due to this turbulence effect, the first sector is not

used for ion mobility separation since the inhomogeneity of the gas flow will impact ion focusing. Improvements that have been suggested for future prototypes to mitigate this are to match the orifice dimensions of the last lens of the funnel with the mobility region or install a straight tube lens between the two components to ensure the axial flow profile is well defined and consistent throughout.

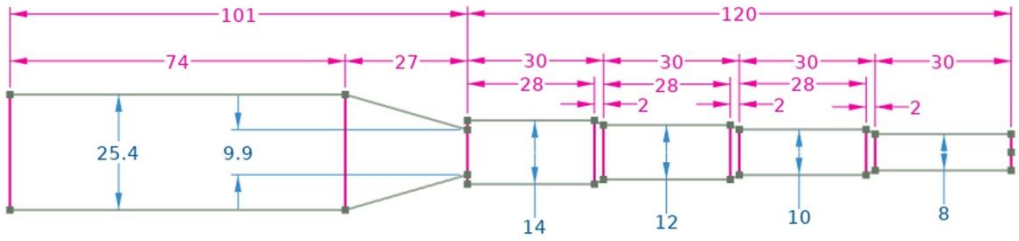

Figure 2-12. vfTIMS entrance funnel and mobility region COMSOL simulation dimensions. All dimensions in mm.

The radial gas velocity profile of the second COMSOL model (Figure 2-14) more closely matches the results obtained from the first model. However, there is a slightly smaller volume (± 3 mm) that the ions can occupy where the gas velocity is near homogenous in each of the four sectors. This is especially apparent in sector 4 where the I.D. is the smallest. The effect of the I.D. mismatch between the entrance funnel and first two sectors of the mobility region is also observed in the magnitude of the radial gas velocity. Inspection of the radial gas velocity plot shows the magnitude of the gas velocity is essentially equal in sector 1 and 2 even though the I.D. has decreased by 2 mm. This finding serves as further evidence that the first sector cannot be used for sequential mobility separations because the drift force exerted by the gas does not increase uniformly between adjacent sectors at the front end of the mobility region. As mentioned above, future iterations of the instrument would focus on redesigning the entrance funnel to mobility region interface. By matching the I.D. of the conductance limit lens with the entrance of the mobility region, a much smoother flow profile would be established in both the axial and radial dimension. This would limit the gas turbulence observed *in silico* as the gas expands into the larger orifice and ensure homogenous gas velocity in each sector of the mobility region. Consequently, this improvement would improve the overall performance of the instrument.

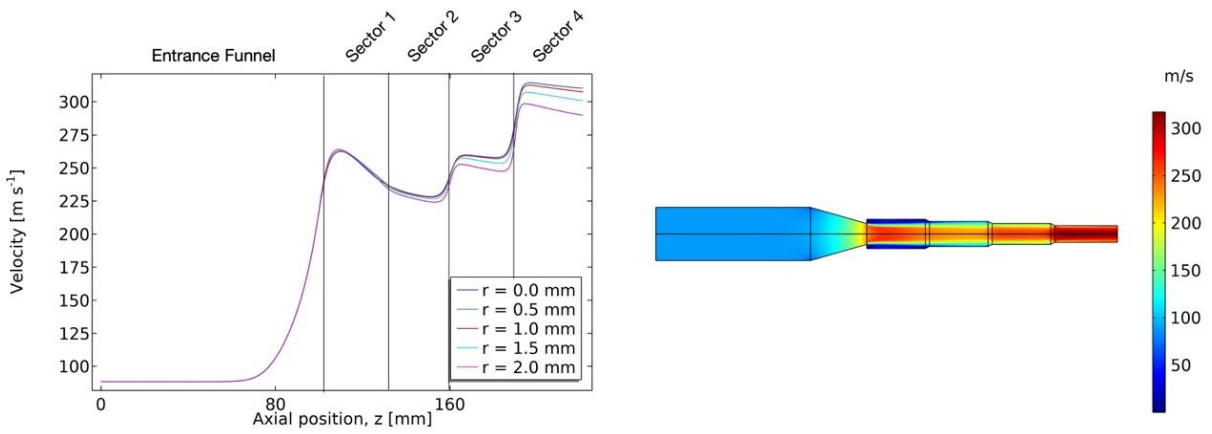

Figure 2-13. COMSOL simulation for the axial gas velocity through the entrance funnel and mobility region.

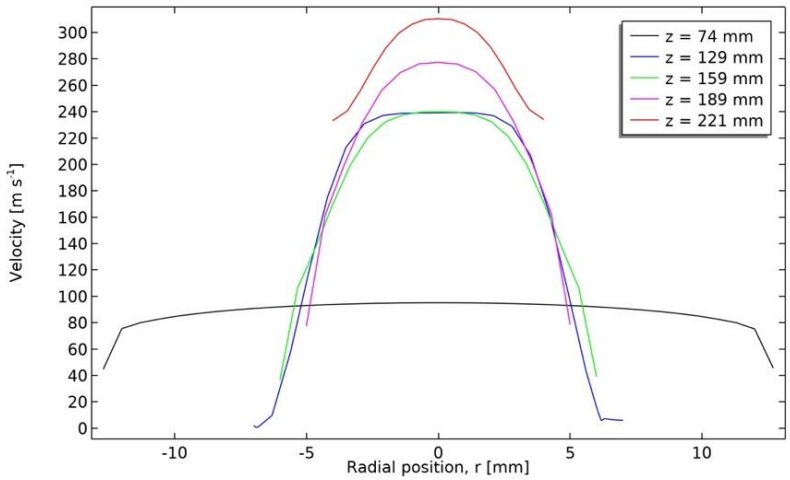

Figure 2-14. COMSOL simulation for the radial gas velocity through the entrance funnel and mobility region.

2.3.5 Detector/Data Acquisition

Once ions have transited through the transfer capillary, entrance funnel, mobility region, and tube lens, the total ion current is measured using a Faraday detector (GAA Custom Electronics, Washington State, USA) based closely on the design by Reinecke and Clowers.[99] The Faraday detector directly measures the current produced by ions striking the surface, and is connected to a transimpedance amplifier (*e.g.*, electrometer) that converts the ion current (nA) into voltage (V) (Figure 2-15). The transimpedance amplifier used in the

vfTIMS instrument has the gain set to 10^8. In this configuration where the detector functions as a positive ion collector, the loss of secondary electrons appears to the electrometer as an additional ion.[100] The DC biased grid installed in front of the surface of Faraday detector ensures that secondary electrons cannot escape and affect the measured current. The grid is biased to +3V for all experiments reported in the thesis.

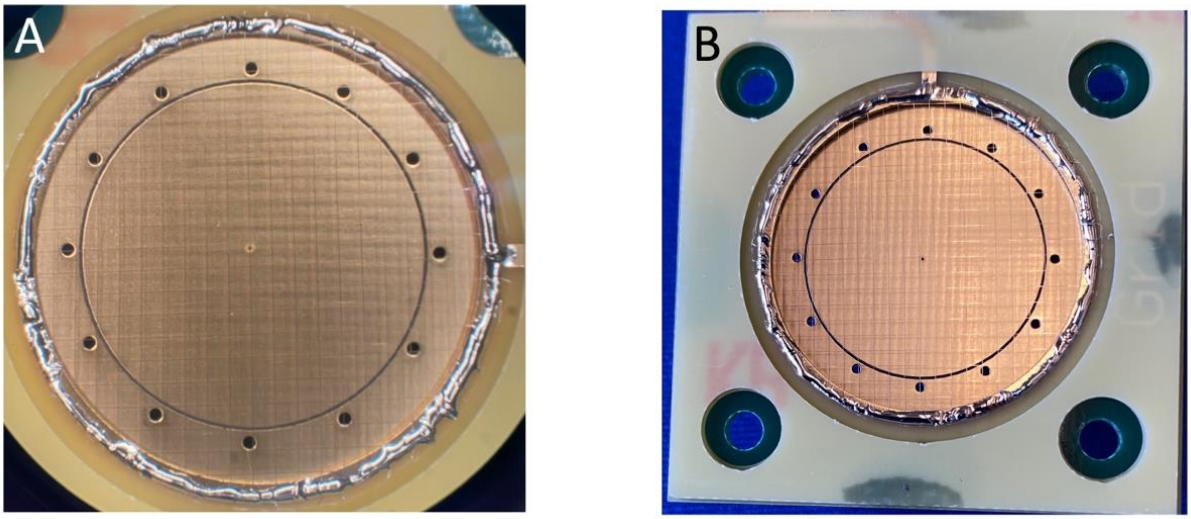

Figure 2-15. Custom built Faraday detector with DC biased grid. The active detection area of the Faraday detector is ~5.0 cm^2.

The detector is mounted directly to the backside of the PEEK pressure divider with screws that connect to the aluminum guide rods in the front half of the chamber (Figure 2-16). A FKM O-ring in a recessed groove ensures that a gas-tight seal is created is between the outer body of the detector and the pressure divider. An SMA cable connects to the backside of the detector, runs through a vacuum feedthrough on the back cap of the chamber, and connects to the electrometer. The output from the electrometer is then split off with a BNC tee, and ion current data can be acquired two ways. The first method uses the built-in ADC installed in the modular intelligent power source and provides an easy real-time visualization of the total ion current. The refresh rate on the ADC is relatively low (~ 0.5 s) so it is best suited for simple measurements and assessment of nanoESI spray stability. The second method uses a high-resolution DPO 5054B oscilloscope (Tektronix, Ontario, CA) to acquire data from the electrometer. This is a much more suitable choice for data acquisition because the refresh rate is orders of magnitude faster, the oscilloscope

can be triggered from the power supply digital outputs, and data .txt files with oscilloscope traces can be exported for further data processing. More details about the data acquisition and the event generator will be described in Chapter 3.

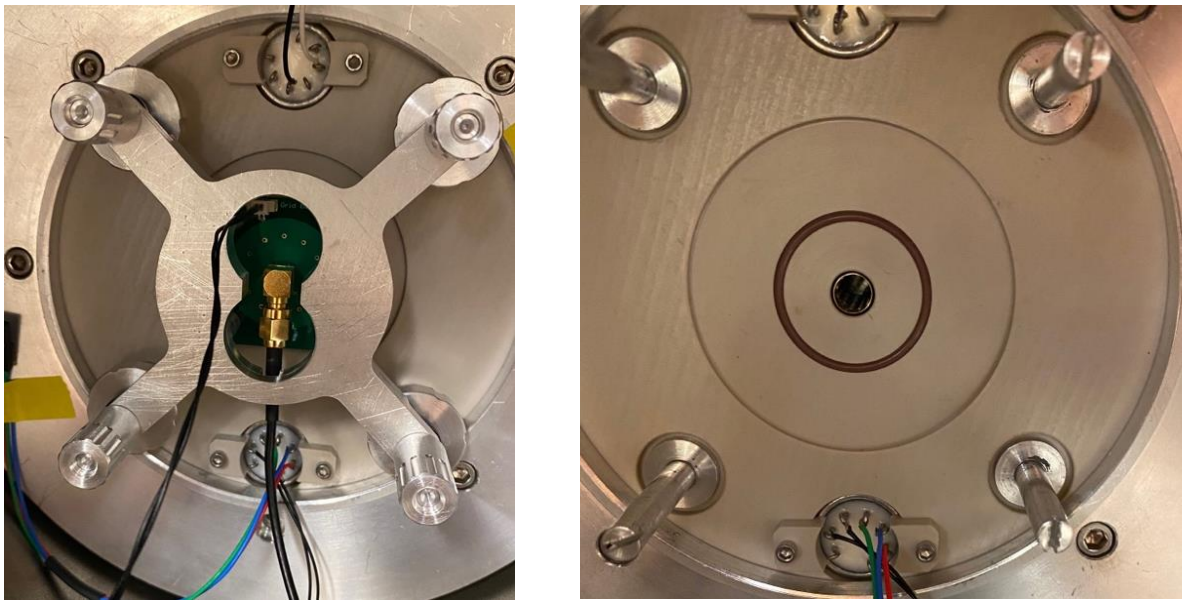

Figure 2-16. (Left) Custom built hardware mount for the Faraday detector in the back half of the vacuum chamber with pressure divider. **(Right)** Back side of pressure divider with tube lens exposed.

2.4 Conclusions

In conclusion, the main objective of the first phase of the project was to construct the vfTIMS prototype in the laboratory. The instrument incorporates multiple commercially available and custom-built components into a single unified system. Simulations were performed using COMSOL Multiphysics to characterize the gas dynamics and flow profile through the entrance funnel and mobility region. Once construction and *in silico* testing were complete, the next stage of the project focused on assembling the electrical components and power supplies that drive the instrument. This will be covered in considerable detail in Chapter 3. Overall, the main research objective was achieved, however, this was only the first step towards the ultimate goal of developing a robust, functioning instrument.

Chapter 3: Electronics Overview and Software Development

3.1 Preamble

This chapter has not yet been published. The majority of the technical information related to the electronics described in this chapter will be used during preparation of a manuscript for submission to Review of Scientific Instruments in 2024. The two MIPS units were custom designed and manufactured by Gordon Anderson based on the technical specifications required for the vfTIMS. The MIPS units were installed in the lab and tested by Daniel Rickert with technical assistance from Gordon Anderson. The variable RF power supply apparatus was designed and built by Krunomir Dvorski and assisted by Daniel Rickert. All testing and troubleshooting of the variable RF power supply was done by Daniel Rickert. The RF modelling using COMSOL Multiphysics was done by Daniel Rickert and Emir Nazdrajić. The MIPS control software was designed by Gordon Anderson. Modifications/improvements to the MIPS control software and implementation of custom MIPS scripts were done by Daniel Rickert and Gordon Anderson. The Python code used to process vfTIMS data was written by Cailum Steinstra with technical input and assistance from Daniel Rickert. Janusz Pawliszyn and Scott Hopkins were responsible for conceptualization of the project, project supervision, and funding acquisition.

3.2 Electronics Overview

After building the instrument and installing it in the laboratory, the next phase of the project focused on integrating the electronics with the vfTIMS hardware and the development of a user interface to run the instrument. Multiple commercial and custom-built pieces of equipment are integrated to form a unified electrical apparatus that runs the vfTIMS (Figure 3-1). See Appendix F for a detailed description of the electrical configuration. The electronics that drive the instrument are configured as follows: The function generator generates a sinusoidal waveform that is routed to the phase splitter which splits the positive and negative phases of the sine wave into separate waveforms. After the splitter, both phases are amplified by the high-voltage high-frequency power amplifier that outputs the RF waveform in the mobility region. The

dipolar RF waveform applied to the entrance funnel is generated independently by a high Q head with a RF driver board installed in one of the modular intelligent power source (MIPS) units. All the DC potentials used throughout the instrument are supplied by multiple (*e.g.*, five) 8-channel DC bias modules that are installed across two MIPS systems. The high-voltage DC potential used to generate the electrospray is also delivered by a compact high-voltage power supply that is also installed and controlled through the MIPS. As described in detail in Chapter 2, the ion current detected by the Faraday plate is converted to voltage by a transimpedance amplifier that is connected directly to the oscilloscope. The oscilloscope can be operated in *run mode* where it is continuously displaying the ion current or in *trigger mode* where it is programmed to accept a trigger signal to start data acquisition.

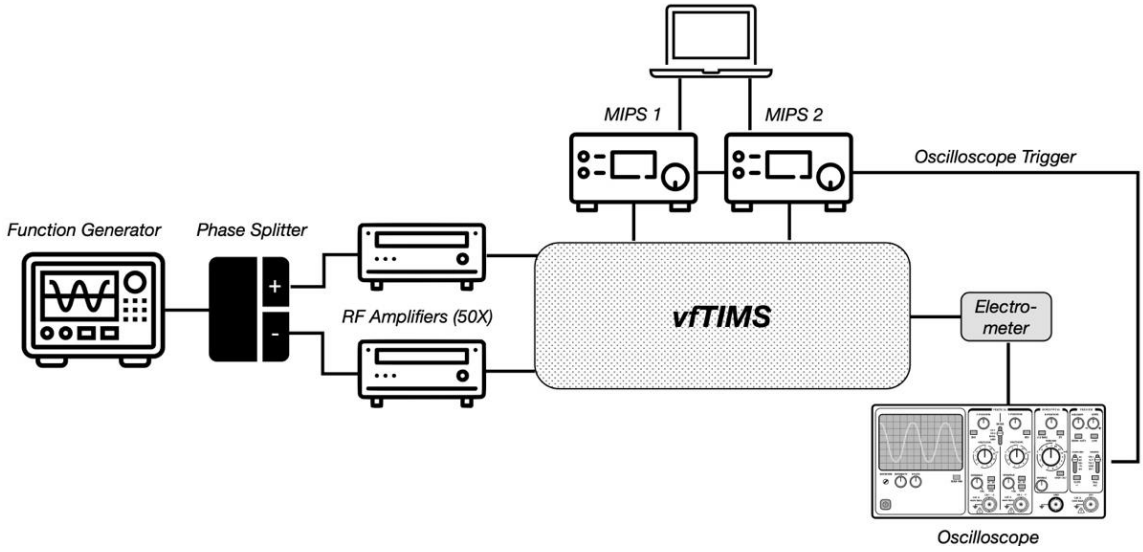

Figure 3-1. vfTIMS electronics overview.

3.2.1 Modular Intelligent Power Sources (MIPS)

Two MIPS units serve as the central hub that integrate most of the electronics that drive the instrument (GAA Custom Electronics, Washington State, USA). The MIPS systems produce DC and RF voltages that are designed for custom ion mobility applications. Within each MIPS module is a powerful embedded controller running at a clock frequency of 84 MHz. This processor controls the output voltages while simultaneously monitoring the output readbacks to ensure signal stability and proper operation.

Additionally, one of the MIPS supplies power to the barrel heaters that maintain the temperature of the transfer capillary in the inlet block. The two MIPS (*e.g.*, MIPS-1 and MIPS-2) are configured with different internal components to balance the electrical load across both systems as well as considering physical space constraints that limit the number of 8-channel DC power supplies that can be installed in a single MIPS.

MIPS-1 is exclusively used to deliver programmable DC potentials to the pin electrodes embedded within the body of the mobility region. These pin electrodes generate the axial electric field used to trap ions within the inner cavity of the analyzer. Each MIPS case can hold a maximum of four 8-channel subunits that output a ±60V potential. If required, a DC power supply subunit can be biased to go as low as –120V or as high +120V. MIPS-2 houses a wider range of electrical subcomponents. Specifically, an additional 8-channel DC power supply (±60V) is routed from MIPS-2 to MIPS-1 because there are two additional DC channels in the mobility region that cannot be supplied by MIPS-1 alone. The wiring for the 34 DC channels is grouped together and connect to the vacuum chamber with a single 35-pin D-sub connector (Digikey, Minnesota, USA). MIPS-2 also houses a second 8-channel DC power supply subunit that generates the potentials for the entrance funnel (*e.g.*, Voltage In, Voltage Out, Conductance Limit) and ion transfer capillary. The wiring for the entrance funnel connects to the vacuum chamber using a smaller, 15 pin D-sub connector (Digikey, Minnesota, USA), while the DC potential applied on the transfer capillary connect via a single BNC connector on the back of MIPS-2. MIPS-2 also controls a custom-built RF high Q head power supply that delivers two equal amplitude, 180° out of phase signals that radially confine ions in the entrance funnel. The Q factor in the RF high-Q head represents the efficacy of a given capacitor to efficiently charge and discharge. A theoretically "perfect" capacitor would have no loss (*e.g.*, voltage drop) and completely charge/discharge during every RF cycle.[100,101] For IMS applications that utilize RF confinement with high frequencies and large peak to peak voltages, minimizing the voltage drop is crucial.[102] Besides the various DC and RF components, MIPS-2 drives the barrel heaters, type-K thermocouple and PID controller for the ion transfer capillary; as well as the variable high-voltage ESI power supply unit outputting between 0 and ±4kV to generate the electrospray. Lastly, an ADC is installed

in MIPS-2 that is connected to the electrometer via a standard BNC to SMA tee connector and provides a secondary means to record the total ion current on the Faraday detector without relying on the oscilloscope for data acquisition.

Presently, the electrical infrastructure (*i.e.*, RF and DC wiring and power supplies, vacuum feedthroughs, internal mounting components, MIPS control panel functionality) is available to connect a second ion funnel at the end of the vfTIMS mobility region. When installed. this funnel would be primarily used to focus ions as they transit towards the detector. However, it could also be used as an ion funnel trap to accumulate ions eluting from the mobility region which would increase the sensitivity of the measurements.[98,103] While this idea was considered during the early stages of the project, technical issues with sealing the exit funnel to the back side of the pressure divider in the vacuum chamber, and concerns about synchronizing the different MIPS events needed to make the ion funnel trapping work properly led to the idea being abandoned. Future iterations of the instrument will inevitably incorporate a second ion funnel and other ion optics to interface the vfTIMS with a high-performance mass analyzer (*e.g.*, TOF-MS).

3.2.2 Custom RF Power Supply with Variable Voltage and Frequency Capabilities

One of the unique features of the vfTIMS is the hexapolar RF confining field generated throughout the mobility region. The hexapolar field differs from the conventional TIMS analyzer which uses a quadrupolar RF field to confine the ions in the center of the tunnel.[27,41] As shown in Figure 3-2, as the RF field increases from quadrupolar to dodecapolar, the confining RF field remains flatter and closer to zero further from the trap axis. In other words, by increasing the number of electrodes that generate the field, ions can occupy a larger near-zero field region near the flow axis of the device.[104,105] The hexapolar confinement field configuration was chosen for the first prototype to increase the total number of ions which can be loaded into the analyzer, thus increasing the sensitivity, while simultaneously decreasing space-charging effects which can limit mobility resolution.[37] As discussed in Chapter 2, care must be taken to not allow the ions to diffuse too far radially from the center because of the decreased gas velocity near the walls of the mobility

region. If the plateau portion of the parabolic radial flow profile is too narrow, issues may arise with peak spreading since the gas velocity is not uniform further from the center of the flow axis.[24]

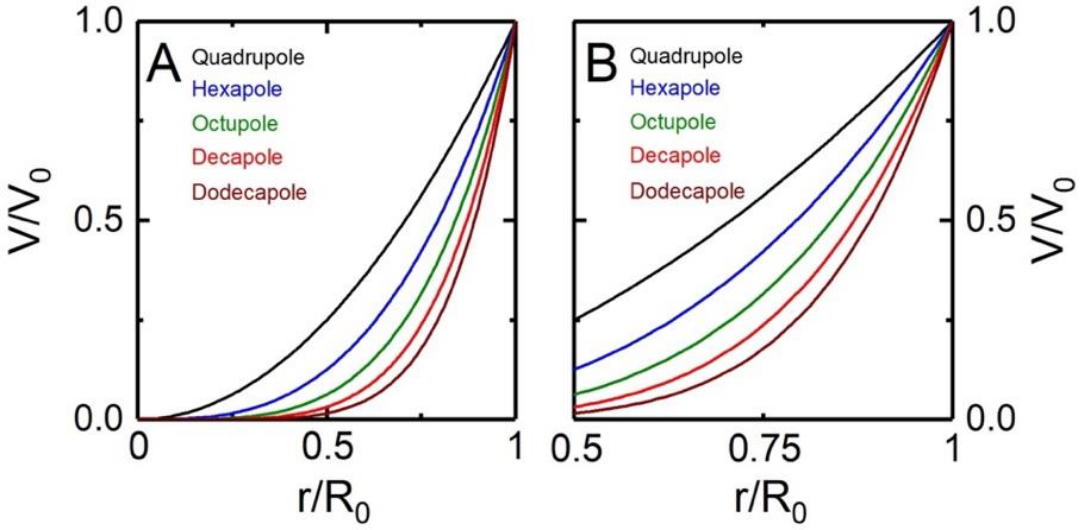

Figure 3-2. Comparison of different RF confinement schemes. **(Left)** The radial electric potential as a function of distance from the flow axis for quadrupolar, hexapolar, octopolar, decapolar, and dodecapolar electrode arrangements. **(Right)** A zoom of the region near the radius ascribed by the confining electrodes.

To produce the hexapolar RF field in the mobility region of the vfTIMS, a custom instrumental set-up capable of variable frequency and peak-to-peak voltage outputs was constructed with the assistance of the University of Waterloo Science Technical Services Electronics Shop. The initial sinusoidal waveform is generated by an AFG1022 arbitrary function generator (Tektronix, Ontario, CA) with 0 ±5V variable output and adjustable frequency. The RF signal is then split with an in-house designed "phase splitter" to produce two 180° out of phase signals. To increase the RF voltage to the required amplitude, each phase is routed to a dedicated TREK 2100 HF high-frequency 50× amplifier (Advanced Energy, Colorado, USA) with an output voltage range between 0 and 300 Vpp. A portable, touch screen ADS1013D oscilloscope (YEAPOOK, Shenzen, CN**)** with 10× oscilloscope probes is connected via BNC tees at the vacuum feedthrough plate to continuously monitor both RF phases being supplied to the boards that connect to the electrodes in the mobility region. An example of the voltages needed to output a final voltage of 150 Vpp are as follows: the function generator outputs a single 1.5 Vpp pure sine wave signal to the phase splitter;

the phase splitter outputs two 180° out of phase sine waves, both with a magnitude of 3 Vpp; each phase is then amplified 50× by the TREK amplifier for a final output of 150 Vpp.

The advantage to the in-house designed RF amplifier arrangement is the adjustable frequency and voltage that is applied through the mobility region of the vfTIMS. It has been extensively reported in the literature that the frequency/voltage combination applied to the drift/mobility region impacts the transmission of ions with different masses. Thus, it is critical that the vfTIMS has this functionality to achieve optimal transmission for a wide *m/z* range of analytes.[26,106] This configuration differs from the RF high-Q head utilized by the entrance funnel. The high-Q head is tuned to a specific resonant frequency to achieve a balanced output at the optimized voltage.[105] If the frequency is adjusted, then the output voltage will decrease since the RF coil inside the high-Q head is not resonating at the optimal frequency. One complication to the variable frequency RF amplifiers is the voltage drop when the system is under load as the frequency increases. In Figure 3-3, five different output voltages between 50 and 250 Vpp, with a range of frequencies between 100 and 1500 kHz, were measured to calibrate the effective voltage being applied to the mobility region at a corresponding frequency. As expected, at low frequencies (*i.e.*, 100 to 500 kHz), there is a marginal decrease in the effective peak to peak voltage. As the frequency increases beyond 500 kHz the reactance in the circuit (*i.e.*, the opposition presented to alternating current by inductance and capacitance) also increases proportionally, and since the resistance is constant, a more significant voltage drop is observed.[101] To ensure measurement consistency, during routine operation of the instrument the effective RF voltage is continuously monitored using the portable touch-screen oscilloscope.

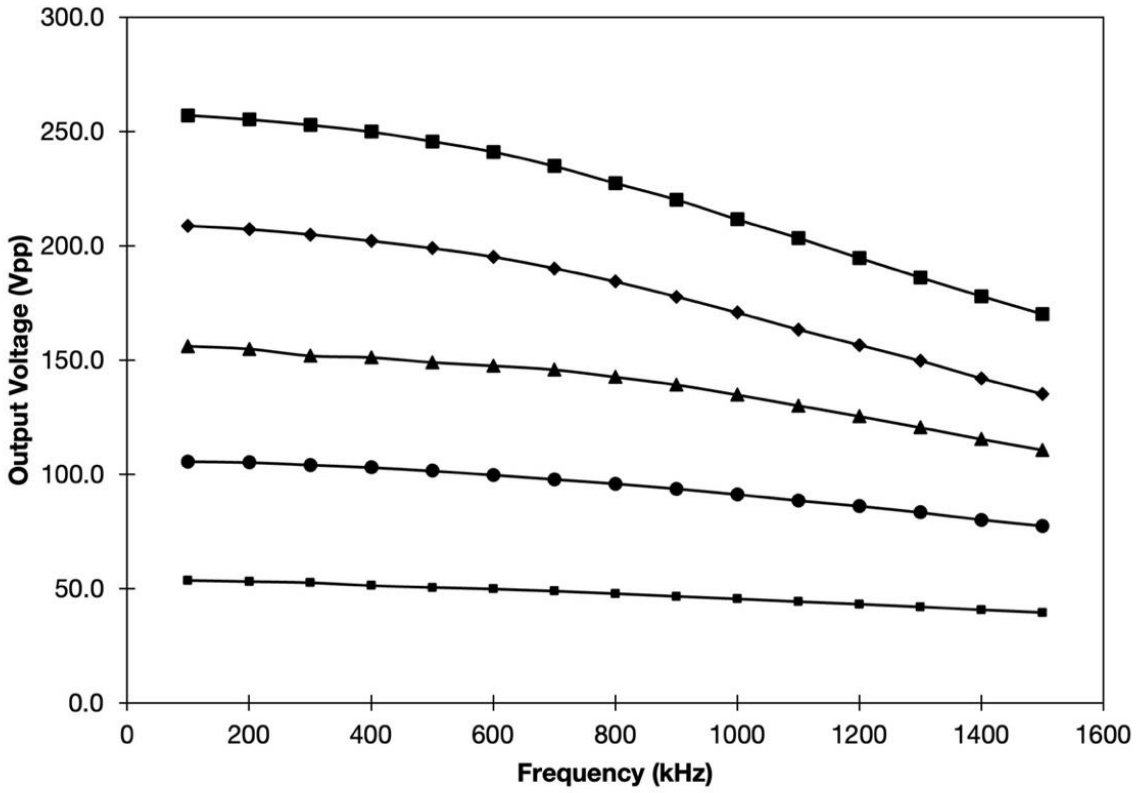

Figure 3-3. Evaluation of the effective RF amplifier frequency/voltage response for the custom-built RF power supply.

While benchmarking the performance of the in-house designed RF power supplies, a technical issue was identified that limits the maximum voltage/frequency that can be applied to the mobility region. Despite purchasing identical TREK amplifiers and using the same length of identical shielded BNC cables, a minor phase shift between the outputs at high frequencies was observed. At 300 kHz, the observed phase shift between the two amplifiers is ~1.5% for each of the voltages measured in Figure 3-3. At 500 kHz, the shift becomes more pronounced, with a ~3% shift observed. The shift continues to increase at higher frequencies, with a ~7.5% phase shift observed at 1200 kHz. To mitigate this issue and guarantee a balanced output, one of the amplifiers could be calibrated with an offset. Unfortunately, this calibration would not be dynamic, and would only be applicable at a specific frequency. It may be feasible to construct a more advanced calibration module with predetermined offsets for different frequencies, however, this has not been explored in detail at this juncture. Another alternative to mitigate this issue could include adding an air gapped

capacitor unit between each of the RF amplifiers and the instrument to ensure that both RF signals are balanced.

3.2.3 COMSOL Modelling – Characterizing the Hexapolar RF Waveform

To better understand the confining effects of the RF waveform applied throughout the mobility region, a model was built using COMSOL Multiphysics (Figure 3-4). This model was adapted from the COMSOL Application Library and was used to perform the simulations of the electric field using the Electrostatics package from the AC/DC module.[107] See Appendix E for a complete summary of the input parameters used for the COMSOL Multiphysics model builder wizard. An electrostatic voltage is applied to the electrodes at each cross-sectional view of each segment of the vfTIMS and is defined as a function of time and represented with the following equations (Equation 3-1 and 3-2):

$$\boldsymbol{RF}\,(+) = \boldsymbol{V sin}\,(\boldsymbol{\omega t}) \qquad \textbf{(3-1)}$$

$$\boldsymbol{RF}\,(-) = -\boldsymbol{V sin}\,(\boldsymbol{\omega t}) \qquad \textbf{(3-2)}$$

where RF (+) and RF (–) represent electrostatic voltage applied to electrodes, V represents the alternating current voltage (V), ω represents the frequency (s^{-1}; Hz), and t represents time (s). There are 12 electrodes in each cross-sectional view in each segment of vfTIMS, for which RF (+) and RF (–) were applied in alternating fashion to 3 electrodes (6 total). Alternating current electric fields were solved using the following equation:

$$-\boldsymbol{\nabla} \cdot (\boldsymbol{\sigma} + \boldsymbol{j\omega\varepsilon_0\varepsilon_r})\boldsymbol{\nabla V} = \mathbf{0} \qquad \textbf{(3-3)}$$

where ε_0 represents permittivity of free space (F m^{-1}) and ε_r represents the relative permittivity of the medium, which is taken as 1 for this application. In Equation 3-3, σ represents the electrical conductivity taken as 0 in this application.

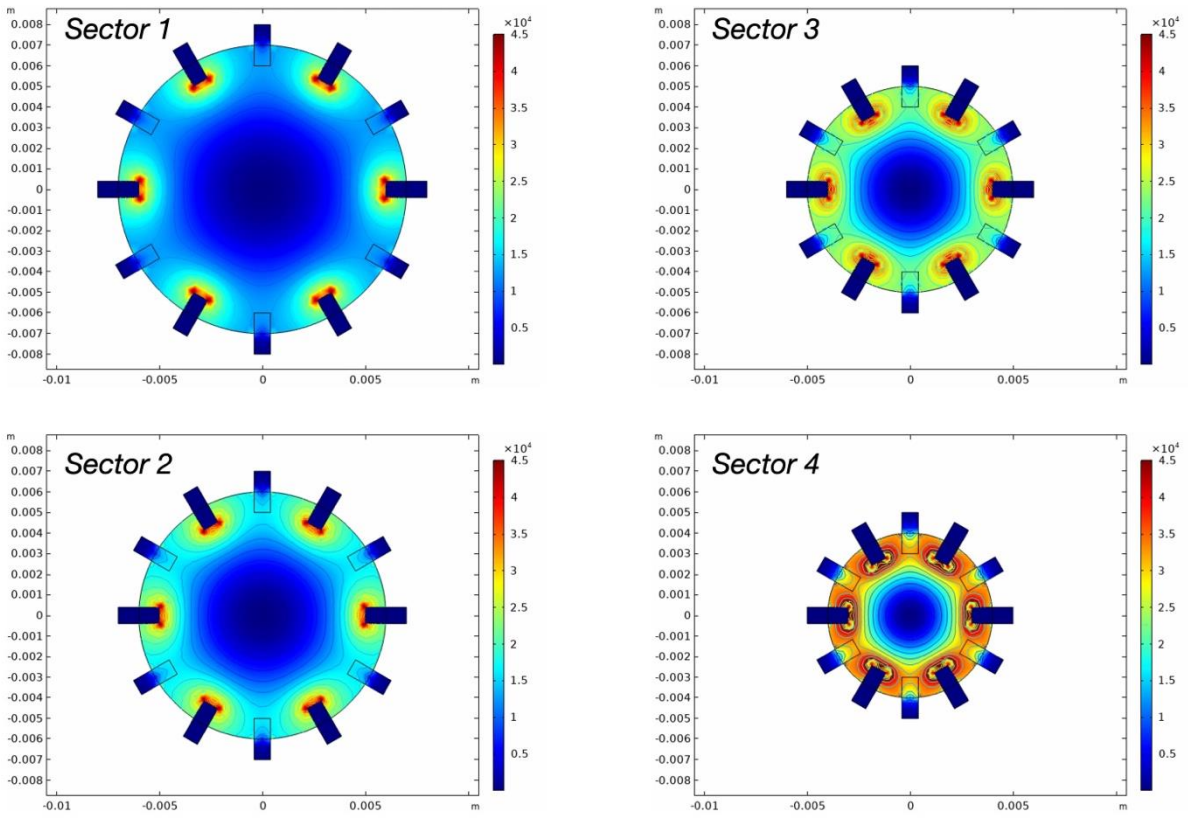

Figure 3-4. Simulation of the normalized RF electric field (V/m) inside each sector of the vfTIMS mobility region. The simulation used 100 Vpp and 750 kHz as inputs. **(Upper Left)** Sector 1. **(Lower Left)** Sector 2. **(Upper Right)** Sector 3. **(Lower Right)**. Sector 4.

The results of the COMSOL model in each of four sectors of the mobility region is shown in Figure 3-4. The field free region (*i.e.*, the area where the ions are confined by the RF field) along the central axis decreases proportionally as the I.D. decreases in the inner cavity from Sector 1 to Sector 4, but more importantly, the field free region in each sector is smaller than the plateau segment of the radial gas velocity profile computed in Chapter 2 (Figure 2-14). In other words, ions need to be confined by the hexapolar RF electric field in a region inside the analyzer where the radial gas velocity is nearly homogenous. Ions are trapped axially within the mobility region when the force applied by the carrier gas matches the opposing force exerted by the DC electric field. In an ideal experimental scenario, each subpopulation of mobility separated ions will experience a uniform driving force from the gas throughout each sector of the mobility region with no deviation in the radially gas velocity. If significant radial diffusion does occur due to insufficient RF confinement, the ion cloud will spread further from the center of the flow axis. Ions closer

to the walls will experience a weaker driving force from the gas compared to ions near the center. During the elution stage of the TIMS experiment when the electric field gradient is decreased, ions near the walls of the analyzer will elute after ions with the same mobility that were confined closer to the center. This leads to a wide distribution of ions with the same mobility reaching the detector, appearing experimentally as a broad peak. Minimizing the effects of radial diffusion is one of the most important factors for maximizing the resolution of the instrument.

3.3 Instrument Control w/ GAA Custom Electronics & MIPS

Both MIPS systems are connected to a laptop computer using standard USB 2.0 connections. The vfTIMS is operated with a customized control panel that integrates the different hardware modules installed in both MIPS and provides real-time feedback to the user of all the voltages being applied throughout the system. The control panel acts as a user-friendly graphical user interface (GUI) that reads a configuration (.cfg) file located in the main MIPS directory of the PC. All of the electrical channels (DC and RF) are defined in the .cfg as independent variables with unique identifiers, and the .cfg file also links other secondary script (.scrpt) files that define the functions of clickable buttons or fillable fields. Readbacks of the voltages being applied throughout the system are displayed on the control panel, and the real-time ion current from the Faraday detector is also displayed when the electrometer is powered on. The control panel can be easily modified for different applications, instrumental configurations, or user preferred visual layouts by editing the .cfg file. See Appendix B for the .cfg file used for the vfTIMS.

In Figure 3-5, the custom vfTIMS interface is labelled (A to O) to highlight the various features that have been implemented. The DC voltages have a fillable field to input the desired voltage, and the corresponding readback is displayed in the green box to the right of the input. If the voltage goes above the defined safe input limit, the box will turn red. The refresh rate for the readbacks can be modified in the preferences menu of the MIPS software, however decreasing the refresh rate below 0.5 s leads to intermittent issues with the MIPS application crashing or becoming temporarily non-responsive. To mitigate this, the refresh rate is usually set to 1 s. The control panel features are summarized in Table 1.

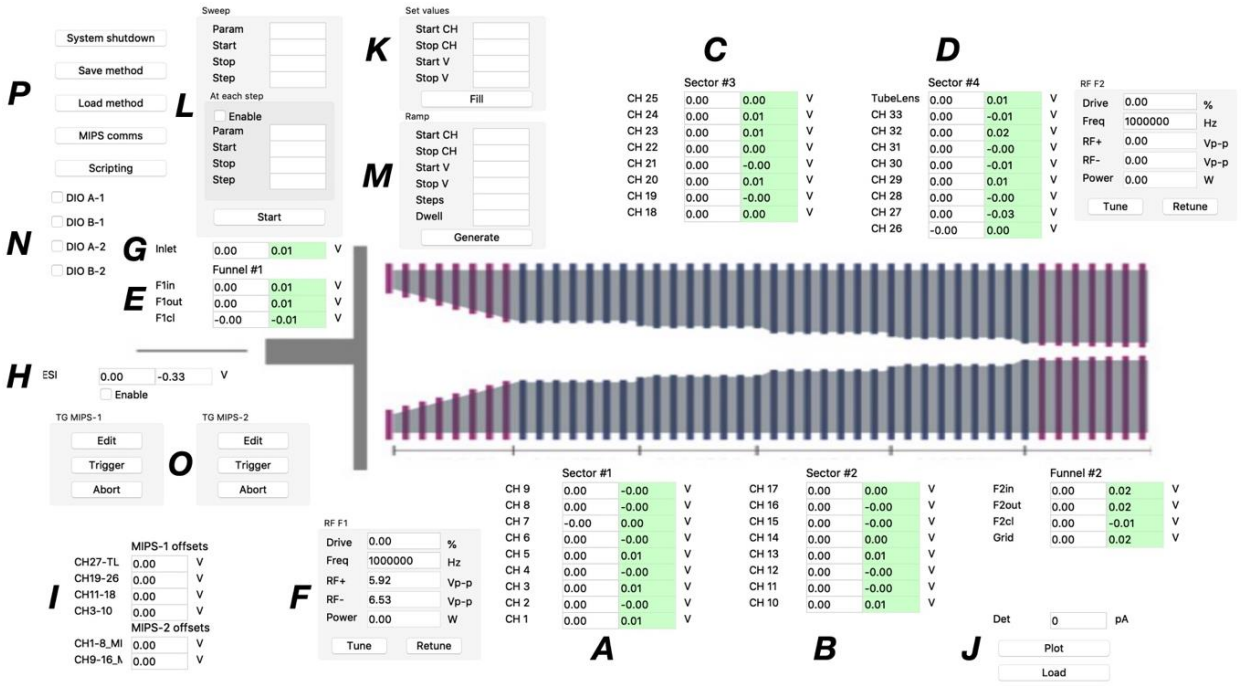

Figure 3-5. MIPS hardware GUI control panel. The white box next to parameter is the input field and the green box is the real-time readback. (A-D) DC voltage inputs for mobility region. (E) Entrance funnel voltage inputs. (F) Entrance funnel RF inputs. (G) Ion transfer capillary voltage input. (H) ESI voltage input. (I) MIPS DC offsets. (J) Faraday detector ion current output. (K) DC gradient fast fill function inputs. (L) DC voltage sweep function inputs. (M) DC ramp function inputs. (N) MIPS digital input/output controls. (O) MIPS timing generator controls. (P) Master MIPS control functions.

Table 1. Summary of features on the vfTIMS ontrol panel.

Label	Feature	Description
A – D	Mobility Region Voltage Inputs	All DC voltages applied to the pin electrodes in the four sectors of the mobility region are controlled by inputting the desired voltage here. Each electrode is defined as a specific channel (*e.g.,* CH-1) that corresponds to a channel in one of the DC power supply subunits.
E	Entrance Funnel Voltage Inputs	All DC voltages applied to the entrance funnel are controlled here. F*in* and F*out* set the electric field gradient in the funnel, and F*cl* controls the last lens of the funnel, referred to as the conductance limit.
F	Entrance Funnel RF Inputs	The RF voltage applied to the funnel is set by inputting a desired drive percentage. This will correspond to a voltage output at the tuned frequency. During installation, the Tune button runs a pre-set tuning protocol at 10% drive to determine the optimum resonant frequency for maximum voltage output. Periodically, the user can select the Retune button to quickly recalibrate the high Q head to ensure optimal performance.

G	Transfer Capillary Voltage Input	Input for the desired DC voltage applied to the ion transfer capillary to ensure maximum transmission of ions from the electrospray needle into the entrance funnel.
H	ESI Voltage Input	Input for the high voltage applied to electrospray needle.
I	MIPS DC Offsets	Input fields to change the offsets on individual 8-channel DC power supplies. The offset input range is ±60 V.
J	Faraday Detector Output	Ion current measurements from the Faraday detector are displayed here in picoamps. The Plot button plots the real time ion current in a separate window where it can be saved as a .plot file. The .plot file can also be exported to a .txt file that displays time on the x-axis and ion current on the y-axis. The Load button opens .plot files.
K	DC Gradient Fast Fill Function	This function enables a .scrpt file that sets the input field of the selected set of electrodes with DC voltages for the desired range. For example, to set electrodes 1 through 9 (CH-1 to CH-9) with a DC voltage gradient of 10V to 20V, the user would input CH-1 in Start CH, CH-9 in Stop CH, 10 for Start V, and 20 for Stop V. Pressing fill will populate the input boxes for the specified channels with evenly spaced voltages that match the desired range.
L	DC Voltage Sweep Function	This function enables a .scrpt file that "sweeps" a selected DC channel from a start voltage to a stop voltage. The Step box defines the voltage step. The dwell time is defined by the refresh rate in the Preferences menu. The lower panel can be used to sweep a second channel within the initial sweep experiment if enabled by the check box. This panel has the same functionality as outlined above. For example, when enabled, the F1*cl* could be ramped from 10V to 30V, and at each voltage step, CH-1 will ramp between 10V and 30V. If the second sweep function is enabled, the latter will run through the entire sweep sequence that has been defined in the lower panel for each step of the sweep parameter of the former. Once the variables have been inputted into the sweep panel, pressing start will open a new window displaying the ion current output as the sweep sequence runs. This file can be exported to .txt with the voltage step as the x-axis and the ion current as the *y*-axis
M	DC Voltage Ramp Function	The ramp function enables a .scrpt file that runs in conjunction with the DC gradient fast fill function (***K***) to run a "ramp down" event that incrementally decreases the DC voltages across a selected set of electrodes. The initial voltage gradient for the ramp is set with ***K***, and then the selected channels to be ramped are defined using the Start CH and Stop CH boxes. The final voltage ramp is defined using the Start V and Stop V boxes, the number of steps taken to reach the final voltage gradient

		is defined with Steps, and the dwell time in milliseconds is defined by Dwell. This script can only be run in conjunction with an event defined by the MIPS timing generator. See Section 3.3.1. Appendix C contains a detailed standard operating procedure for properly running the ramp function.
N	MIPS Digital Input/Output (DIO) controls	These buttons manually enable the digital input/output triggers on MIPS-1 and MIPS-2. When enabled, each trigger outputs a continuous +5V DC signal for external triggering applications. Each MIPS has two digital outputs and has a digital trigger input. The digital input and output enable MIPS-2 to send a signal to MIPS-1 to run a different set of events. The DIO's can also be controlled through the timing generator as a definable event. This is discussed in more detail in Section 3.3.1.
O	MIPS-1/MIPS-2 Timing Generator (TG) Controls	The timing generator Edit button opens a separate window where timing generator events can be edited. Trigger starts the timing generator and switches the MIPS to table mode. Abort kills the timing generator and resets the MIPS to standard operating mode. See Section 3.3.1 for detailed explanation of MIPS timing generators.
P	Master MIPS Control Functions	These buttons are the master control buttons for the MIPS. System Shutdown places both MIPS in standby mode and all voltages are set to zero. Save Method saves the values and timing generator events that are active on the control panel as a .settings file. Load Method opens a .settings file. MIPS comms and Scripting are buttons not used in general option. These functions are only accessed during advanced troubleshooting sessions with GAA Custom Engineering.

3.3.1 MIPS Timing Generator and Event Editor

One of the most useful features of the MIPS systems, and the reason why it is referred to as an "intelligent power source" is the programmable timing generator. A small processor installed in each MIPS unit runs a dedicated timing generator where individual events are defined and linked. Shown below in Figure 3-6 is an example of the timing generator editor interface window running within the MIPS application. The timing generator editor allows the user to add, modify or delete events by clicking the drop-down menu at the top of the window. After adding a new event, the parameter/group of parameters that will be used is defined, as well as the time when the event starts, how long it will run, and what will happen when it ends.

All this information is read by the MIPS in the form of a text-based table. For most experiments, the first event is the master trigger signal. This event uses the Trigger Source set to Software, and pressing Trigger on the MIPS control panel starts the experiment.

In the example given below in Figure 3-6, the timing generator in MIPS-1 is running an experiment to change the voltage on one of the electrodes to trap ions inside the mobility region that have been pulsed into the mobility region from the entrance ion funnel before releasing them to the detector. When the Trigger button is pressed on the control panel, MIPS-2 sends a +5V trigger output signal to MIPS-1, where the trigger source is set to accept a positive trigger pulse (Pos), initiating an event called Trap. The total time for all the events to occur within one trigger pulse is defined in the frame parameters section. For the Trap event shown in Figure 3-6, electrode 22 (CH-22) is held from 0 to 200 ms (Start) at +80V (Value,off), before switching the voltage to +10V (Value) for 20 ms (Width). After 20 ms, the voltage returns to the initial +80V for the remaining 270 ms of the frame. Once all the events in a sequence have been defined in the timing generator, the experiment can be saved as a .seq file. Different .seq files can be loaded back into the timing generator editor after being saved and are easily modified when changes to instrumental parameters are required.

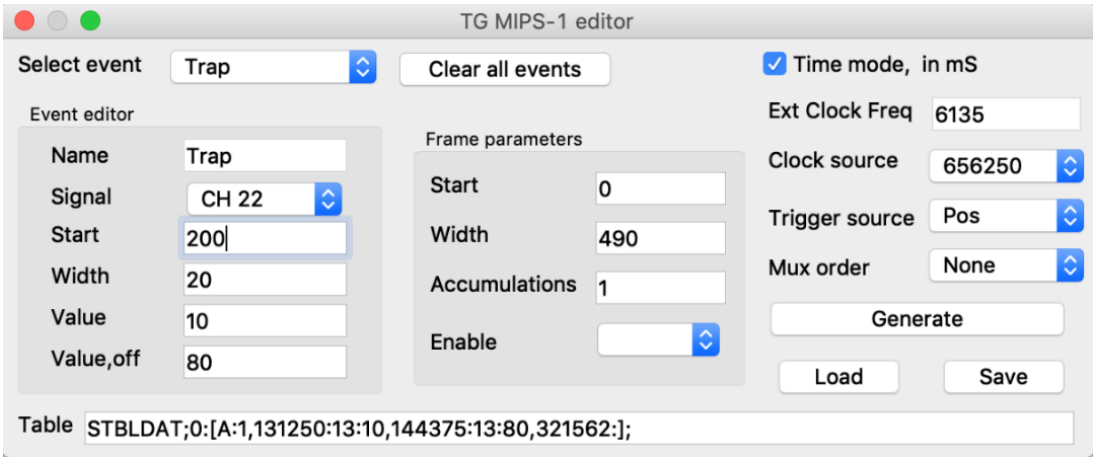

Figure 3-6. Example of MIPS timing generator event page for a single electrode trap experiment.

Multiple trigger pulses can be set by changing the number of accumulations in the Frame parameters section. For most experiments, MIPS-2 starts the event cascade with the initial master trigger, so the

MIPS-2 timing generator defines the total number of accumulations. The number of accumulations corresponds to the number of trigger pulses sent to MIPS-1. Once the trigger pulse is received, it initiates the events that have been defined in the table, starting with the event with the earliest Start time. There are few limitations to the experiments that can be run using the MIPS timing generators. For example, several events can run simultaneously, multiple DC voltage channels can be grouped/controlled into a single parameter such as the Ramp function (Table 1), or an output trigger pulse (or pulses) can be sent to the oscilloscope to start external data acquisition.

3.3.2 Data Acquisition and Post-Acquisition Processing

High-resolution ion current measurements from the Faraday detector are acquired by a DPO5054 oscilloscope (Tektronix, Ontario, CA) set to record a data point every 20 µs. Two independent channel inputs on the oscilloscope are used to collect data, and two corresponding .txt files are generated for each experiment. The Channel 1 .txt file contains the trigger pulse data and the Channel 2 .txt file contains the ion current data (1V = 1nA). Data acquisition for an experiment begins when the MIPS sends the first trigger pulse to the oscilloscope. Each 1 ms pulse is recorded in Channel 1 as a +5V signal. The duration of the pulse and the total number of pulses (*i.e.,* accumulations) is defined by an event labelled Scope Trigger in the MIPS-2 timing generator. The trigger pulses define the beginning and end of an accumulation (*e.g.*, the start of the event sequence defined in the MIPS for one experiment) so it is critical that this signal is consistent. For the majority of the experiments run on the vfTIMS, the oscilloscope is configured to run in *Trigger* mode using a long record length to collect the data for all accumulations in the same frame (Figure 3-7).

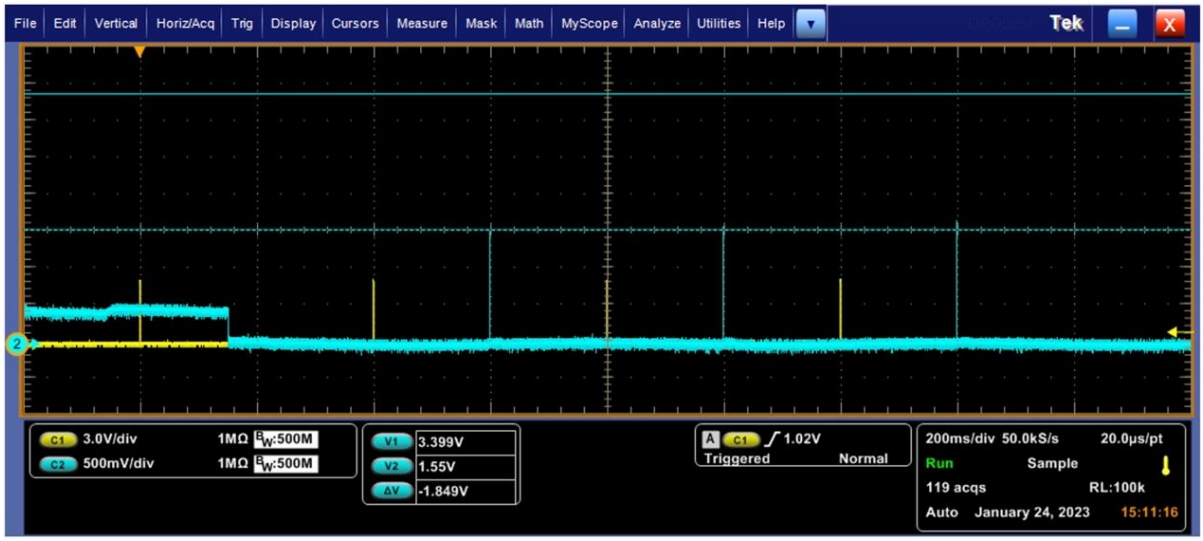

Figure 3-7. Raw data collected from the DPO5054 oscilloscope. Channel 1 (C1, yellow trace) displays the trigger pulses sent from the MIPS. Channel 2 (C2, blue) displays the ion current data for a single electrode trapping experiment.

Once the data has been acquired, it is processed using a Python script (Python v.3.10). Since the oscilloscope collects the ion current completely independently from the trigger pulses in different oscilloscope channels, the Python script must accurately separate the ion current into individual bins that match the duration of time between triggers. The script starts by reading the MIPS trigger signal data in the Channel 1 .txt file and applying a 2nd order polynomial Savitzky-Golay smoothing function. This smoothing is used to average out and minimize the electrical noise in the 1 *ms* wide +5V plateau portion of the trigger, ensuring that the width of each bin is consistent. The center of the first trigger pulse defines the t = 0 ms timepoint for the entire experiment. Once the triggers are processed, the ion current data in the Channel 2 .txt file is read and split into bins that are defined by the indices of the trigger pulses. The time between pulses matches the width frame parameter set in the MIPS timing generator, while the total number of bins matches the number of accumulations. The Python script is set to discard the first bin, as the MIPS is configured to use the first accumulation to equilibrate the power supplies and ensure all the voltages defined by the events in the MIPS timing generators are set to the correct potentials. After binning the ion current data, a low-pass fast Fourier transform (FFT) filter is applied to the ion current to remove high frequency noise. The default setting for the FFT filter is set to pass the 100 lowest frequencies. Following data filtering,

a peak detection algorithm identifies the peaks in each bin. The peak height is calculated, and every peak is integrated numerically to determine the peak area. The average peak height and peak area from all the accumulations (excluding the first) is then calculated. Once the data processing is complete, the averaged ion current spectrum as well as the full multi-accumulation spectrum are outputted as .png and .csv files (Figure 3-8).

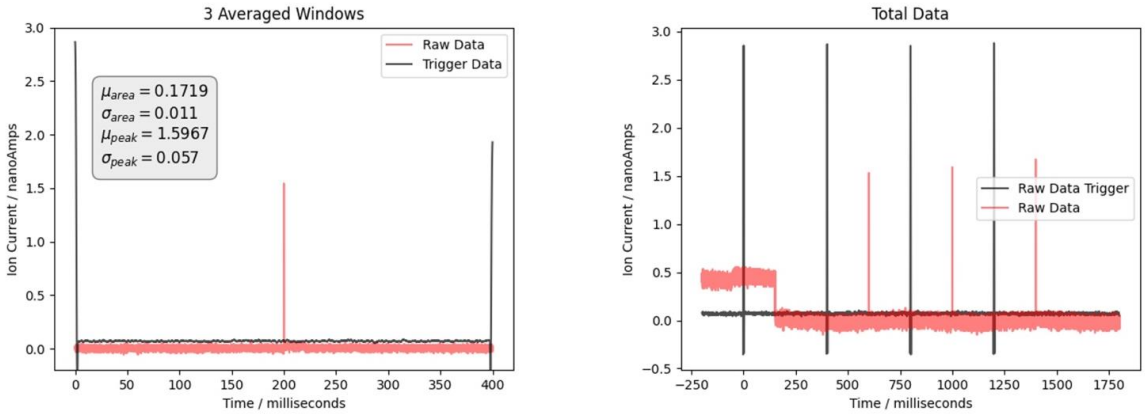

Figure 3-8. Example of ion current data following data processing using the 25 µM TAA8 working solution as a representative example. The pink trace is the total ion current, and the black trace is the trigger signal. **(Left)** The average ion current from three accumulations (first accumulation removed) for a single electrode trapping experiment. **(Right)** The full ion current measurements collected throughout the full duration of the experiment (four accumulations).

3.4 Conclusions

The main objective for this phase of the project was to integrate the power supplies with the vfTIMS and test the electronics to ensure they were working correctly and identify any technical issues that may affect instrument performance. Besides this, an *in-silico* model was built to characterize the hexapolar RF fields generated within the four sectors of the mobility region. This model gave considerable insight into the level of ion confinement needed to ensure optimal performance of the prototype instrument. Furthermore, the user interface was designed to control both MIPS devices, and the MIPS timing generators were configured so comprehensive testing and characterization of the vfTIMS could begin. Lastly, a python script was developed to batch process raw data files that were acquired using the oscilloscope. This script was used to normalize the data, apply a FFT to reduce noise, detect and integrate the peaks, and calculate averaged peak

heights and peak areas for each experiment. Although one technical issue was observed with a minor phase shift between the output signal of the two RF amplifiers, the overall research objective was achieved.

Chapter 4: Prototype Instrument Characterization

4.1 Preamble

This chapter has not yet been published. Most of the data presented in Chapter 4 will be reported in a manuscript in preparation for submission to the Review of Scientific Instruments journal in 2024. All experiments were performed by Daniel Rickert. Data processing and preparation of all figures was done by Daniel Rickert. Data analysis and interpretation was done by Daniel Rickert, Gordon Anderson, Scott Hopkins, and Janusz Pawliszyn. Scott Hopkins and Janusz Pawliszyn were responsible for conceptualization of the project, project supervision, and funding acquisition.

4.2 Introduction

Once the prototype vfTIMS was built and the electronics were configured, the next phase of the project focused on running experiments in the laboratory. Before experiments began, the system was carefully inspected. The mechanical components and hardware installed inside the vacuum chamber were examined to ensure all the components were secured and properly aligned. The power supplies and other electronics were also tested after installation to ensure that appropriate electrical contact was being made between all the wiring connecting the power supplies to the feedthroughs, and the wiring from the feedthroughs to the electrical boards on the instrument. Testing was also done to ensure that all the electronics were properly grounded, there was no visual evidence of short circuits, as well as offline verification to confirm the power supplies were outputting the correct voltage defined by a specified MIPS channel to the correct electrodes on the instrument. Following the extensive quality control testing on the hardware and electronics, the time had come to “fly” ions and begin experimentally characterizing the vfTIMS.

Despite the widespread use of IMS instruments and a considerable amount of literature on different custom-built systems, there is minimal technical information available describing how the instruments were initially tested and optimized to achieve complete operability. Many of the published reports solely describe the different mechanical hardware and electrical components of the instrument in the Experimental Section,

with little emphasis in the Results/Discussion Section detailing the experimental process of developing the instrument. In the case of published literature reporting the development of new commercial IMS instruments, most of the technical information is not publicly shared due to intellectual property concerns. On the other hand, most academic research groups that build prototype instruments have a large amount of in-house experience and "tribal knowledge" that is rarely shared outside of the research group.[99] Thus, much of the initial testing and optimization of the vfTIMS was done via trial and error to determine suitable operating conditions. Since the vfTIMS was the first prototype built at the University of Waterloo, there were few (if any) experimental "starting points" that would apply to this instrument based on literature reports describing similar systems.

The main objective of Chapter 4 was to systematically investigate and identify the optimal set of instrumental parameters for the vfTIMS that would eventually be employed during IMS experiments. To achieve this objective, experimental testing was split into three phases: Phase One – Acquire consistent ion current through the instrument, then determine optimal hardware parameters and instrumental conditions for maximum ion transmission to the Faraday detector; Phase Two – Implement a multi-event MIPS method and optimize instrumental conditions for trapping/releasing ions in one sector of the mobility region; Phase Three – Develop a more robust workflow for trapping ions in one sector of the mobility region before eluting the ions into a second downstream sector where the ions are trapped again prior to the final release to the detector.

In Phase One of experimental testing, the main objective was to determine the ideal settings to maximize ion transmission through the various components of the instrument to the detector. These experiments included optimizing the nanoESI source settings, the DC voltages that define the EFG profile through the instrument, and the RF field applied inside the mobility region. Additionally, since the underlying TIMS functionality relies on pulsing ions into the mobility region, the feasibility of utilizing the aperture at the end of the entrance funnel (*i.e.*, conductance limit) to control the flow of ions into the mobility region was also evaluated. Building on the results from Phase One, the goal of Phase Two was to optimize the

instrumental conditions for trapping ions in individual sectors of the vfTIMS mobility region. The conditions that were tested included the N_2 bath gas flow rate, the pressure differential through the chamber, as well as the RF frequency and peak to peak amplitude. Furthermore, the ion injection pulse time from the entrance funnel conductance limit, and the duration of ion trapping in the mobility region were evaluated. Lastly, the objective of Phase Three was centered around developing an instrumental method where ions would accumulate in one sector of the mobility region for a user-defined period, before being eluted and trapped in a subsequent sector prior to detection. Ultimately, all three phases of the instrumental development were critical for determining the baseline set of conditions that would permit more advanced experiments to be run on the vfTIMS.

For the majority of the experiments described in Chapter 4, several tetraalkylammonium (TAA) compounds were selected as model analytes. These compounds have been widely reported in literature as suitable calibrant molecules for IMS instrument development due to their high ionization efficiency and stability (*i.e.*, permanent positive charge from the quaternary amine), uniform *m/z* increase as the alkyl chains are extended, and well characterized mobilities and CCSs.[43,99,108–111] Agilent TuneMix was also utilized for some of the preliminary experiments due to the wide *m/z* range of analytes in the mixture, which provided valuable insight into the optimal ionization conditions and transmission efficiency of analytes at the atmosphere/vacuum interface of the instrument.[112]

4.3 General Experimental Overview

4.3.1 Sample Preparation

Three TAA salts were used for most of the prototype characterization experiments and were purchased directly from Millipore Sigma (Missouri, USA): tetrapentyl ammonium (TAA5) bromide (CAS: 866-97-7), tetraoctyl ammonium (TAA8) bromide (CAS: 14866-33-2), tetradodecyl ammonium (TAA12) bromide (CAS: 14866-34-3). The TAA analytes were prepared as individual stock solutions in MS grade MeOH purchased from Millipore Sigma (Missouri, USA) and were stored at –80°C. Working solutions for

individual TAA analytes were prepared at a final concentration of 25 µM in MS grade MeOH and were stored at +4°C. A working solution for the TAA mixture (TAA5, TAA8, and TAA12) was prepared with a final concentration of 10 µM for each analyte in MS grade MeOH and stored at 4°C.

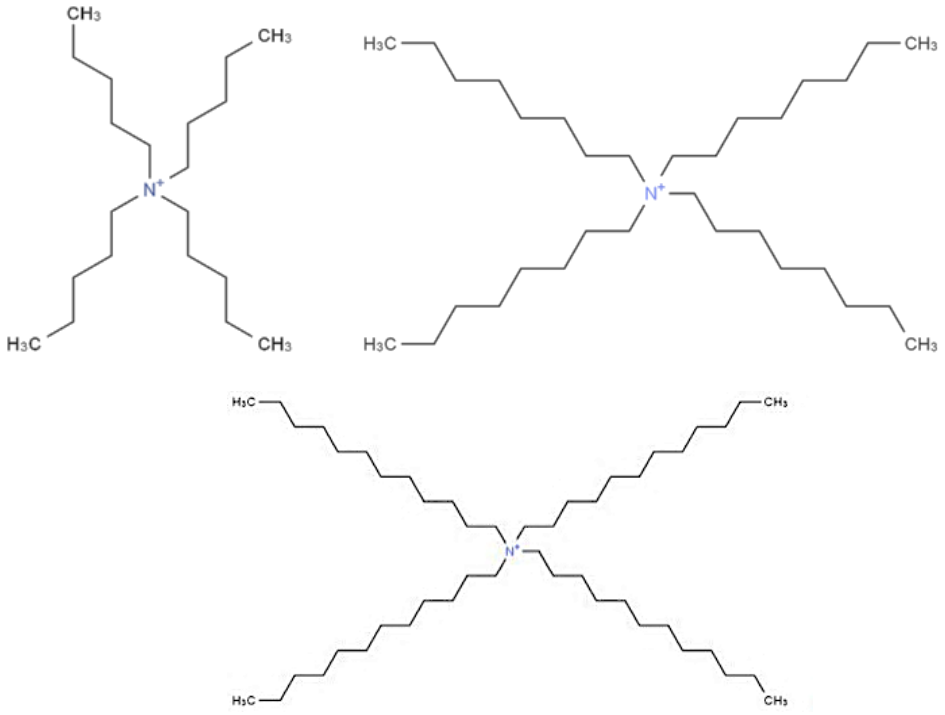

Figure 4-1. (Top **Left)** Chemical structure for TAA5; *m/z* 298.6 and drift tube CCS = 190.1 Å^2.[111] **(Top Right)** Chemical structure of TAA8; *m/z* 466.6 and drift tube CCS = 256.6 Å^2.[111] **(Bottom)** Chemical structure of TAA12; *m/z* 691.3 and drift tube CCS = 319.0 Å^2.[111]

Agilent TuneMix (Product No: G2421 – 60001; California, USA) was used for preliminary experiments that optimized the experimental conditions required to produce a stable ion current from the nanoESI source. The TuneMix consisted of a mixture of calibrants including: betaine (CAS: 107-43-7), trifluoroacetic acid ammonium salt (CAS: 3336-58-1) hexamethoxyphosphazene (CAS: 957-13-1), hexakis (2,2-difluoroethoxy) phosphazene (CAS: 186817-57-2), hexakis (1H,1H,3H-tetrafluoropropoxy) phosphazene (CAS: 58943-98-9), hexakis (1H,1H,5H-octafluoropentoxy) phosphazene (CAS: 16059-16-8), hexakis (1H,1H,7H-dodecafluoroheptoxy) phosphazene (CAS: 3830-74-8), hexakis (1H,1H,9H-perfluorononyloxy) phosphazene (CAS: 186043-67-4), and tris-heptafluoropropyl-S-triazine (CAS: 915-76-4). The mixture of calibrants was diluted in a 95:5 (v/v) mixture of HPLC grade acetonitrile and water.

Per the Agilent product information sheet, the solution was stored at 4°C and no additional modifications were made.

Morphine (CAS: 57-27-2) analytical standard was purchased from Millipore Sigma (Missouri, USA) and used during one of the proof-of-concept experiments in Chapter 5. The stock morphine standard was stored at –80°C. A 25 μM working solution was prepared in MS grade MeOH with 0.1% formic acid (v/v) that was purchased from Millipore Sigma (Missouri, USA) and stored at 4°C.

4.3.2 nanoESI Ion Source Conditions

The various analyte solutions were delivered to the glass nanoESI capillary via a Fusion 100 syringe pump (Chemyx; Texas, USA) at a flow rate of 0.5 – 2 μL/min. QuartzTip nanoESI emitters (New Objective; Massachusetts, USA) with dimensions of 1.0 mm O.D., 0.58 mm I.D., and a tip size of 2 ±1 μm were used for all experiments. An in-house ionization source was used to accurately position the nanoESI emitter in front of the transfer capillary.[94,95] To generate the electrospray, a DC potential of +2.0kV was applied by an alligator clip connected to either the conductive coating on the outer surface of the glass nanoESI emitter or the metal union that joins the emitter to the PEEK tubing from the syringe. The ion transfer capillary was heated to 160°C. For complete hardware details, refer to Chapter 2.

4.3.3 Ion Current Measurements

The ion current was measured two different ways depending on the experiment. The ion current from the earliest experiments optimizing the ion spray conditions from the nanoESI source was measured using custom-built breakout modules that were connected to the transimpedance amplifier. The output from the amplifier was then monitored by the MIPS or a digital multimeter. The breakout boxes housed either a 37 pin D-sub breakout board (CZH-LABS: Electronics-Salon; Shenzen, CHN) that was wired to all the DC channels in the mobility region of the vfTIMS, or a 15 pin D-sub breakout board (CZH-LABS: Electronics-Salon; Shenzen, CHN) that was wired to all the DC channels on the entrance ion funnel and ion transfer capillary. The advantage of the breakout modules for preliminary instrument optimization experiments was

that the ion current could be easily measured at specific points through the instrument without requiring the ions to transit through the entire system to reach the detector. For all the experiments in Chapter 4 following the nanoESI optimization, the ion current was directly measured by the Faraday plate detector connected to the transimpedance amplifier. The output from the amplifier was then split with a BNC tee so the current would be recorded by the MIPS and the Tektronix oscilloscope.

4.4 Results and Discussion: Phase One

4.4.1 nanoESI Optimization – Achieving Stable Ion Spray

The nanoESI source generates ions by applying a large DC potential (*ca.,* 2.0 kV) to the tip of a platinum coated glass capillary while analyte solution is slowly pumped through the capillary using a standard syringe pump.[95] To optimize the stability of the ion spray from the tip of the capillary, several conditions related to the nanoESI source were evaluated using the Agilent TuneMix solution. The multimeter was connected to the 15-pin DC breakout module, and the total current from ions transiting through the transfer capillary and discharging inside the entrance funnel was measured by connecting both the Funnel In (F1In) and Funnel Out (F1Out) channels to the breakout module output. To block ions from passing through the entrance funnel and ensure the full ion current from all ions entering the funnel was measured, the dipolar RF field in the entrance funnel was set to 0 Vpp, and the conductance limit electrode at the end of the funnel was biased to +60V. The aim of these experiments was to solely identify the best nanoESI settings, so measuring the current in the funnel was the logical choice since no other optimizations to the instrument settings were required.

As expected, the total ion current was directly correlated to the voltage that was applied to the nanoESI capillary (Figure 4-2).[95,113] The ion current increased as higher voltages were applied, before plateauing around a voltage of ~2.5 kV and eventually decreasing. Besides the magnitude of the ion current, the other important factor to characterize was the reproducibility of the spray. Therefore, a trade off had to be made between the absolute ion signal, and the reproducibility (*i.e.,* standard deviation) of the spray.

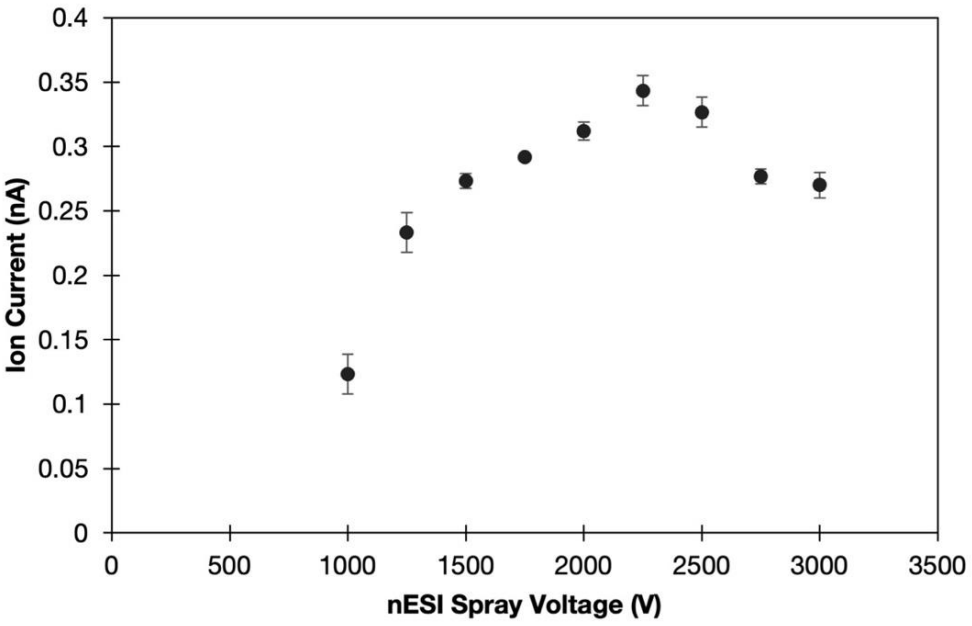

Figure 4-2. nanoESI voltage optimization using Agilent TuneMix. Measurements were taken in triplicate with multimeter connected to F1In and F1Out Breakout. nanoESI sprayer was placed 3 mm back from the transfer capillary inlet.

Once the voltage had been optimized, the position of the nanoESI sprayer relative to the inlet of the transfer capillary (Figure 4-3) was optimized. The tip of the nanoESI capillary was placed directly in line with the inlet of the transfer capillary, unlike other conventional ESI assemblies that position the ESI capillary at a 45° to 90° off-axis angle from the entrance inlet to reduce the likelihood of neutral solvent molecules entering the vacuum chamber. This was a non-factor on the vfTIMS since a small nanoESI capillary tip size (2 ± 1 μm) would inherently reduce the number of neutral solvent molecules entering the instrument, and combined with the heated transfer capillary, the ions were assumed to be sufficiently desolvated.[96] As shown in Figure 4-3, as the sprayer was moved closer to the inlet of the transfer capillary, the ion current exhibited a corresponding increase. However, when the nanoESI emitter was placed closer than 2 mm, arcing occurred between the emitter and the transfer capillary which disrupted the electrospray process. These experiments demonstrated that the main source of instability in the ion current was the high voltage applied to the nanoESI capillary, and that the distance from the transfer capillary had minimal impact.

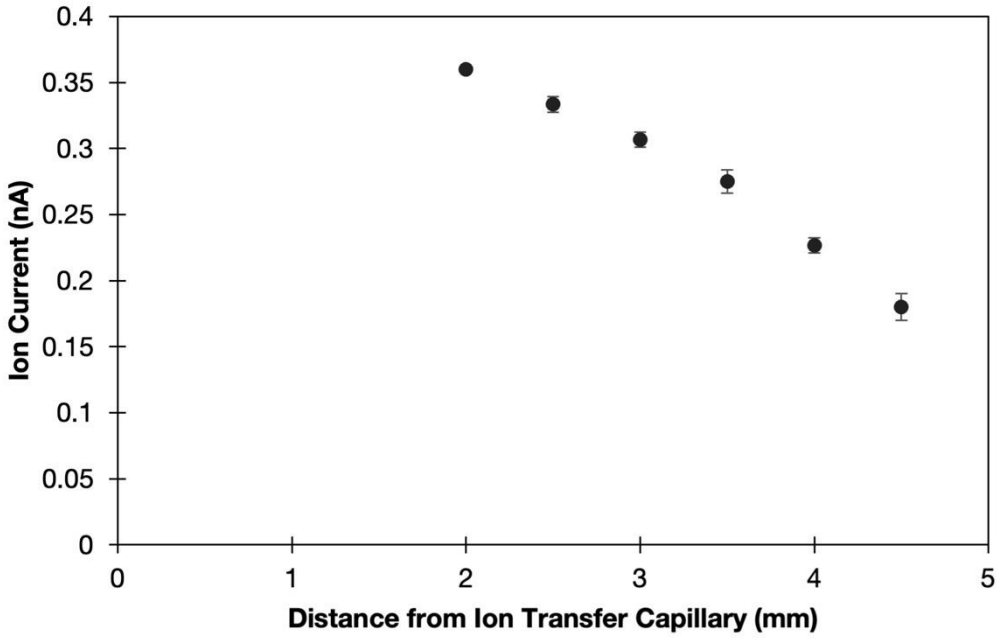

Figure 4-3. nanoESI sprayer distance optimization using Agilent TuneMix at +2.0 kV. Measurements were taken in triplicate with multimeter connected to the F1In and F1Out Breakout.

4.4.2 Transmission Mode Optimization

After optimizing the ionization source conditions, the DC EFG applied through the instrument was evaluated to determine the optimal voltages required for maximum transmission of TAA ions to the Faraday detector. These parameters would be used to build a Transmission Mode instrumental method. The 10 µM working solution mix of TAA analytes (TAA5, TAA8, TAA12) was infused through the nanoESI capillary (2 mm from transfer capillary; +2.0 kV spray voltage) and the total ion current was measured by the Faraday detector. Analyte solution was infused for 30 s for each of the ten trials, and an ion current measurement was taken every 1 s. The average and standard deviation of the ion current were then calculated across the 30 data points. The ion transfer capillary was biased to +60V, and the temperature was held at 160° C. The dipolar RF field through the entrance funnel was set to 760 kHz and 100 Vpp (15% drive) while the hexapolar RF field through the mobility region was set to 700 kHz and 250 Vpp. The N_2 gas flow was set at 0.1 SLPM, the pressure in the front half of the chamber was set to 1.65 Torr, and the pressure in the back half of the chamber was throttled to 950 mTorr. Table 2 contains all the DC EFG profiles that were tested.

Table 2. Summary of DC voltages tested for Transmission Mode optimization.

Trial	F1In (V)	F1Out (V)	F1Cl (V)	Ch1 (V)	CH33 (V)	TubeLens (V)
1	55	30	26	25	−5	−10
2	55	25	21	20	−5	−10
3	55	20	16	15	−5	−10
4	55	15	11	10	−5	−10
5	55	15	6	0	−5	−10
6	55	15	5	0	−5	−10
7	55	15	11	5	−10	−15
8	55	15	11	5	−15	−20
9	55	15	11	5	−20	−25
10	55	15	11	5	−25	−30

F1In, F1Out and F1Cl are the three DC channels that set the electric field through the entrance ion funnel. Ch1 is the first electrode in the mobility region (sector 1), and CH33 is the last electrode in the mobility region (Sector 4). The tube lens (TubeLens) spans the pressure divider and transmits ions to the detector.

As shown in Table 2, ten different trials were conducted with varying DC EFG profiles to establish the best conditions for transmission of the three TAA analytes through the instrument to the detector. The MIPS DC gradient fast fill script was used to define the linear EFG across the mobility region based on the inputs from CH1 and CH33. Figure 4-4 contains the results from the Transmission Mode optimization study. Trials 5 – 8 were the most optimal for transmission of the TAA mix while excellent signal stability (*i.e.*, low standard deviation) was observed across all ten trials. These results demonstrated that optimal transmission of several TAA analytes with a *m/z* range of 299 to 691 required a steady decrease in the DC potentials applied in each region of the vfTIMS. A large DC potential difference across the entrance funnel, combined with a much shallower DC potential difference through the mobility region resulted in the best performance (Figure 4-5). For subsequent experiments, the DC potentials from Trial 5 were used to define the Transmission Mode DC EFG profile.

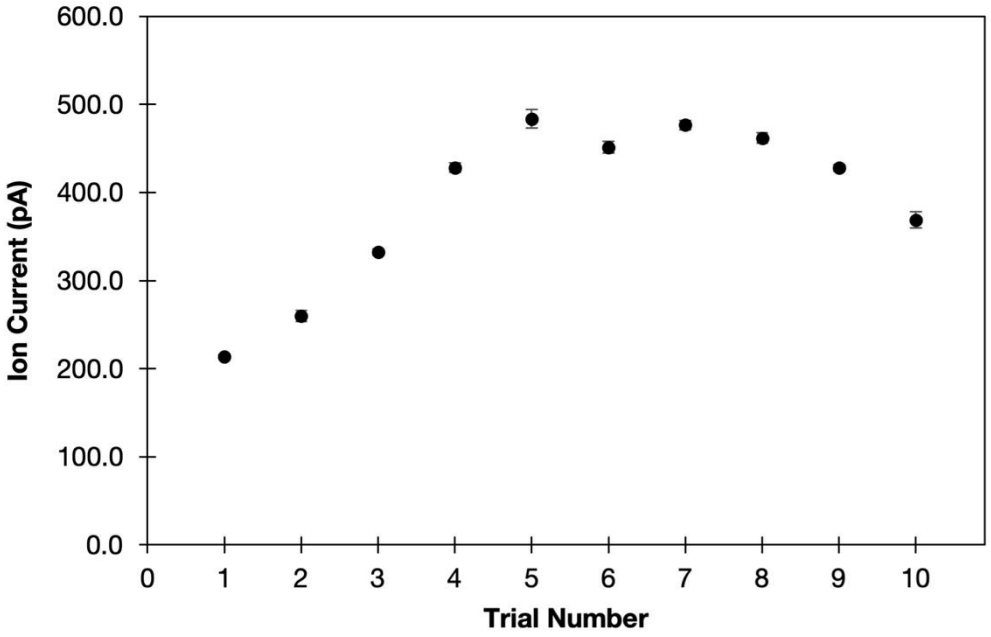

Figure 4-4. Summary of Transmission Mode DC voltage gradient optimization. 10 µM TAA mix was used for all trials. The ion signal was averaged across a 30 s acquisition with a measurement recorded every 1 s. Details on voltages used for each trial are listed in Table 2.

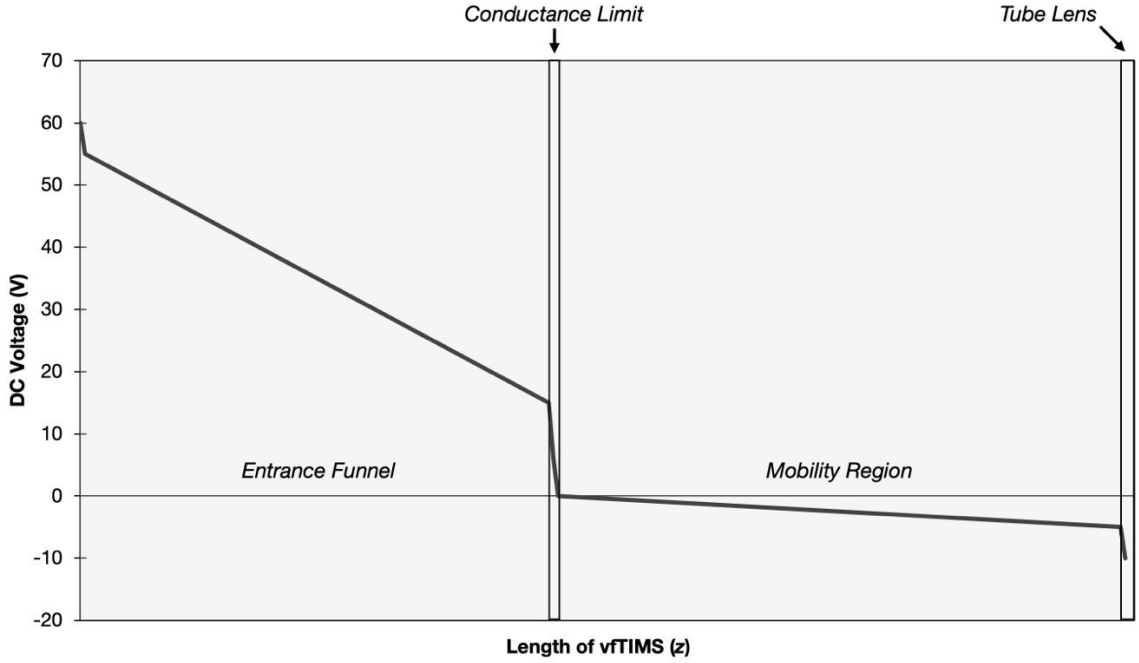

Figure 4-5. Visualization of the Transmission Mode DC EFG profile (Trial 5).

The RF frequency and peak to peak amplitude (*i.e.*, Vpp) that defined the waveform applied to the electrodes in the mobility region to generate the hexapolar confining field were also evaluated to determine the best conditions for ion transmission. Fundamentally, the effectiveness of the radial confinement, and thus the transmission through the mobility region, depend on several factors. These include: (i) the dampening of the ion motion by collisions with neutral gas molecules, (ii) the RF frequency and amplitude, and (iii) space charging effects (*i.e.*, ion-ion coulombic repulsion).[114] Instead of infusing the 10 µM TAA mix, 25 µM individual standards of the three TAA analytes were analyzed. The rationale behind this choice was that since the Faraday detector has no mass selection capability, the most straightforward way to assess the mass dependency of the RF induced pseudopotential for sufficient ion focusing and transmission was to analyze the compounds individually. The DC potentials to generate the EFG profile were set using the values from Trial 5. The effect of the RF frequency on overall ion transmission was investigated from 100 kHz to 900 kHz. During the RF frequency optimization experiment, as the frequency was increased, the RF amplitude was also adjusted to ensure the voltage was kept constant at 250 Vpp. For the RF voltage optimization experiments, the frequency was held constant at 700 kHz, and amplitude was varied from 50 Vpp to 270 Vpp. Analyte solution was continuously infused throughout the experiment, and ion current data was collected for 30 s with a measurement taken every 1 s. The total ion current for each analyte solution was plotted. Prior to data acquisition at each frequency and amplitude test point, the RF power supplies were allowed to stabilize and equilibrate for 30 s to ensure consistent measurements.

For each of the individual TAA solutions that were infused, a similar trend was observed when the RF frequency was varied (Figure 4-6). As the frequency of the hexapolar RF field was increased from 100 kHz to 500 kHz, a sharp rise in the ion current was observed for the three analytes. From 500 kHz to 700 kHz, the signal was consistent, and only at 900 kHz did the ion current for the largest analyte (TAA12) slightly decrease, while the signal for the smallest analyte (TAA5) slightly increased. Unfortunately, due to hardware limitations of the RF power supplies, it was not feasible to apply a frequency >900 kHz while still maintaining a consistent output of 250 Vpp. However, these results matched other reports in literature

that describe the same trend, especially with respect to the smaller TAA5.[97,114,115] Given the results reported in the literature, and our own observations, it is likely that if even smaller TAA analytes were infused, or the frequency was increased beyond 900 kHz, the trend would have been even more pronounced. This approach could be utilized as an effective low or high pass *m/z* filter for the vfTIMS. When a low RF frequency is applied through the mobility region, larger molecules would be effective transmitted through the instrument. Conversely, if a higher RF frequency is applied, small molecules would be easily transmitted through the instrument, while transmission of larger molecules would be significantly diminished.

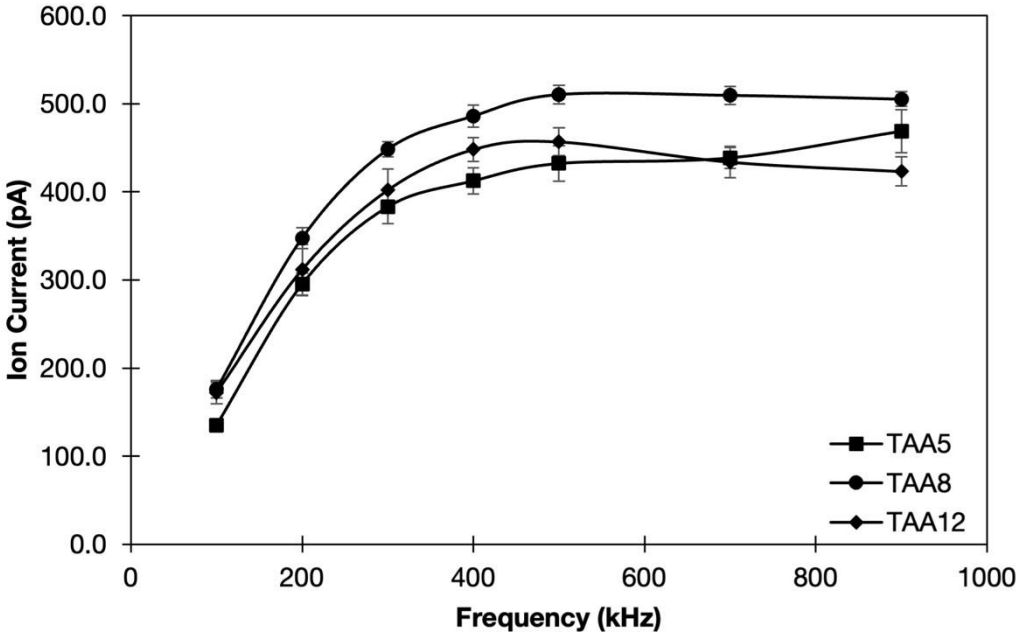

Figure 4-6. Transmission Mode RF frequency optimization. RF amplitude held constant at 250 Vpp for all measurements. Trial 5 EFG profile was applied through the vfTIMS. 25 µM individual TAA analyte solutions were infused. The ion signal was averaged across a 30 s acquisition with a measurement recorded every 1 s.

A similar trend was also observed when the RF amplitude through the mobility region was optimized (Figure 4-7). Theoretically, as the RF amplitude is increased, the magnitude of the hexapolar RF electric field will also increase, consequently improving ion transmission.[41] Experimentally, as the RF amplitude was increased from 50 Vpp to 250 Vpp, a significant rise in the ion current was observed for each TAA species. From 250 Vpp to 270 Vpp (*i.e.,* the maximum output for the RF amplifier), the ion current

plateaued, then began to decrease. This behavior was thought to be primarily due to instability of the TAA ion cloud at high RF amplitudes, an attribute that has also been described in published reports detailing the development of early electrodynamic ion funnels as well as the first articles describing the TIMS analyzer.[22,26,97] In conclusion, the results from the RF optimization experiments verified that the optimal frequency to transmit the three TAA analytes was between 500 kHz to 700 kHz, while the optimal RF amplitude was 250 Vpp.

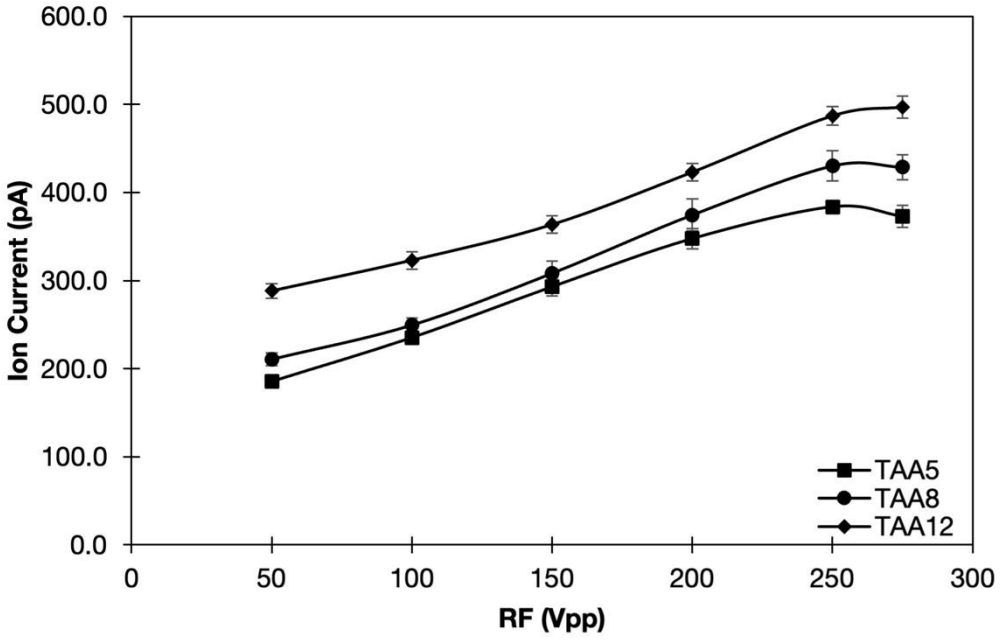

Figure 4-7. Transmission Mode RF voltage optimization. The RF frequency was held constant at 700 kHz for all measurements. Trial 5 EFG profile was applied through the vfTIMS. 25 µM individual TAA analyte solutions were infused. The ion signal was averaged across a 30 s acquisition with a measurement recorded every 1 s.

The final hardware component of the vfTIMS that was optimized during the Transmission Mode development process was the tube lens (Figure 4-8). The tube lens is the cylindrical copper tube that is biased with a DC potential to transmit ions exiting from the last sector of the mobility region to the Faraday detector. Since the detector is mounted to the back side of the pressure divider in the center of the vacuum chamber, the tube lens is essential for transmitting ions through the pressure divider and to the detector. The 10 µM TAA working solution mixture (TAA5, TAA8, TAA12) was infused through the nanoESI

capillary (2 mm from transfer capillary; +2.0 kV spray voltage) and the total ion current was measured by the Faraday detector. The DC potentials to generate the EFG profile were set using the values from Trial 5, the dipolar RF field through the entrance funnel was set to 760 kHz and 100 Vpp (15% drive) while the hexapolar RF field through the mobility region was set to 700 kHz and 250 Vpp. The gas flow and pressure settings were unchanged from previous experiments. The DC potential applied to the tube lens was scanned from –60V to +60V, with 3 V/s measurement increments. The ion current was recorded from three replicate measurements to calculate the average and standard deviation. As shown in Figure 4-8, the optimal voltage to transmit the mixture of TAA ions was between –30V to +10V. When a DC potential above +10V was applied to the tube lens, the ion current rapidly diminished, and above +30V, the measured ion current was negligible. This result demonstrates that as the magnitude of the applied DC voltage is increased, a potential energy barrier is formed. This barrier defocuses the ions, leading to radial ejection and ultimately results in neutralization as the ions collide with the inner walls of the tube lens.[116,117]

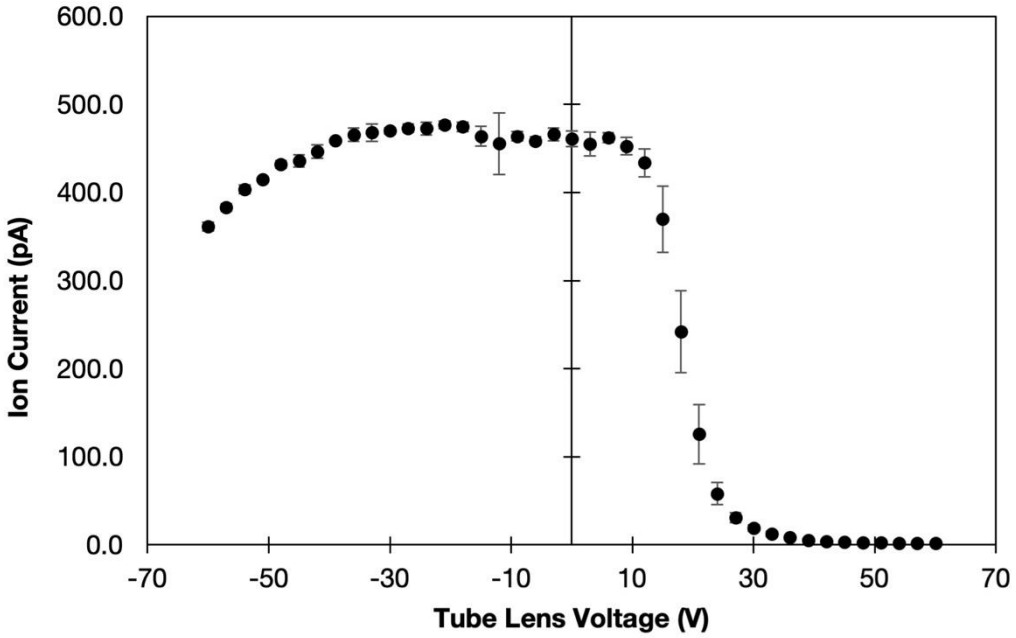

Figure 4-8. Tube lens voltage optimization. 10 µM TAA mixture was infused. The ion current measurements were collected in triplicate to calculate the average and standard deviation.

4.4.3 Modulating Ion Transmission using the Entrance Funnel Conductance Limit

The last experiment in Phase One of vfTIMS instrument testing centered on understanding how the flow of ions through the entrance funnel into mobility region could be precisely controlled. A key component of the conventional TIMS instrument is the electrostatic deflector that applies a repulsive DC potential to a metal plate in the source region to pulse ions into the entrance funnel as they exit the transfer capillary.[27] Since the vfTIMS does not utilize a deflector plate and the nanoESI source was continuously producing ions when the high voltage was applied, a different approach was needed. The terminal lens of the entrance funnel (*i.e.,* conductance limit) can be controlled separately from the rest of the electrodes that comprise the funnel. Thus, an independent potential can be applied to the conductance limit lens to block the flow of ions without disrupting the EFG applied through the rest of the entrance funnel. This approach is analogous to the Bradbury Nielsen or Tyndall ion gates used in most DTIMS instruments to pulse ions into the drift region.[118–120] The main difference is that both the Bradbury Nielsen and Tyndall gates are constructed using thin wire meshes where a potential is applied to create an orthogonal repulsive electric field that prevents ions from passing through.

In the vfTIMS, the entrance funnel conductance limit does not have a mesh grid, so it was necessary to test if the singular application of a DC potential to the conductance limit aperture was sufficient to block the flow of ions into the mobility region (Figure 4-9). To evaluate this hypothesis as an initial proof of concept, 25 µM TAA8 working solution was continuously infused through the nanoESI capillary (2 mm from transfer capillary; +2.0 kV spray voltage) and the total ion current was measured by the Faraday detector. As the solution was infused, the DC potential applied to the conductance limit was scanned from –60V to +60V, with 2 V/s measurement increments. The DC potentials to generate the EFG profile were set using the values from Trial 5, the dipolar RF field through the entrance funnel was set to 760 kHz and 100 Vpp (15% drive) while the hexapolar RF field through the mobility region was set to 700 kHz and 250 Vpp. The gas flow and pressure settings were unchanged from previous experiments.

The total ion current for the TAA8 solution as a function of the conductance limit voltage is shown in Figure 4-9. At a lowest DC potential (*e.g.*, –60V), the ion current at the detector was essentially zero, meaning the conductance limit was effectively functioning as an ion gate. As the potential increased, the ion current also increased until it reached a maximum from +5V to +20V before beginning to decrease. Somewhat unexpectedly, at the largest positive potential (*e.g.*, +60V) applied, the conductance limit could not completely prevent ions from leaking through the aperture to the detector. This was assumed to be caused by a combination of the positive charge on the TAA8 ions and the driving force exerted by the flowing N_2 bath gas. When the large negative DC potential is applied, the ions are attracted to the conductance limit and neutralize upon contact with the lens. Conversely, when the large positive potential is applied, the ions are repelled from the lens, but the flowing bath gas is still able to push a small number of ions through the aperture.[100] Therefore, if the voltage applied to the conductance limit is rapidly pulsed between –60V (*i.e.*, gate closed) and +5V (*i.e.*, gate open), the number of ions entering the mobility region can precisely controlled.

As evidenced by Figure 4-9, the repulsive electric field is not as effective as the attractive electric field for controlling the flow of ions through the entrance funnel conductance limit into the mobility region. Because of this, the entrance funnel as it is currently constructed cannot be used to accumulate in the entrance funnel prior to injection.[103] For applications requiring high sensitivity or a high duty cycle, this is a weakness that not only affects the vfTIMS but also the majority of IMS instruments that operate via ion pulsing.[119] Only a small percentage of ions passing through the conductance limit aperture are analyzed, while the majority of the ions eventually neutralize and are not sampled. A potential avenue for a hardware improvement in a future vfTIMS prototype would be to install a wire mesh to the conductance limit so it could function as a "pseudo" Bradbury Neilson/Tyndall ion gate. The mesh grid would significantly increase the strength of the repulsive electric field at the end of the funnel. This would ensure that ions would be accumulated for a defined period prior to injection into the mobility region without being neutralized.

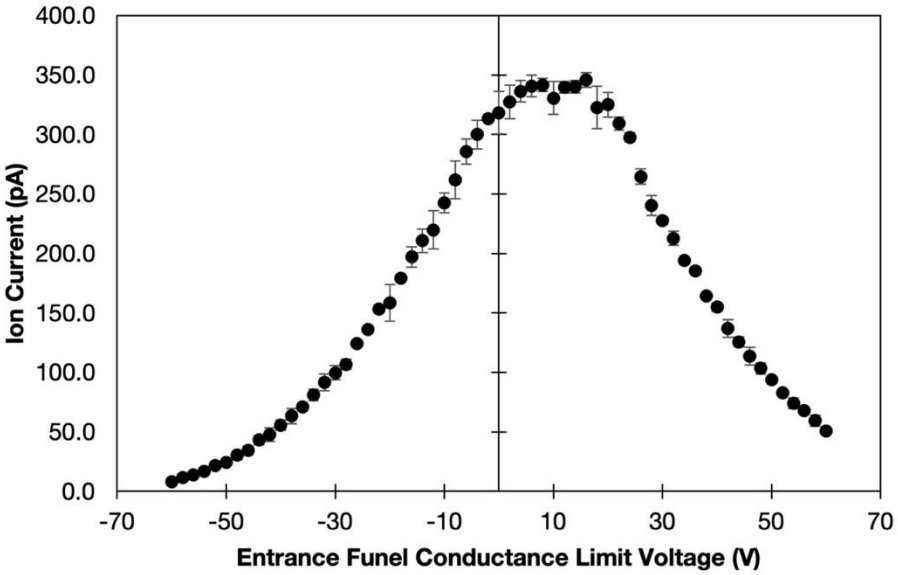

Figure 4-9. Entrance funnel conductance limit optimization. 25 µM TAA8 working solution was infused. The ion current measurements were collected in triplicate to calculate the average and standard deviation.

4.5 Results and Discussion: Phase Two

Throughout Phase One of testing, the settings on the vfTIMS were configured to maximize ion transmission. While these settings were suitable for transmission, they were unlikely to be optimal for trapping ions, a much more sensitive process. Fundamentally, trapping and mobility separation in any TIMS instrument depend on the balance between the force exerted by the flowing bath gas through the analyzer and the opposing force of the electric field. Therefore, careful adjustment of gas flow, pressure, and axial and radial electric fields were essential for creating the ideal conditions for ion trapping. As discussed in the introduction to Chapter 4, the primary objective in Phase Two of vfTIMS development was to establish a second instrumental method, known as the Trap Mode, for trapping ions in different sectors of the mobility region.

4.5.1 Modification to the DC EFG to Facilitate Ion Trapping

The first modification made for the Trap Mode involved introducing a small change to the shape of the axial DC EFG through the mobility region. Early experiments revealed that transitioning from a negative

slope of the EFG (DC potential range of 0V to –5V) to a slightly positive slope with a DC potential range from 0V to +15V significantly improved the ability to trap ions (see Figure 4-10 and Figure 4-11).[27] In the preliminary experiments conducted during Phase Two, the EFG through the mobility region was set to a linear gradient from 0V to +15V across the mobility region, and a single set of electrodes in the middle of a particular sector was used to trap ions. These selected set of electrodes were biased to a large positive DC potential (+80V) which created a repulsive electric field barrier. To induce ion trapping, a short MIPS sequence was developed using the MIPS timing generator. This sequence involved applying the repulsive DC potential in the mobility region for a defined period to trap ions, rapidly switching to a lower potential to release the ions, and then returning to the initial trapping state. This straightforward experimental setup allowed for the optimization of key experimental variables, such as the pressure differential and N_2 gas flow. Notably, during these preliminary experiments, the entrance funnel conductance limit gate was not used, resulting in ions continuously flowing into the mobility region, where they were trapped. While this was not the ideal set-up for the instrument and would limit overall performance, the purpose of these experiments was not to achieve optimal performance. Instead, the aim was to optimize the parameters required for baseline operability before attempting more complex experiments.

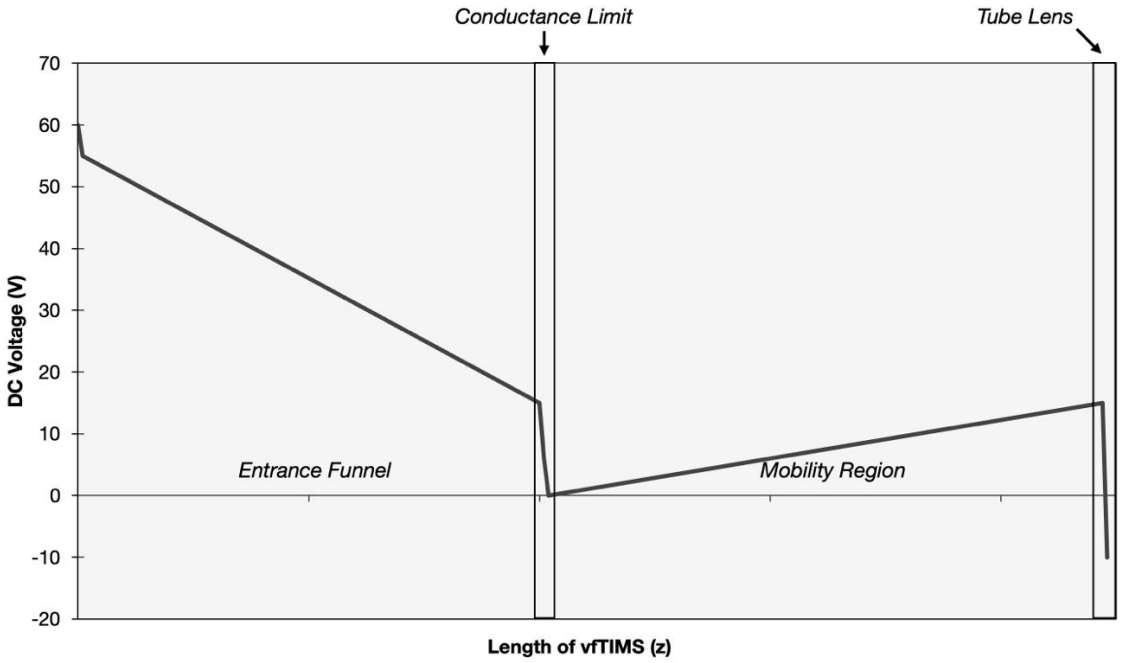

Figure 4-10. Optimized DC EFG for trapping in different sectors of the vfTIMS mobility region.

4.5.2 Preliminary Experiments to Establish Optimal Gas Flow and Pressure Differential

The first parameters optimized during Phase Two of the vfTIMS instrument development process were the N_2 bath gas flow and pressure differential across the divider that separates the source region (front vacuum chamber) and the detection region (rear vacuum chamber). Refer to Figure 2-1 in Chapter 2 for a schematic of the vacuum chamber assembly. To evaluate the effect of these parameters, the 25 µM TAA8 working solution was continuously infused through the nanoESI capillary (2 mm from transfer capillary; +2.0 kV spray voltage) while the total ion current was acquired using the Faraday detector and oscilloscope. The dipolar RF field through the entrance funnel was set to 760 kHz and 100 Vpp (15% drive) and the hexapolar RF field through the mobility region was set to 700 kHz and 250 Vpp.

The MIPS sequence file was configured to start the experiment by sending a trigger signal from MIPS-2 to the oscilloscope to initiate data acquisition. Simultaneously, the DC potential on the set of electrodes in the middle of sector 3 (CH22) was raised at +80V to trap ions for 30 ms, dropped to +9.84V for 2 ms, before reverting to +80V for the remainder of the acquisition window. The total time for each experiment (*i.e.*, accumulation) was 100 ms, and four accumulations (one “equilibration” accumulation, three “true”

accumulations) were collected in a single oscilloscope data file. An example of this experiment is shown in Figure 4-11. The MIPS systems were designed to utilize the first accumulation, known as the "equilibration" accumulation, to verify that all voltages were correctly set on the instrument control panel according to the initial values specified in the MIPS sequence file. Since the experiment begins with the DC potential on CH22 set according to the 0V to +15V EFG, the MIPS must switch the voltage on CH22 to +80V 32 ms after the trigger in the first accumulation to match the potential defined by the MIPS sequence file for the subsequent accumulations. To assess the degree of trapping occurring under different experimental conditions, the magnitude (*i.e.,* height) of the ion current during the first 30 ms of the "equilibration" accumulation was compared to the average magnitude of the subsequent three "true" accumulations. In Figure 4-11 (right panel), “A” denotes the ion current when ions are being transmitted through the analyzer with no trapping during the “equilibration” accumulation, while “B” denotes the ion current during the three “true” accumulations when the trapping potential was applied.

An examination of Figure 4-11 also highlights the benefits of adjusting the DC EFG through the mobility region. In Figure 4-11 (left panel), the DC EFG in the mobility region was set to the optimal Transmission Mode (0V to –5V) settings. Negligible ion trapping occurred under these conditions since the ion current during the initial equilibration accumulation was essentially the same as during each of the three trapping accumulations. This behavior is in contrast with the right panel of Figure 4-11, where the DC EFG through the mobility region was changed to the Trap Mode (0V to +15V) settings and a significant spike in ion current is observed after the potential drop. This sharp spike in ion current is associated with the trapped ions being released from sector 3 of the mobility region towards the detector.

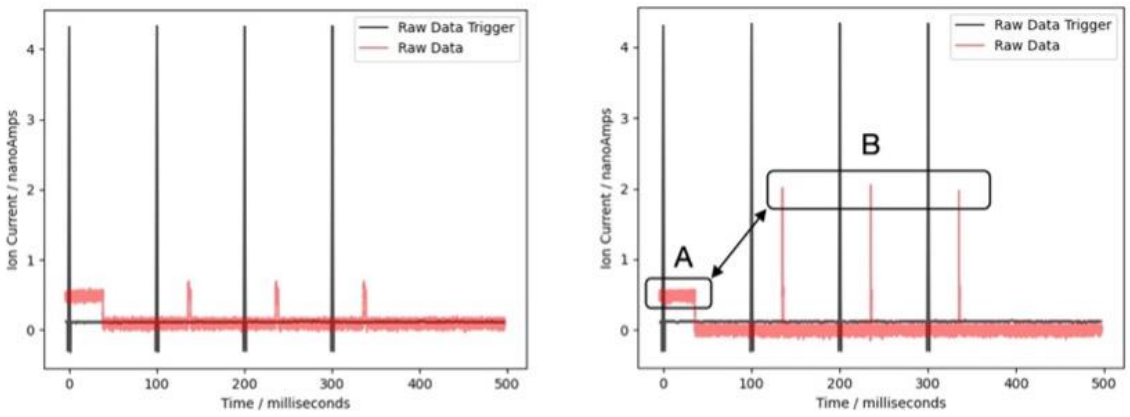

Figure 4-11. Example data for quantifying ion trapping. The black data trace is the smoothed MIPS trigger signals, and the red data trace is the ion current. 25 µM of TAA8 solution was infused. **(Left)** Example of negligible trapping when applying the Transmission Mode EFG through the mobility region. **(Right)** Example of significant trapping when applying the Trap Mode EFG through the mobility region. The **A** region shows the ion current prior to the repulsive potential on CH22 in sector 3 being applied. The **B** region shows the spike in ion current when the repulsive potential is dropped, which released the trapped TAA8 ions. The intensity average of the B region versus the average of the A region is used to calculate the relative ion intensity during the trapping event.

Optimization of the pressure differential within the vacuum chamber revealed that achieving ion trapping required precise pressure and gas flow conditions. To assess the influence of source chamber pressure, a controlled variation was applied, ranging from 1.15 Torr to 1.65 Torr, while the pressure in the detection region remained constant at 950 mTorr. The flow rate of N_2 gas was maintained at a consistent 0.1 SLPM for the duration of the experiment. The pressure differential was calculated as the difference between the source (front chamber) and detection region (rear chamber) pressures. As depicted in Figure 4-12, an evident trend emerged as the pressure differential increased, indicating a significant decrease in ion trapping efficiency. This observation suggests that as the gas velocity increased due to the larger pressure differential, the opposing force of the repulsive electric field became notably less effective in retaining TAA8 ions within sector 3. Furthermore, there was almost a 2-fold improvement in trapping when the source pressure was set to 1.25 Torr compared to when the source pressure was set to 1.7 Torr.

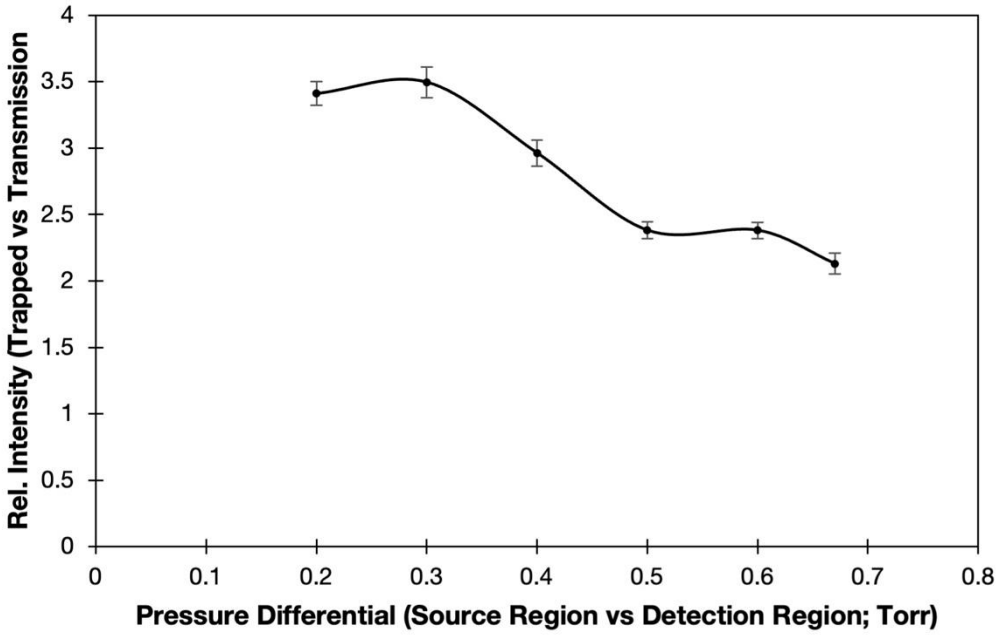

Figure 4-12. Evaluation of varied pressure in source region (front vacuum chamber) on ion trapping. Pressure in detection region (rear section of chamber) locked at 950 mTorr. The average maximum intensity of the three "true" accumulations was compared versus the average intensity of the initial transmission ion current. 25 µM TAA8 working solution was infused and trapped in sector 3 (CH22).

The pressure conditions in the detection region of the vacuum chamber were also evaluated. Due to the interdependency of pressure in the source and detection vacuum chambers, adjustments to the rear vacuum chamber were constrained relative to the previous optimization experiment. Specifically, the pressure in the source vacuum chamber was held constant at 1.25 Torr, while the pressure in the detection region from 1.05 Torr to 870 mTorr. This led to a pressure differential range between 0.25 and 0.38 Torr, as illustrated in Figure 4-13. Notably, when the pressure in the detection region was varied, minimal changes in the extent of ion trapping for TAA8 ions were observed. This outcome reinforces the notion that the primary driver of trapping is the pressure in the source region vacuum chamber, a logical deduction since both the entrance funnel and mobility region are in the front vacuum chamber (as depicted in Figure 2-1).

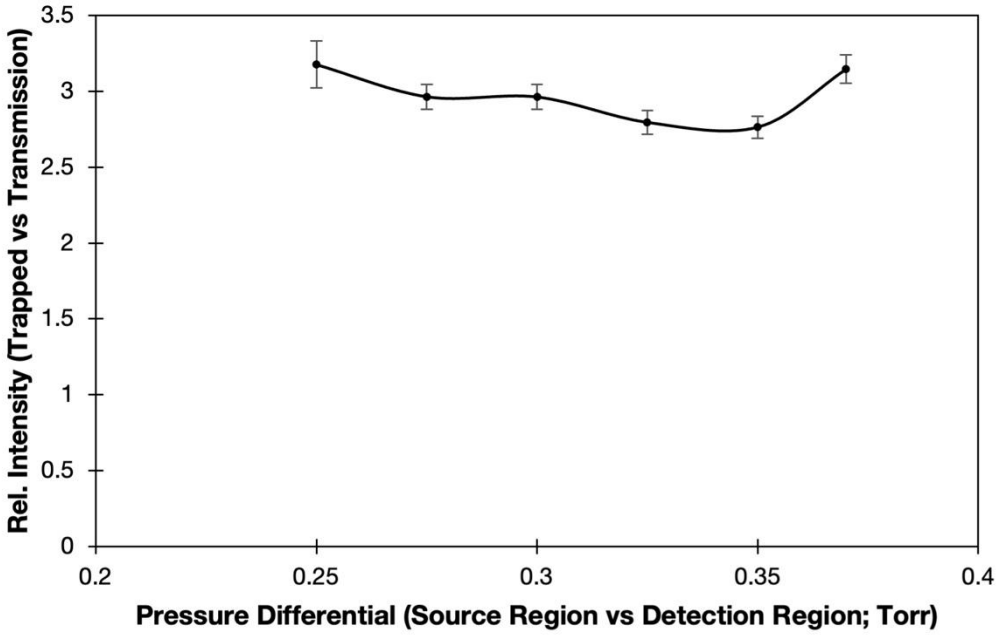

Figure 4-13. Evaluation of varied pressure in detection region (rear vacuum chamber) on ion trapping. Pressure in source region (front section of chamber) locked at 1.25 mTorr. The average maximum intensity of the three "true" accumulations was compared versus the average intensity of the initial transmission ion current. 25 µM TAA8 working solution was infused and trapped in sector 3 (CH22).

Following the establishment of the optimal pressure differential, attention was directed toward optimizing the N_2 bath gas flow (Figure 4-14). The influence of varying the N_2 flow on the trapping of TAA8 was examined within the range of 0.1 SLPM to 0.35 SLPM. It is important to note that 0.1 SLPM marked the lower limit accurately measurable by the flowmeter, while exceeding 0.35 SLPM rendered it unfeasible to maintain the front pressure at 1.25 Torr and the rear pressure at 950 mTorr. A noteworthy pattern emerged when the N_2 flow rate was increased that was somewhat like source region vacuum pressure optimization experiment. With increasing N_2 flow, the extent of ion trapping began to decrease. This decline was attributed to the increased volume of gas streaming through the N_2 gas tubes that are coaxially aligned with the end of the ion transfer capillary inside the vacuum chamber. The increased gas flow likely induced some degree of turbulence, which impacted ion focusing and trapping downstream in the mobility region.

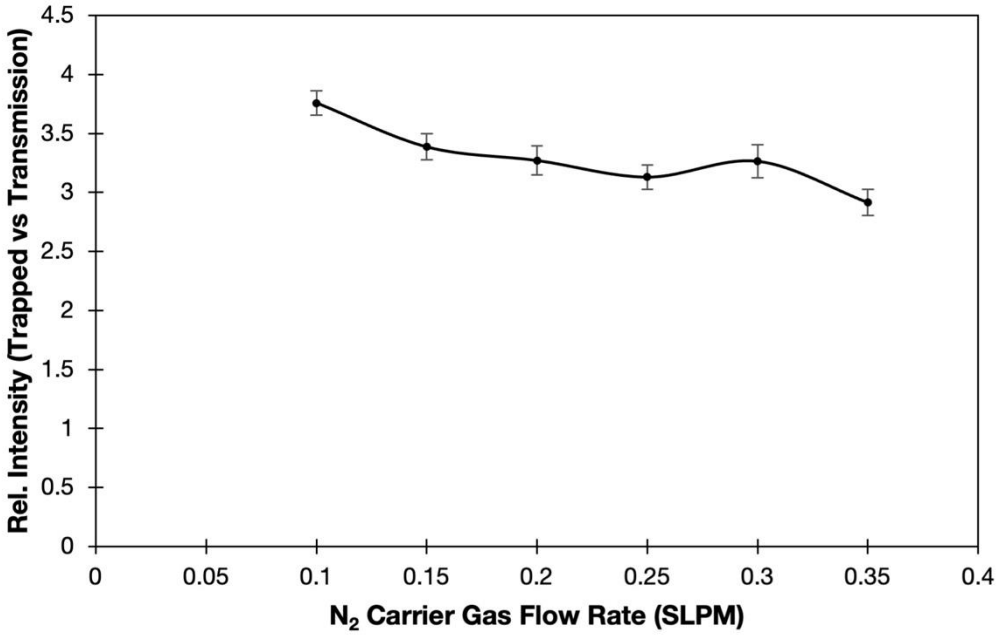

Figure 4-14. Effect of N_2 gas flow on ion trapping. Previously optimized pressure settings used: Source region – 1.25 Torr; Detection region – 950 mTorr. The average maximum intensity of the three "true" accumulations was compared versus the average intensity of the initial transmission ion current. 25 µM TAA8 working solution was infused and trapped in sector 3 (CH22).

4.5.3 Achieving Complete Ion Trapping Functionality

Sections 4.5.1 and 4.5.2 detailed experiments aimed at optimizing key parameters affecting ion trapping within the vfTIMS mobility region. However, it must be acknowledged that these experiments had limitations and did not provide a comprehensive characterization of the instrument's ion trapping capacity. Notably, one significant aspect absent from these experiments was the precise control of the number of ions entering the vfTIMS analyzer through the entrance funnel. Furthermore, these experiments exclusively utilized TAA8 ions, warranting an expansion of the study to encompass a broader range of ions for a more complete evaluation. While limited in scope, these initial experiments were critical for establishing a working baseline set of instrumental parameters that could be utilized during more complex experiments that are described below. To comprehensively assess the vfTIMS's ability to focus and trap ions, a more detailed analysis of the dynamics governing the radially confining RF field during ion trapping was required. There was also a need to explore the entrance funnel's performance in efficiently pulsing ions into

the mobility region, as the initial proof of concept study solely examined its gating functionality. Lastly, for genuine mobility separation experiments in the TIMS, it is critical to retain ions in the analyzer while gradually reducing the electric field strength. Therefore, characterizing the duration for which ions could be held within different sectors of the analyzer was imperative.

To assess the influence of the magnitude and frequency of the radially confining hexapolar RF field on ion trapping, a more elaborate MIPS sequence built off the previous proof of concept MIPS trapping sequence was designed. This enhanced MIPS sequence script, utilizing both MIPS-1 and MIPS-2 in parallel, was configured to trigger a sequential series of events: pulsing ions through the entrance funnel conductance limit, trapping ions within one of the mobility region's sectors, and subsequently releasing the ions to the detector. However, given that the entrance funnel's potentials were supplied through MIPS-2 while the vfTIMS mobility region's potentials were controlled by MIPS-1, synchronization of the timing generators in both MIPS units was required. This was achieved by creating an individual sequence script file on each MIPS that outlined specific events to occur on each power supply, with the trigger signal sent from MIPS-2 to MIPS-1 serving as the link between the systems. The sequence file for MIPS-2 was designed as follows: Commencing with the trigger button on the vfTIMS being clicked (t = 0 ms), MIPS-2 simultaneously sent two trigger signals – one to MIPS-1 and another to the oscilloscope to initiate data acquisition. From 0 to 130 ms, the entrance funnel's conductance limit was maintained at –60V to block the entry of ions into the mobility region. Between 130 ms and 150 ms, the conductance limit potential was raised to +6V, enabling ions to enter the mobility region. Past 150 ms until the end of the accumulation, the conductance limit potential reverted to –60V. The sequence file for MIPS-1 was configured to accept the trigger pulse from MIPS-2 and immediately initiate its own sequence of events. From 0 ms to 200 ms, a repulsive potential (*e.g.,* +80V) was applied to a set of electrodes within the mobility region (e.g., CH22 – sector 3 middle). As the ions were released through the entrance funnel, they were trapped for a predefined duration. Between 200 ms and 220 ms, the repulsive potential was lowered to allow all accumulated ions

within the mobility region to reach the detector. A visual schematic of the time sequence is shown in Figure 4-15.

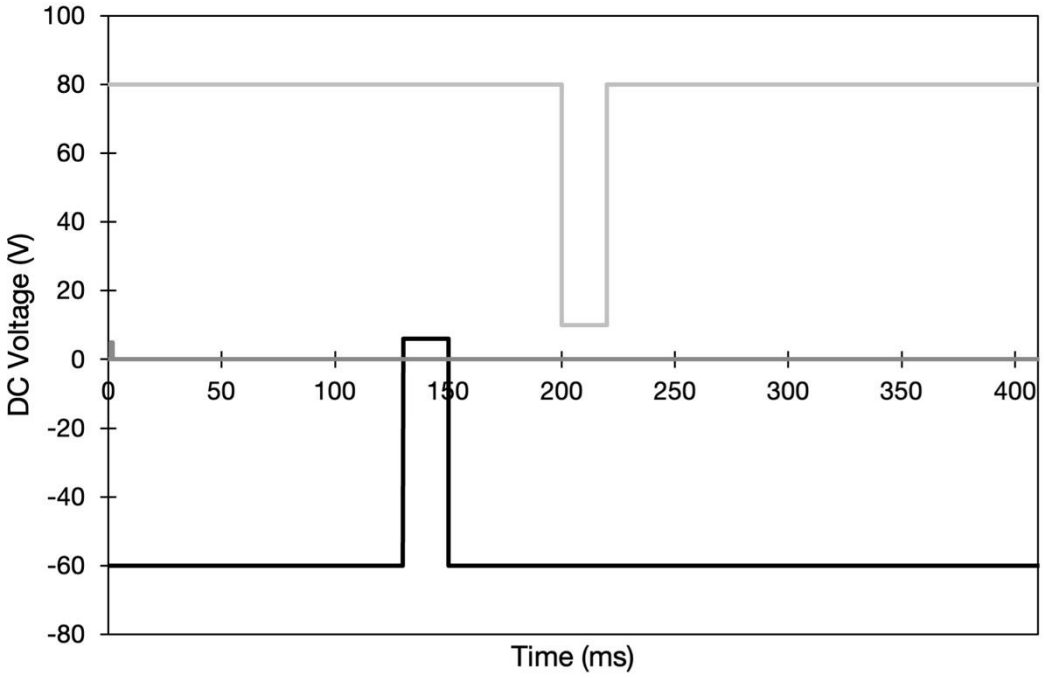

Figure 4-15. MIPS timing sequence for single sector ion trapping with entrance funnel pulsing. Black trace corresponds to the potential on the entrance funnel conductance limit. Light grey trace corresponds to the potential applied to the selected set of electrodes. Dark grey trace on the far left of the plot corresponds to the two triggers signals (MIPS-2 → MIPS-1, MIPS-2 → Oscilloscope).

4.5.3.1 RF Voltage and Frequency Optimization.

Low-pressure IMS systems such as the vfTIMS require RF confinement to minimize ion diffusion and ensure ions are effectively focused within the analyzer.[28] When conducting trapping experiments on the prototype instrument, the presence of the radially confining field is crucial as it prevents ions from diffusing toward the inner walls when they encounter the repulsive DC electric field in the mobility region. During Phase One, the RF frequency and magnitude were specifically tuned for experiments involving the continuous flow of ions through the mobility region. As explained in detail in the Introduction, the number of ions injected into the analyzer directly impacts both radial and axial diffusion. In Phase Two, the objective was to inject a group of ions into the mobility region, trap them for a certain period, and then

release them to the detector. Consequently, the instrumental parameters for the RF field needed to be reevaluated to determine the optimal conditions for ion trapping and focusing.

To evaluate the effect of the RF frequency for trapping ions with different *m/z* values, individual 25 µM working solutions for TAA8 and TAA12 were infused. The improved MIPS script with the conductance limit ion gate was used to control the number of ions injected into the mobility region. Since radial confinement is very sensitive to Coulombic repulsion (*i.e.,* space charging), precise control of the stream of ions into the mobility region is needed to truly evaluate the effects of the RF frequency and peak to peak amplitude.[37] Ions were pulsed into the mobility region with a 20 ms pulse width, trapped for 50 ms in the center of Sector 3, before being released to the detector. The Trap Mode DC EFG, as well as the optimal gas and pressure settings were used for all experiments. For RF frequency optimization, the RF magnitude was maintained at 250 Vpp. During data processing, the initial equilibration accumulation was removed. The subsequent three true accumulations were averaged, and the average and standard deviation of the integrated area of the trapped peak were reported. See Section 3.3.2 for more details.

The effect of RF frequency on trapping was evaluated between 300 kHz to 800 kHz (Figure 4-16). In the case of both TAA8 and TAA12 analytes, a notable decrease in integrated area was observed as the RF frequency increased. Above 800 kHz, negligible trapping occurred. This finding was somewhat unexpected, as a different trend was observed during the Transmission Mode optimization in Phase One. In general, higher frequencies in RF fields tend to favor the transmission of low-mass ions, particularly those below 200 amu.[106] Thus, the decrease in integrated area could be attributed to various independent factors or, potentially, the synergistic effect of several. From a hardware standpoint, the reduction in integrated area (*i.e.,* trapping) could be related to the increasing phase shift between the two RF amplifiers at higher frequencies, resulting in a destabilizing asymmetric radially confining RF field within the mobility region. On the other hand, from an ion dynamics perspective, it could also be linked to a decrease in ion adiabaticity (*i.e.,* stability) as higher frequencies were applied to the RF electrodes in the mobility region, leading to the instability of both TAA ions when they were trapped.[106] At this stage, it is difficult to determine which of

these factors was the reason why this behaviour was observed. Another technical issue arose at lower frequencies (ranging from 300 kHz to 400 kHz), where some significant RF-induced electrical noise was detected by the Faraday detector. As a result, a compromise needed to be reached between the optimal trap conditions and transmission conditions. Consequently, 550 kHz was determined to be the best compromise and was subsequently employed for subsequent experiments.

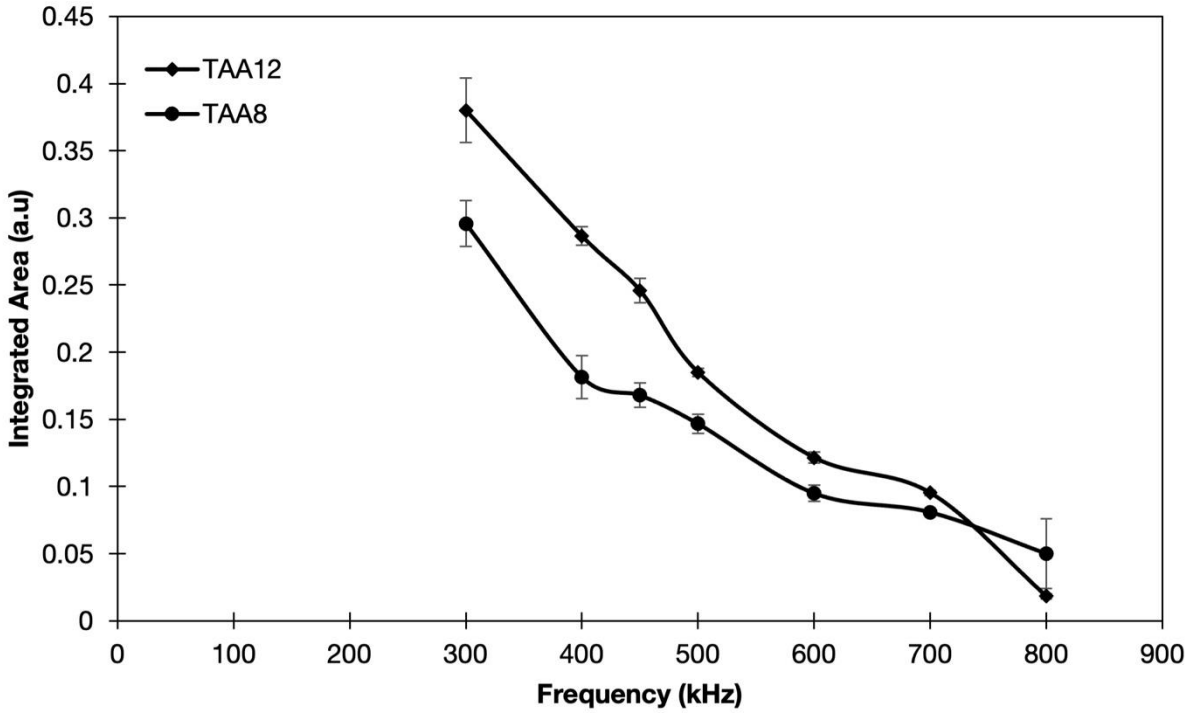

Figure 4-16. Optimization of RF frequency for ion trapping (Sector 3). Constant RF amplitude of 250 Vpp. 25 µM TAA8 and TAA12 working solutions were infused and trapped in sector 3 (CH22). Optimized gas flow conditions and DC EFG used.

After the RF frequency evaluation, optimization of RF amplitude was performed (as shown in Figure 4-17). The frequency was maintained at 550 kHz, and the applied RF voltage was adjusted between 175 Vpp to 250 Vpp. When the applied RF amplitude was less than 175 Vpp, the integrated area fell below the minimum threshold for peak integration that was defined in the Python data processing script (refer to Section 3.3.2). Fundamentally, as the magnitude of the radially confining force increases (by increasing the RF amplitude), the ion cloud is pushed closer to the center of the mobility region, resulting in sufficient trapping and ion focusing.[41] This trend was observed experimentally for both analytes. Interestingly, there

was also a degree of mass dependence on the applied RF amplitude for trapping. At 175 Vpp and 200 Vpp, roughly the same quantity of TAA8 and TAA12 ions were trapped. However, beyond 200 Vpp, the integrated area for the two analytes started to diverge. This divergence was likely related to the axial dispersion induced at high RF field strengths. While the larger TAA12 is adequately confined, the smaller TAA8 begins to diffuse away from the center of the analyzer due to Coulombic repulsion effects, resulting in less ions being trapped and a smaller integrated area.

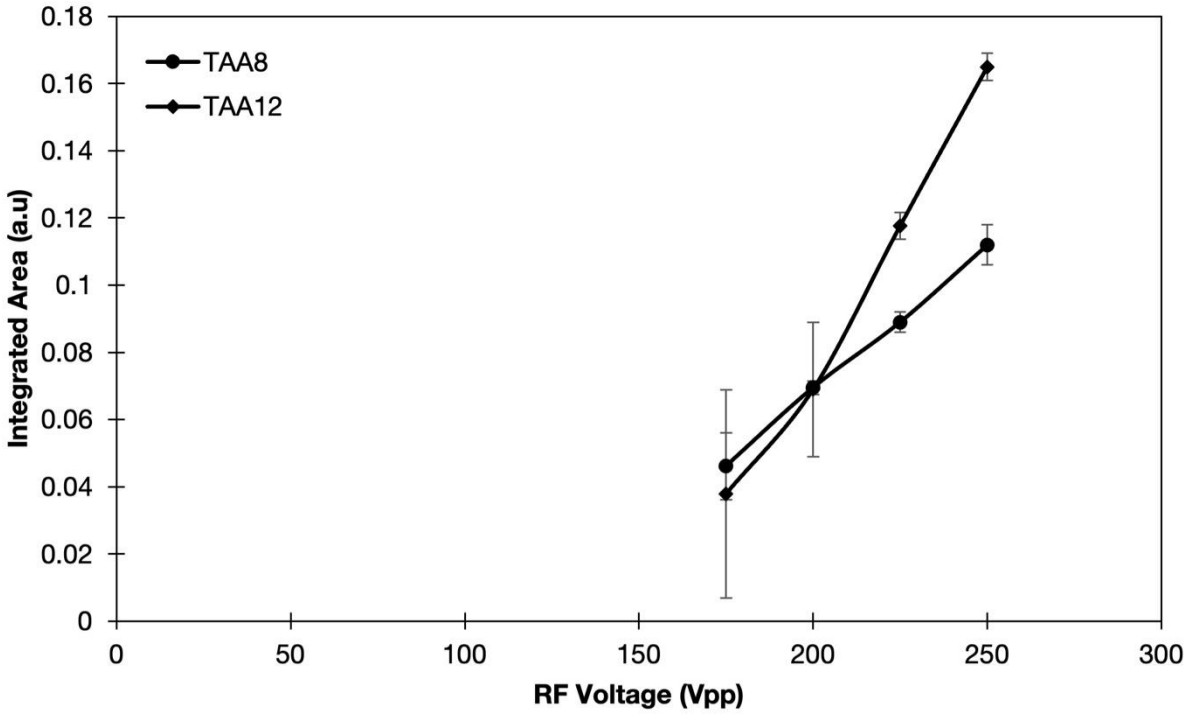

Figure 4-17. Optimization of RF voltage for ion trapping (Sector 3) with locked frequency at 550 kHz. 25 µM TAA8 and TAA12 working solutions were infused and trapped in sector 3 (CH22). Optimized gas flow conditions and DC EFG used.

4.5.3.2 Injection Time Evaluation

Once the RF field parameters had been tuned for optimal ion trapping, the variation of the ion packet size as a function of injection time through the entrance funnel was studied. The injection time was the duration of time when the potential applied to the conductance limit was set to allow ions to enter the mobility region. Individual 25 µM working solutions for TAA8 and TAA12 were infused, the optimized DC EFG and gas flow settings were kept consistent with previous experiments, and the optimal frequency (*i.e.*, 550 kHz),

and amplitude (*i.e.*, 250 Vpp) were applied through the mobility region. For these experiments, the injection time was varied between 0.5 ms and 100 ms, and the trap time in the mobility region was kept constant at 50 ms. Additionally, instead of only studying the effect of the injection time on trapping in the middle of Sector 3 (CH22), trapping in the middle of sector 2 (CH14) was also evaluated.

As the injection time through the entrance funnel conductance limit was initially increased from 0.5 ms to 10 ms, there was a noticeable increase in the number of ions trapped in both sector 2 (see Figure 4-18) and sector 3 (see Figure 4-19). However, the absolute number of ions trapped in these two sectors differed significantly. Initially, sector 2 trapped more TAA8 and TAA12 ions at shorter injection times, but after 20 ms, the integrated area for both analytes began to stabilize. In contrast, sector 3 had fewer ions trapped during short injection times, but with longer injection times, ions continued to accumulate, and the integrated ion current didn't plateau until 100 ms.

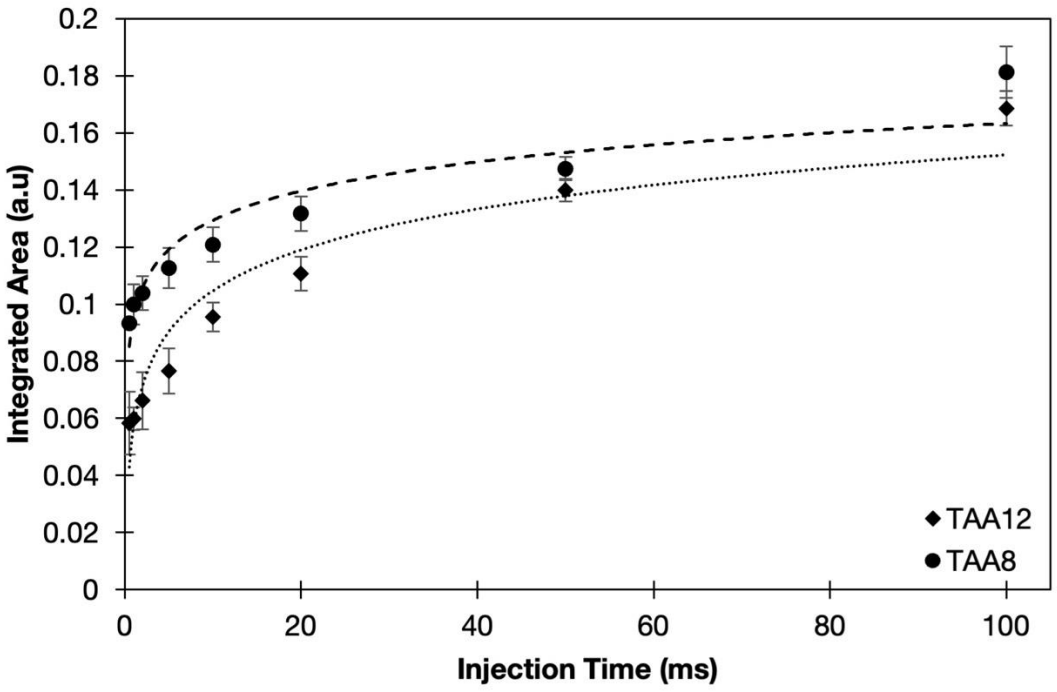

Figure 4-18. Injection time profile for 25 µM TAA8 and TAA12. Ions were trapped in sector 2 (CH14) for 50 ms. The average and standard deviation of the trapped peak area was plotted as a function of injection time from the entrance funnel conductance limit.

To rationalize these results, one must consider what occurs as the ions are released into the mobility region. Sector 2 is closer to the conductance limit at the end of the entrance funnel, meaning ions would travel a shorter axial distance before reaching the trapping zone. Conversely, more ions were lost when they transited further into the mobility region before reaching the trapping zone in sector 3, as indicated by the lower integrated area at short injection times. During longer injection times, a much larger number of ions were released into the mobility region compared to shorter injection times, however, the majority of these ions were clearly not trapped, as indicated by the limited increase in integrated area. This result suggested that sector 2 of the mobility region reached the maximum charge capacity after the 20 ms pulse width, while sector 3 reached the maximum trap capacity after 100 ms.

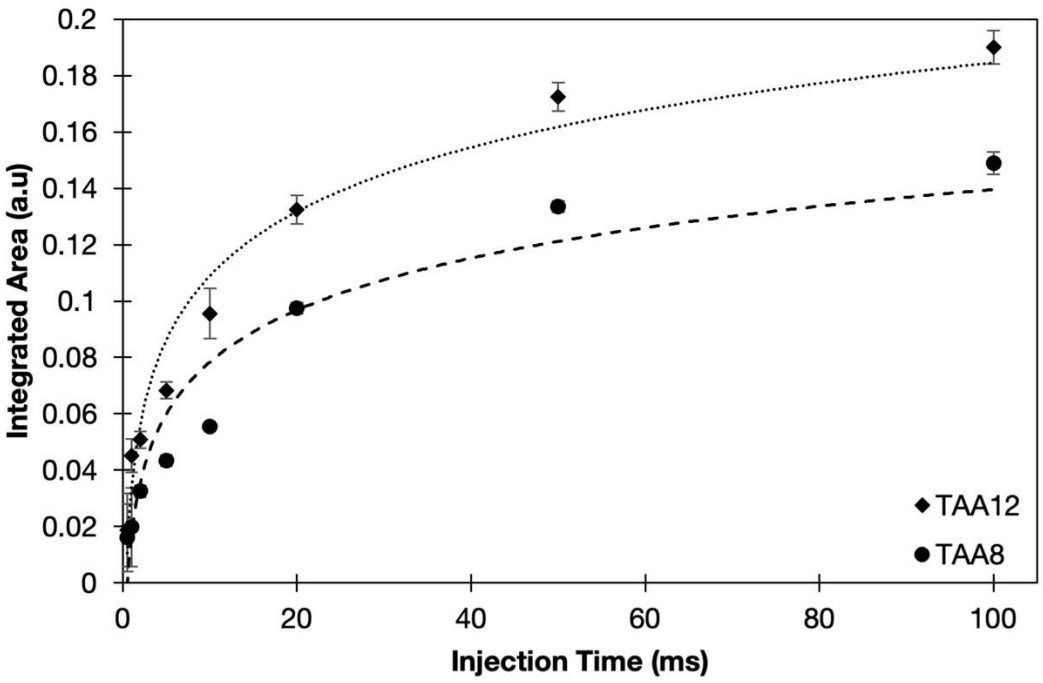

Figure 4-19. Injection time profile for 25 µM TAA8 and TAA12. Ions were trapped in sector 3 (CH22) for 50 ms. The average and standard deviation of the trapped peak area was plotted as a function of injection time from the entrance funnel conductance limit.

The injection time profiles further confirmed that the peak-to-peak amplitude of the RF field had a differential effect on trapping ions with different *m/z* values in various sectors of the mobility region. This phenomenon was first observed during the initial RF amplitude optimization experiments shown in Figure

4-17. An insignificant difference was observed in the absolute number of trapped TAA8 ions compared to TAA12 in sector 2 (Figure 4-18). On the other hand, significantly more TAA12 ions were trapped in sector 3 compared to TAA8 (Figure 4-19). This would suggest that the large RF amplitude that was being applied through the mobility region was inducing a destabilizing effect on the trapped TAA8 ion cloud. Since this was not observed in sector 2 where the I.D. is 20% larger, the relative strength of the hexapolar RF field must be greater.

In conclusion, these results confirmed that the entrance funnel was suitable for controlling the flow of ions into the mobility region, and shorter injection times resulted in more optimal trapping efficiency with fewer losses. Furthermore, these results provided a qualitative measure of the maximum trapping capacity for two sectors and gave additional insight into the ion dynamics occurring during the trapping process in the vfTIMS.

4.5.3.3 Trap Time Evaluation

The last series of experiments in Phase Two of vfTIMS instrument testing assessed the duration for which ions could be trapped and held in sector 2 or sector 3 of the mobility region. In a conventional TIMS experiment, ions are required to remain trapped throughout the entire electric field ramp when the axial electric field strength is decreased during ion elution. Therefore, it was crucial to determine how long ions could be retained in the various sectors of the vfTIMS mobility region. Figure 4-20 and Figure 4-21 present an overview of the results from this experiment. A 20 ms pulse width was used to inject ions into the mobility region, with the trap time ranging from 50 ms to 300 ms, while all other previously described optimized conditions were maintained. In sector 2, minimal losses were observed for both TAA8 and TAA12 when the trapping time was extended to 300 ms (Figure 4-20). The approximately 10% reduction in the integrated area of the trapped peaks could suggest that less space charging and diffusive effects as the ions were continuously held within sector 2 of the mobility region.

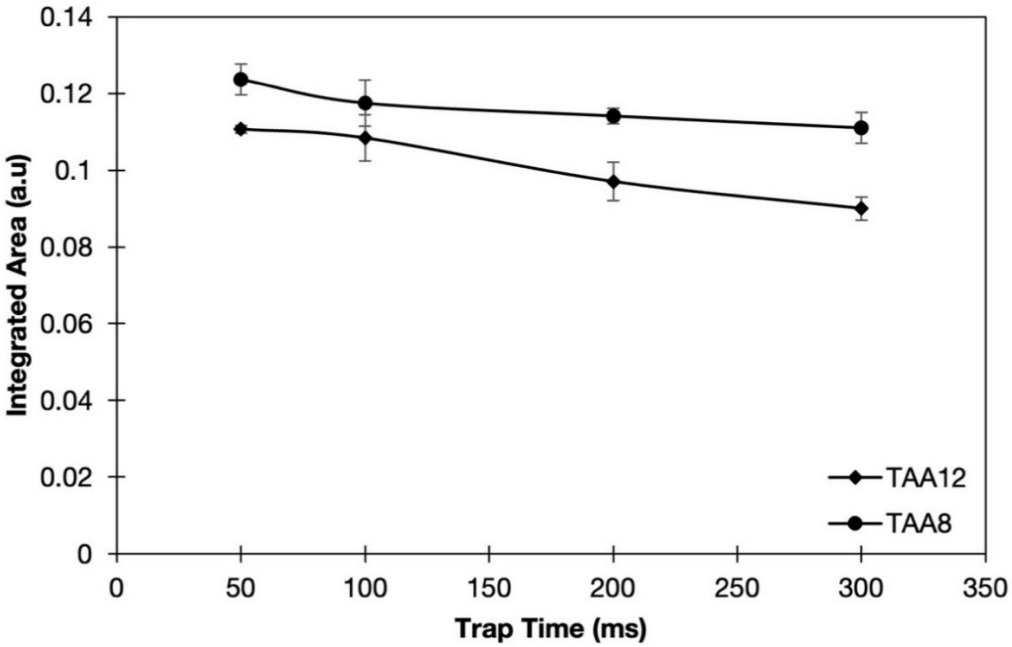

Figure 4-20. Sector 2 (CH14) trap time profile for 25 µM TAA8 and TAA12. 20 ms injection time for all experiments. The average and standard deviation of the trapped peak area was plotted as a function of injection time from the entrance funnel conductance limit.

In sector 3 (Figure 4-21), a more significant decrease in the integrated area of the trapped peaks was observed when the duration of trapping was increased. This observation matched the same trend seen in previous trapping experiments in sector 3. Since the magnitude of the confining RF field was stronger in this region, the ions were compressed more than in sector 2, resulting in more pronounced Coulombic repulsion. To mitigate this issue for future TIMS experiments the use of shorter pulse widths with the conductance limit or a reduction in analyte concentration would reduce the number of ions trapped within the analyzer and minimize ion losses.

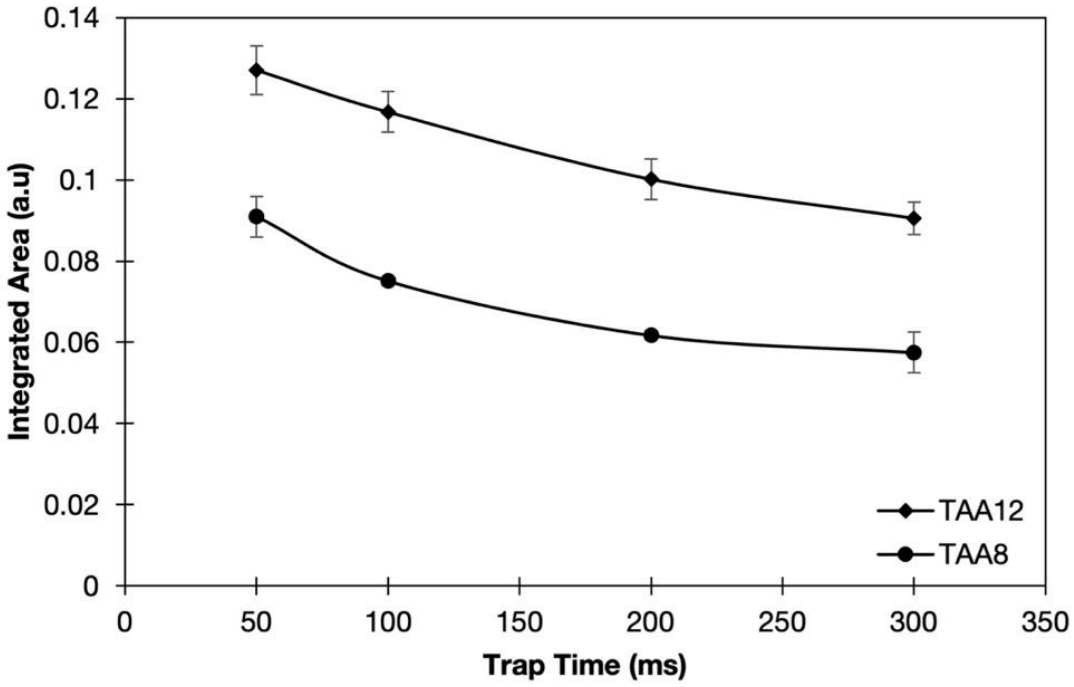

Figure 4-21. Sector 3 (CH22) trap time profile for 25 µM TAA8 and TAA12. 20 ms injection time for all experiments. The average and standard deviation of the trapped peak area was plotted as a function of injection time from the entrance funnel conductance limit.

4.6 Results and Discussion: Phase Three

During Phase Two, the instrument conditions and hardware parameters were optimized to trap ions in one specific sector of the mobility region. This was achieved by applying a repulsive DC potential to a particular set of electrodes, allowing the ions to accumulate for a user-defined period before their release. Notably, the vfTIMS offers a unique capability: it enables independent control over different sectors of the mobility region, allowing ions to be trapped in one sector, released, and then trapped again in a subsequent sector. It is intended that this approach will eventually be applied for high-resolution IMS experiments on the vfTIMS, where ions are initially separated in one sector, eluted, and then separated again in a different sector. Therefore, Phase Three primarily focused on assessing the vfTIMS's ability to perform multiple trap and release experiments on a single packet of injected ions. To sequentially trap ions in different sectors, the MIPS-1 sequence script was modified with a second trap event 100 ms after the first trap event. Using this script, ions would be pulsed into the mobility region through the entrance funnel conductance limit,

trapped for 50 ms in the middle of sector 2 (CH14), then released into sector 3 (CH22) where they were trapped for 100 ms. Following the second trap event, the ions were released to the detector. A visualization of the entire MIPS timing sequence is shown in Figure 4-22. The same instrumental parameters as previous experiments where ions were only trapped in one sector before being released to the detector were used to ensure that accurate comparisons could be made between experiments.

4.6.1 Sequential Two Sector Ion Trapping

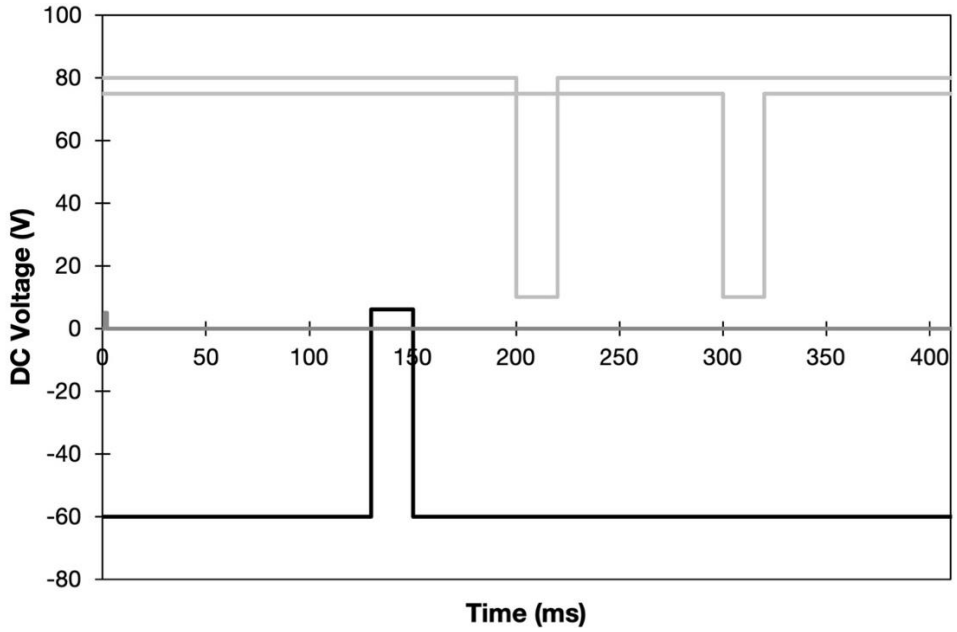

Figure 4-22. MIPS timing sequence for double sector ion trapping with entrance funnel pulsing. Black trace corresponds to the potential on the entrance funnel conductance limit. First light grey trace corresponds to the potential applied to the selected set of electrodes in sector 2 (200 – 220 ms), while second grey trace corresponds to the potential applied to the selected electrodes in sector 3 (300 – 320 ms). Dark grey trace on the far left of the plot corresponds to the two triggers signals (MIPS-2 → MIPS-1, MIPS-2 → Oscilloscope).

As with previous injection time optimization experiments, the pulse width of the conductance limit was varied between 0.5 ms and 100 ms. Individual 25 µM working solutions for TAA8 and TAA12 were infused, the optimized DC EFG and gas flow settings were kept consistent with previous experiments, and the optimal frequency (*i.e.*, 550 kHz), and peak-to-peak amplitude (*i.e.*, 250 Vpp) were applied through the mobility region. Shown in Figure 4-23, as the pulse width of the conductance limit was initially increased from 0.5 ms to 10 ms, the integrated peak area for both TAA ions at each pulse width was essentially the

same. Between 20 ms and 100 ms, the difference between the integrated area of the two ions began to occur, albeit to a lesser degree than when only sector 3 was used to trap ions. Overall, when compared to the trapping in a single sector (either sector 2 or sector 3), the total amount of TAA8 and TAA12 ions decreased. This was likely due to inherent losses that occurred as the ions were released into the next sector of the mobility region for the second trap event.

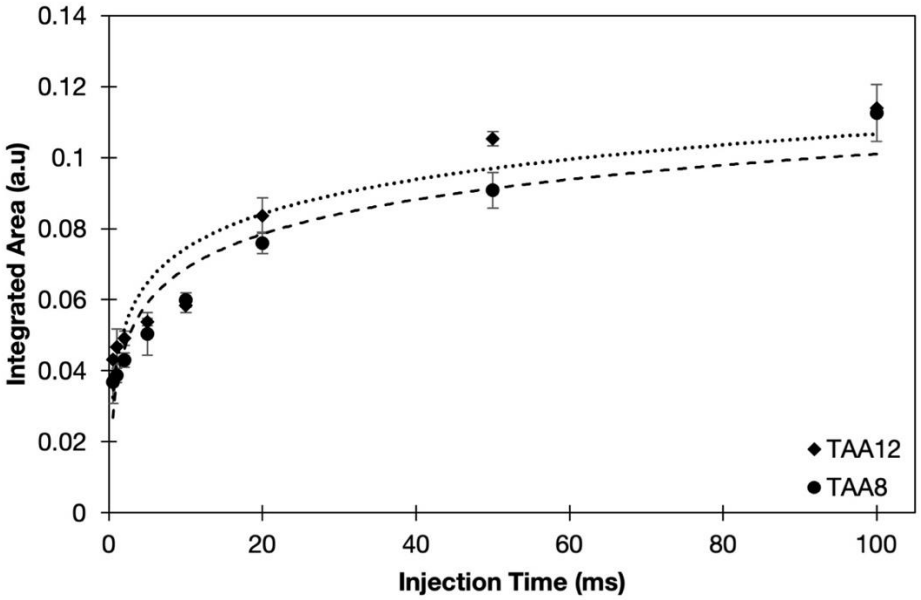

Figure 4-23. Sequential two-sector trapping injection time profile for 25 µM TAA8 and TAA12. First trap event in the middle of sector 2, and second trap event in sector 3. The injection time was varied, and ions were trapped for 50 ms in sector 2 and 100 ms in sector 3. The average and standard deviation of the trapped peak area was plotted as a function of injection time from the entrance funnel conductance limit.

The trapping efficiency of the single sector trapping compared to the two-sector trapping was also quantified. The peak area for trapped TAA8 and TAA12 ions in sector 3 was compared to the peak area from the sequential double trap experiment (sector 2 → sector 3). As shown in Figure 4-24, at very short injection times (0.5 ms to 2 ms), more ions were trapped during the double trapping experiment. As the injection time was increased, the trapping efficiency began to level off to approximately 80% for TAA8 and 65% for TAA12. This experiment highlights that, while the trapping efficiency was higher at short injection times, the variation in the peak area was significant since minor fluctuations in the nanoESI spray had a significant impact on the number of ions that were injected in such a small time-window. However,

beyond the 2 ms injection pulse width, the average integrated area was very consistent. Furthermore, during the transfer of ions between trapping sectors it was clear that losses did occur, however, this was an inherent limitation of the vfTIMS. Future studies should focus on how these losses can be mitigated to ensure near 100% trapping efficiency for multi-sector trap experiments. Overall, implementation of the sequential two-sector trapping scheme was a success, and a significant number of ions were able to be trapped in two different sectors of the instrument prior to detection.

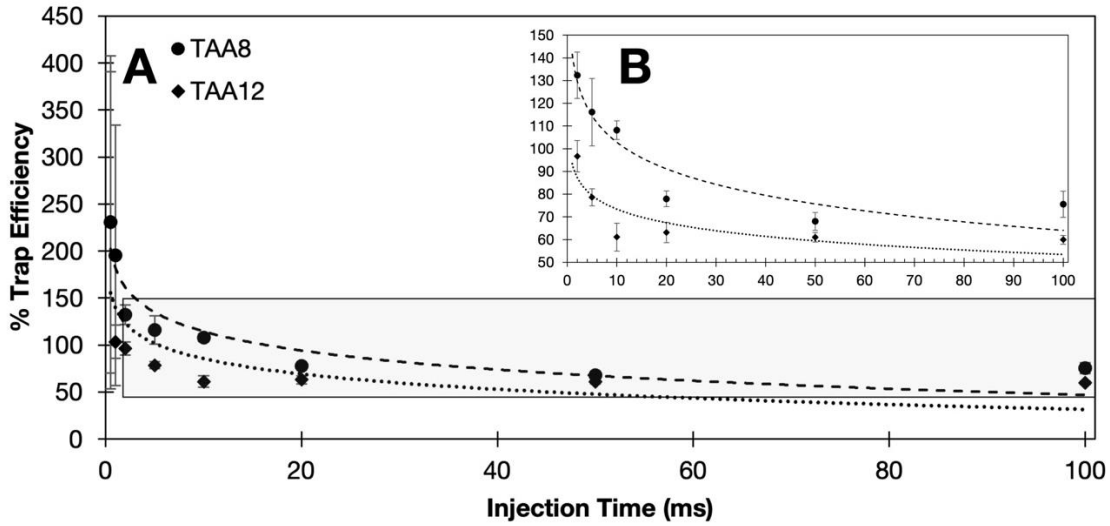

Figure 4-24. Percent trapping efficiency – two-sector trapping versus single-sector trapping. (**A)** Percent difference of the peak area of 25 µM TAA8 and TAA12 from the sequential double trapping experiment compared to the single trapping experiment as a function of injection time. The light grey box corresponds to the zoomed in plot from 50% to 150% shown in the inset (**B**).

4.7 Conclusions

In conclusion, the main objective of the research presented in Chapter 4 was to systematically investigate and identify the optimal set of instrumental parameters for the vfTIMS that would eventually be utilized during ion mobility experiments. To achieve this, the experimental testing was split into three phases. Phase One focused on obtaining stable ion current through the instrument and maximizing the number of ions that were transmitted through the instrument to the detector. In Phase Two, the objective was to develop a method to precisely control the flow of ions entering the mobility region of the vfTIMS and determine the optimal conditions for trapping ions in different sectors. Lastly, Phase Three focused on demonstrating that

ions could be trapped in one sector, eluted, and trapped again in another sector, before being released to the detector. Overall, the main objectives in Chapter 4 were achieved; we determined the instrument settings and hardware parameters needed to transmit ions through the prototype instrument and to trap ions in the various sectors. Through considerable experimental optimization and trial and error, the optimal gas flow, pressure differential, DC EFG and RF settings were optimized for the vfTIMS Transmission Mode and Trap Mode. While full mobility separation was not achieved at this stage of the project, all the instrumental conditions are in place for those experiments to begin.

Chapter 5: Ion Mobility Separation: Two Proof-of-Concept Studies

5.1 Preamble

This chapter has not yet been published. Most of the data presented in Chapter 5 will be used during the preparation of a manuscript for submission to the Review of Scientific Instruments journal in early 2024. All experiments were performed by Daniel Rickert. Data processing and preparation of all figures was done by Daniel Rickert. Data analysis and interpretation was done by Daniel Rickert, Gordon Anderson, Scott Hopkins, and Janusz Pawliszyn. Scott Hopkins and Janusz Pawliszyn were responsible for conceptualization of the project, project supervision, and funding acquisition.

5.2 Introduction

IMS instruments separate ions in the gas phase based on differences in their respective mobilities (*K*). In a DTIMS, ions collide with a neutral bath gas as they are driven through the drift region by an electric field, and the frequency of the ion-neutral collisions induces separation.[23] In a TIMS instrument, ions are propelled through the TIMS tunnel by the flowing column of neutral bath gas, and the axial electric field gradient traps ions where the gas velocity is equal and opposite to the ion's drift velocity. Larger ions (*i.e.*, small *K*) will be pushed deeper into the tunnel, while smaller ions (*i.e.*, large *K*) are trapped closer to the entrance of the analyzer.[27] Throughout Chapter 4, a wide range of experiments were presented that described the initial development of the prototype vfTIMS instrument. Those experiments focused on achieving operability of the instrument and determining the initial working parameters for ion transmission and ion trapping. However, up to that point, mobility separation experiments had not yet been attempted. Thus, Chapter 5 contains two proof-of-concept sets of experiments that attempt to provide the preliminary evidence of the mobility separation capabilities of the vfTIMS.

In the first proof-of-concept, individual working solutions of three TAA analytes (*e.g.*, TAA5, TAA8, TAA12) and morphine were continuously infused into the vfTIMS. While the ions were being infused, an increasingly repulsive DC potential was applied to the central set of electrodes at the midpoint of sectors 2,

3, or 4 in the mobility region. As the magnitude of the repulsive DC potential was increased in a particular sector, the ion current remained constant until a specific voltage was reached, at which point the ion current rapidly diminished. This voltage was referred to as the critical trap voltage. A similar experimental set-up was described by Baykut and coworkers in 2009, where the authors described an experiment where an increasing DC voltage was applied to the last lens of a dual ion funnel to form a potential barrier, which ultimately acted as a mobility filter.[121] Using a variety of small positively charged molecules with increasing *m/z* values (and decreasing mobilities) as test analytes, their work demonstrated that by tuning the critical trap voltage, they could variably filter ions with differing ion mobilities. Our first proof-of-concept aimed to replicate this approach by utilizing the tunable gas flow velocity gradient that is produced throughout the four sectors of the mobility region. In this experiment, the critical trap voltage for a particular ion would increase when it was trapped in sector 2, 3 or 4 due to the increased gas velocity. Similarly, comparison of the critical trap voltage for different ions blocked in the same sector of the mobility region would show that a greater critical trap voltage would be required to trap a larger (low mobility) ion compared a smaller ion (higher mobility), ultimately providing a semi-quantitative measure of the mobility separation capabilities of the vfTIMS.[121] Considered another way, for a particular sector (*e.g.* sector 3) under one set of experimental conditions, the force exerted by the gas/pressure differential would be directly correlated with the mobility of the ion. Larger ions with lower mobilities will experience a larger driving force compared to a small ion with a higher mobility. Thus, the potential barrier required to trap larger ions will be greater than the barrier required to trap a small ions.

In the second proof-of-concept, mobility separation with a mixture of TAA8 and TAA12 ions using the sequential double trapping configuration described in Section 4.6 was attempted. In this experiment, a mixture of TAA8 and TAA12, or individual working solutions of each TAA molecule to act as negative controls were infused into the instrument, pulsed through the entrance funnel conductance limit aperture before being trapped in sector 2 of the mobility region. To evaluate the mobility separation of TAA8 and TAA12, the DC potential applied to the electrodes in sector 4 during the second trap event was varied.

When low trapping potentials are applied in sector 4, once the TAA8 and TAA12 ions are released from sector 2, both ions are transmitted through the subsequent downstream sectors of the mobility region and reach the detector without being trapped (Figure 5-1, A). This would appear experimentally as a single peak occurring after the first trap event, with no peak occurring after the second trapping event. Our hypothesis was that as the trapping potential is increased, the smaller TAA8 ions would begin to be trapped during the second trap event in sector 4 (Figure 5-1, B), but the DC potential would not be strong enough to trap the larger TAA12 ion. As the magnitude of the voltage applied to sector 4 was increased further, eventually TAA12 would begin to be trapped (Figure 5-1, C). If the intensity of the second peak (*e.g.* after the second trap event) was recorded and then plotted relative to the trapping voltage applied in sector 4, the TAA8 ion peak would appear at lower voltages than TAA12. To further visualize this, the first derivative of the sigmoid curves could be plotted a function of the voltage to determine where the inflection point in the data occurred and provide insight into the separation of the ions in the mixture.

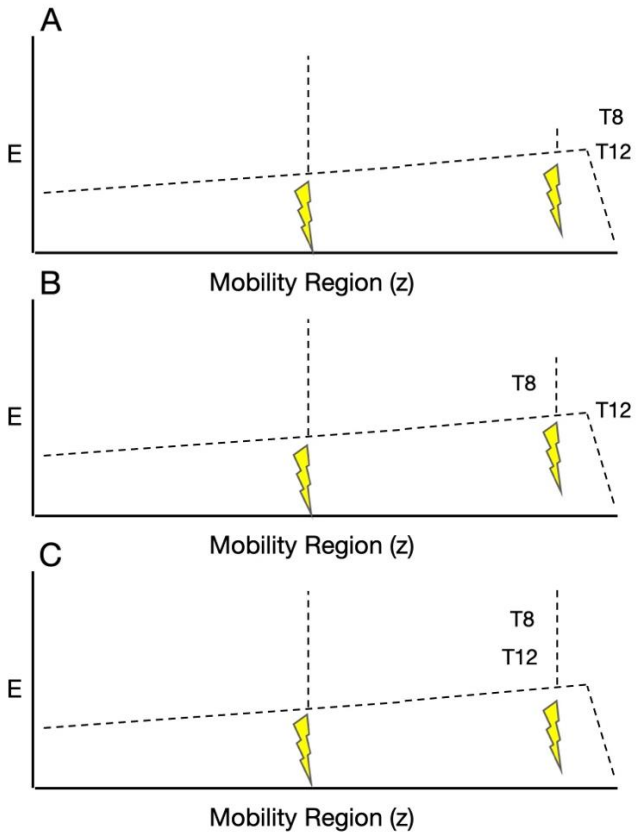

Figure 5-1. Visual schematic of the sequential double trapping experimental scheme with variable trapping in sector 4. A, B, and C correspond to the three expected outcomes detailed above.

In both sets of proof-of-concept experiments, the primary objective was to demonstrate the correlation between the trapping voltage and the ion's mobility. For example, in the first demonstration the critical trap voltage in sector 4 for a small ion like TAA5 would be less than a larger ion like TAA12. Thus, the difference in the critical trap voltage for ions with different mobilities would verify that the magnitude of the applied axial electric field in the mobility region was responsible for inducing separation. In the second demonstration, the magnitude of the trap voltage applied in sector 4 would correlate with the difference in mobility of the ions. This would substantiate why TAA8 was trapped in sector 4 while TAA12 would transmit immediately to the detector at certain trapping potentials. While neither of these experiments truly demonstrated a complete working TIMS instrument, they do provide a more complete picture of the analytical potential of the vfTIMS. As the development of the vfTIMS continues, these results will serve as a framework for the instrumental conditions that are required to separate different ions.

5.3 Proof-of-Concept 1: Continuous Flow Mobility Separation

5.3.1 Experimental Details

Individual 25 µM working solutions of the three TAA analytes (TAA5, TAA8, TAA12) and morphine were infused at 1 µL/min through the nanoESI emitter into the vfTIMS. The DC EFG through the various sectors of the instrument were set using the optimal Trap Mode values. The dipolar RF field through the entrance funnel was set to 760 kHz and 100 Vpp (15% drive), and the hexapolar confining RF field through the mobility region was set to 550 kHz and 250 Vpp. A set of DC electrodes in the center of sector 2 (CH14), sector 3 (CH22), or sector 4 (CH30) were scanned from 0V to +120V in 2V/s measurement intervals. The ion current was measured on the Faraday detector and acquired using the on-board ADC in MIPS-2. Four different gas flow/pressure differential conditions were evaluated to characterize how the gas velocity affected mobility separation and are summarized in

Table 3.

Table 3. Experimental conditions employed during continuous flow mobility separation experiments.

Description	**Instrumental Conditions**			
	Source Region Pressure (Torr)	Detection Region Pressure (Torr)	Pressure Differential (Δ Torr)	N_2 Gas Flow (SLPM)
Standard Gas/Pressure	1.25	0.950	0.3	0.1
Increased Gas/Pressure	1.45	0.950	0.5	0.1
Max Gas/Pressure	1.65	0.950	0.7	0.1
Standard Pressure + Increased Gas	1.25	0.950	0.3	0.3

Pressure measurements taken from gauges on end caps of vacuum chamber. Gas flow measured using flow meter connected to N_2 tank.

5.3.2 Results and Discussion

Four different gas flow/pressure conditions were utilized to investigate the effect of the gas velocity on the critical trap voltage for the selected molecules. To better visualize the critical trap voltage, the “negative” of the first derivative of the ion current as a function of voltage was plotted. An example of the raw ion current, followed by the corresponding “negative” first derivative plot is shown in Figure 5-2.

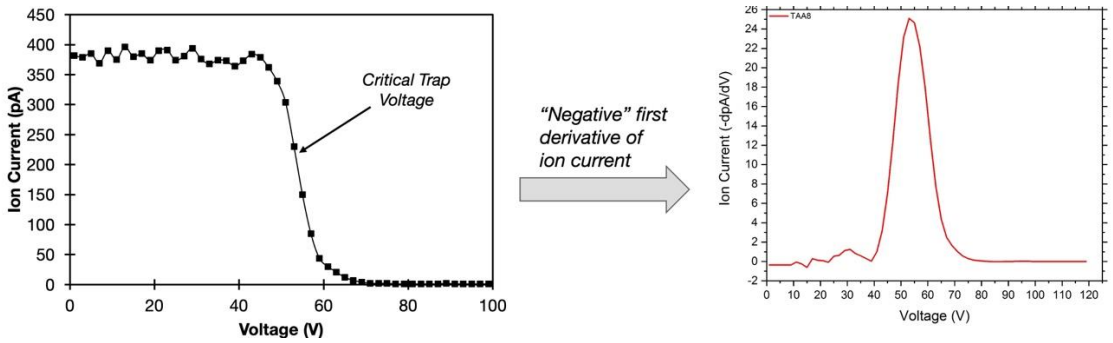

Figure 5-2. Continuous flow mobility separation. **(Left)** Raw experimental data showing ion current dependence on the potential applied to one set of electrodes in the mobility region. **(Right)** Negative first derivative plot for ion current as a function of DC potential (V). Example data from TAA8 – Standard Pressure + High Gas dataset.

The same approach was used by Baykut and coworkers to visualize differences in the critical trap voltage between various analytes more effectively.[121] Comparison of the magnitude of the critical trap voltage and the sharpness of the "peak" for different ions under different conditions provides a semi-quantitative measure for the mobility separation, as well as an approximation of the resolution. To account for variations in the ion current (*i.e.* uncertainty), the raw data was fit using a sigmoid decay function, and the derivative of the fitted data was plotted. The error in the "A" term of the fitting function for each data trace was added as a shadow.

Under the standard gas/pressure differential conditions, (Figure 5-3), as hypothesized, the magnitude of the critical trap voltage increased from sector 2 to sector 4 for each of the analytes. Focusing on sector 2, essentially the same voltage was needed to block TAA5 and morphine while a slightly higher voltage was required for TAA8 and TAA12. In sector 3, the difference between the critical trap voltage became more apparent for the four analytes, and in sector 4, this trend continued and became even more pronounced. This result suggests that when using these instrumental conditions, the best resolution is obtained in the sector with the smallest I.D where the gas velocity was the highest. It should be noted that the ion current for morphine was significantly lower than the other three TAA ions making interpretation of those specific results quite challenging, and additional optimization of the ionization conditions or concentration are required.

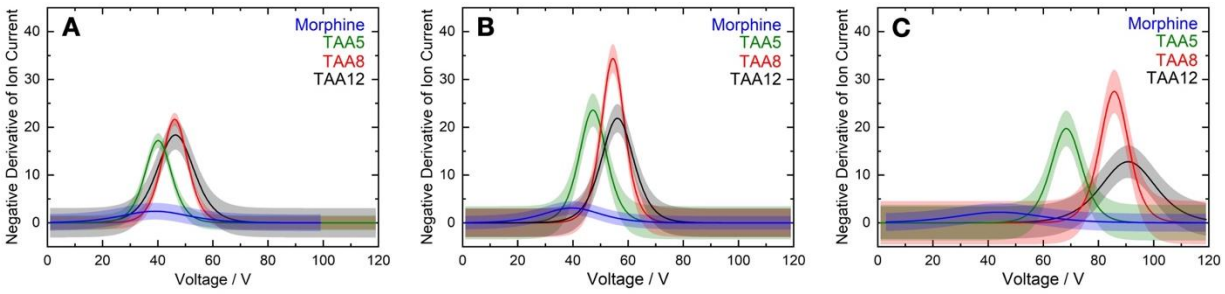

Figure 5-3. Continuous flow mobility separation under Standard Gas/Pressure conditions – Δ 0.3 Torr. The negative first derivative of the fitted ion current is plotted as a function of the voltage (V) applied to the middle set of DC electrodes in the specified sector of the mobility region. The shadow on each line represents the uncertainty (2σ). **(A)** Sector 2 (Channel 14). **(B)** Sector 3 (Channel 22). **(C)** Sector 4 (Channel 30).

When the pressure differential was increased to Δ 0.5 Torr while keeping the N_2 gas flow into the source region constant, improved resolution between the four analytes was observed. The best example of this resolution improvement is seen in Figure 5-4, panel C, where TAA5 and TAA12 are nearly baseline resolved, and TAA8 and TAA12 are now partially resolved. Interestingly, when the pressure differential between the sub-chambers was at the highest achievable magnitude (Δ 0.7 Torr), poorer separation and worse resolution was observed between the four analytes in (Figure 5-5), suggesting that there is a trade-off between the driving force exerted by the gas/pressure differential and the overall separation. Furthermore, there was a noticeable difference in the peak shape of the negative derivatives shown in Figure 5-4 and Figure 5-5. This suggests that as the pressure differential was increased, the peaks in the first derivative plots became considerably wider resulting in a decrease in resolution. Additionally, the increased pressure differential significantly increased the deviation of the ion current, suggesting that the stability of the flow of ions through the instrument was affected by turbulence in the gas flow.

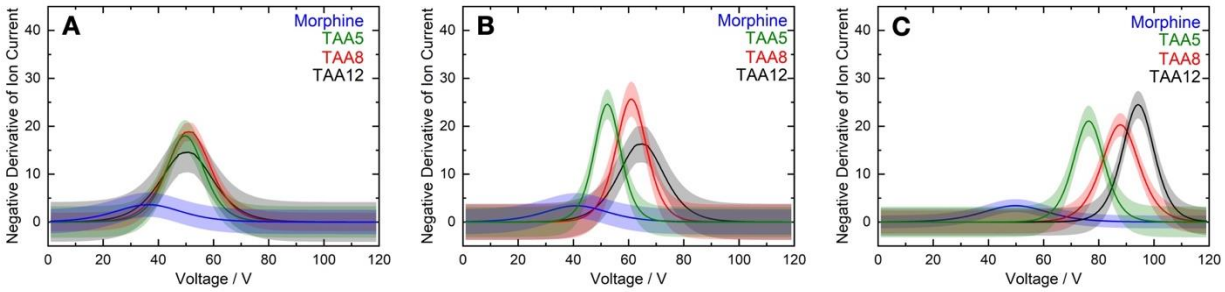

Figure 5-4. Continuous flow mobility separation under Increased Gas/Pressure conditions – Δ 0.5 Torr. The negative first derivative of the fitted ion current is plotted as a function of the voltage (V) applied to the middle set of DC electrodes in the specified sector of the mobility region. The shadow on each line represents the uncertainty (2σ). **(A)** Sector 2 (Channel 14). **(B)** Sector 3 (Channel 22). **(C)** Sector 4 (Channel 30).

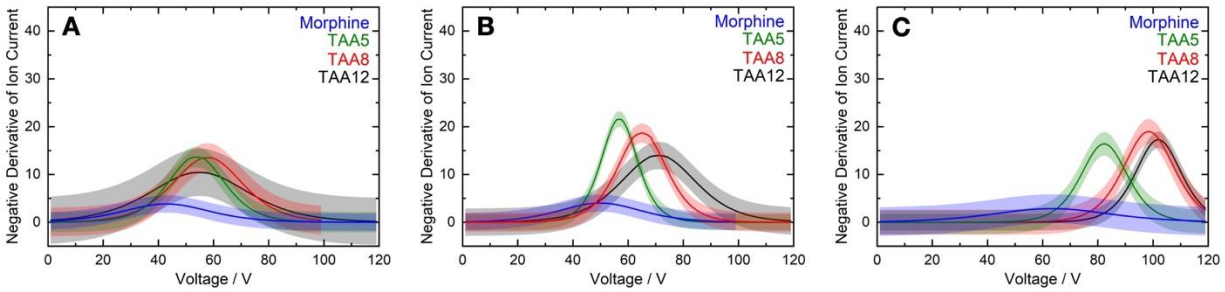

Figure 5-5. Continuous flow mobility separation under Maximum Gas/Pressure conditions – Δ 0.7 Torr. The negative first derivative of the fitted ion current is plotted as a function of the voltage (V) applied to the middle set of DC electrodes in the specified sector of the mobility region. The shadow on each line represents the uncertainty (2σ). **(A)** Sector 2 (Channel 14). **(B)** Sector 3 (Channel 22). **(C)** Sector 4 (Channel 30).

The best results were obtained when the pressure differential was maintained at standard trapping conditions (Δ 0.3 Torr) and the N_2 gas flow was increased from 0.1 SLPM to 0.3 SLPM (Figure 5-6). Under those conditions, the narrowest peak shape was observed, and reasonable resolution was obtained between the critical trap voltages for the four selected analytes. Additionally, the deviation in the ion current was significantly decreased compared to the previous trials. These results from these experiments proved that the magnitude of the blocking potential applied to electrodes in different sectors of the mobility region had a differential effect on the separation of ions with differing mobilities, and matched previously reported work in the literature.[121] Subsequently, once the functionality to smoothly decrease the axial DC EFG

through the mobility region has been implemented on the vfTIMS, the critical trap voltages will serve as a reference point for building the complete TIMS method on the prototype instrument.

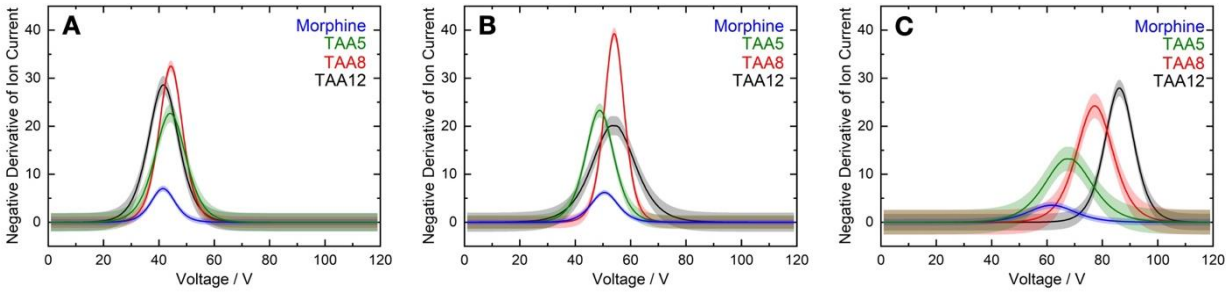

Figure 5-6. Continuous flow mobility separation under standard pressure differential (Δ 0.3 Torr) and increased gas flow (0.3 SLPM N_2) conditions. The negative first derivative of the fitted ion current is plotted as a function of the voltage (V) applied to the middle set of DC electrodes in the specified sector of the mobility region. The shadow on each line represents the uncertainty (2σ). **(A)** Sector 2 (Channel 14). **(B)** Sector 3 (Channel 22). **(C)** Sector 4 (Channel 30).

5.4 Proof-of-Concept 2: Multi-Sector Trapping – Mobility Separation

5.4.1 Experimental Details

A 25 µM mixture of TAA8 and TAA12 or individual 25 µM working solutions of TAA8 and TAA12 were infused at 1 µL/min through the nanoESI emitter into the vfTIMS. The DC EFG through the various sectors of the instrument were set using the optimal Trap Mode values. The dipolar RF field through the entrance funnel was set to 760 kHz and 100 Vpp (15% drive), and the hexapolar confining RF field through the mobility region was set to 550 kHz and 250 Vpp. The pressure differential was set to previously optimized settings of 1.25 Torr in the front half of the chamber and 950 mTorr in the rear of the chamber, while the N_2 flow was maintained at 0.1 SLPM. Using the sequential two sector trapping MIPS script (see Section 4.6), ions were pulsed through the entrance funnel conductance limit into sector 2 of the mobility region with a 50 ms pulse width and were trapped for 50 ms by applying an +65V potential to the DC electrodes in the midpoint of the sector (CH14). After the first trap event, the ions were released into the adjacent sector, where a variable DC potential (+0V to +70V) was applied to the electrodes in the middle of the sector 4 (CH30) to trap ions for 100 ms. The ion current was measured with the Faraday detector and collected using the Tektronix oscilloscope. A visual schematic of the time sequence is given in Figure 5-7.

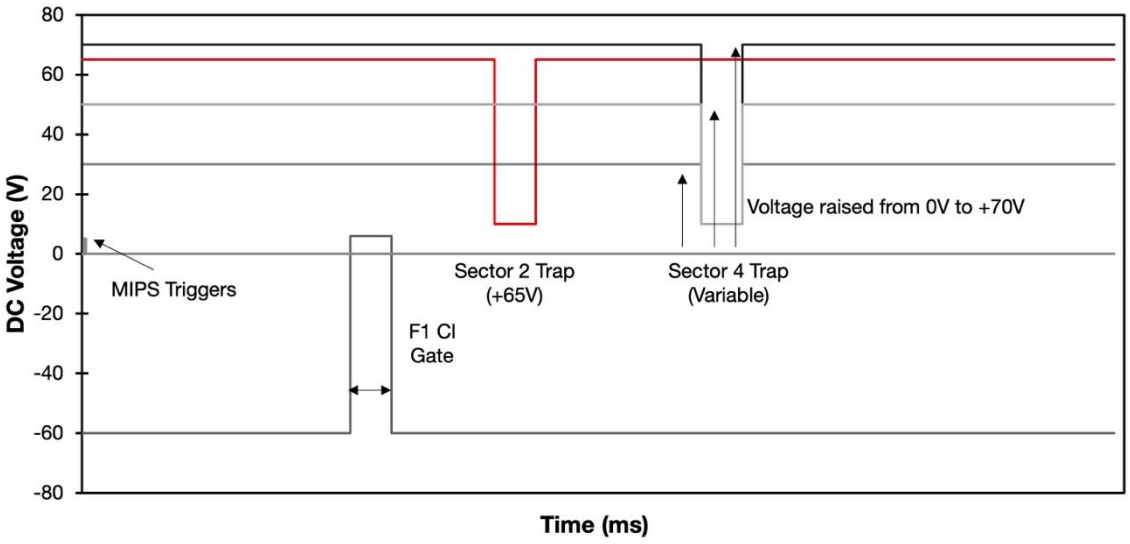

Figure 5-7. MIPS timing sequence for mobility selective two-sector ion trapping.

5.4.2 Results and Discussion

The main objective of the second proof-of-concept study was to demonstrate that the magnitude of the trapping potential could be tuned to selectively trap ions with different mobilities. To attempt to achieve this, a modified two-trap experiment was devised where both ions (TAA8 and TAA12) would be trapped in sector 2 and depending on the magnitude of the trapping potential applied in sector 4, mobility selective trapping would occur. In this experiment, three different outcomes were expected. When a low magnitude potential was applied in sector 3, neither ion would be trapped during the second event, and ions would appear immediately after being released from sector 2. The next outcome would be that when a larger potential is applied in sector 4, TAA8 would be trapped for a second time, but the trapping potential would not be strong enough to also trap TAA12. Since TAA12 has a lower mobility, it will have a correspondingly larger velocity from the force of the flowing gas, thus requiring a larger trapping potential compared to TAA8. In the third outcome, the trapping potential in sector 4 would be large enough to trap both ions.

The results from the second proof-of-concept are shown below in Figure 5-8. Panels A through C depict the relative intensities of the second peak (ions trapped in sector 4) as a function of the voltage applied. For each sample, when the voltage applied in sector 4 was below 35V, the ions were not trapped since the

intensity of the second peak was ~ 0. As the voltage applied to trap the ions was increased past 35V, trapping began to occur, and the relative intensity increased before plateauing.

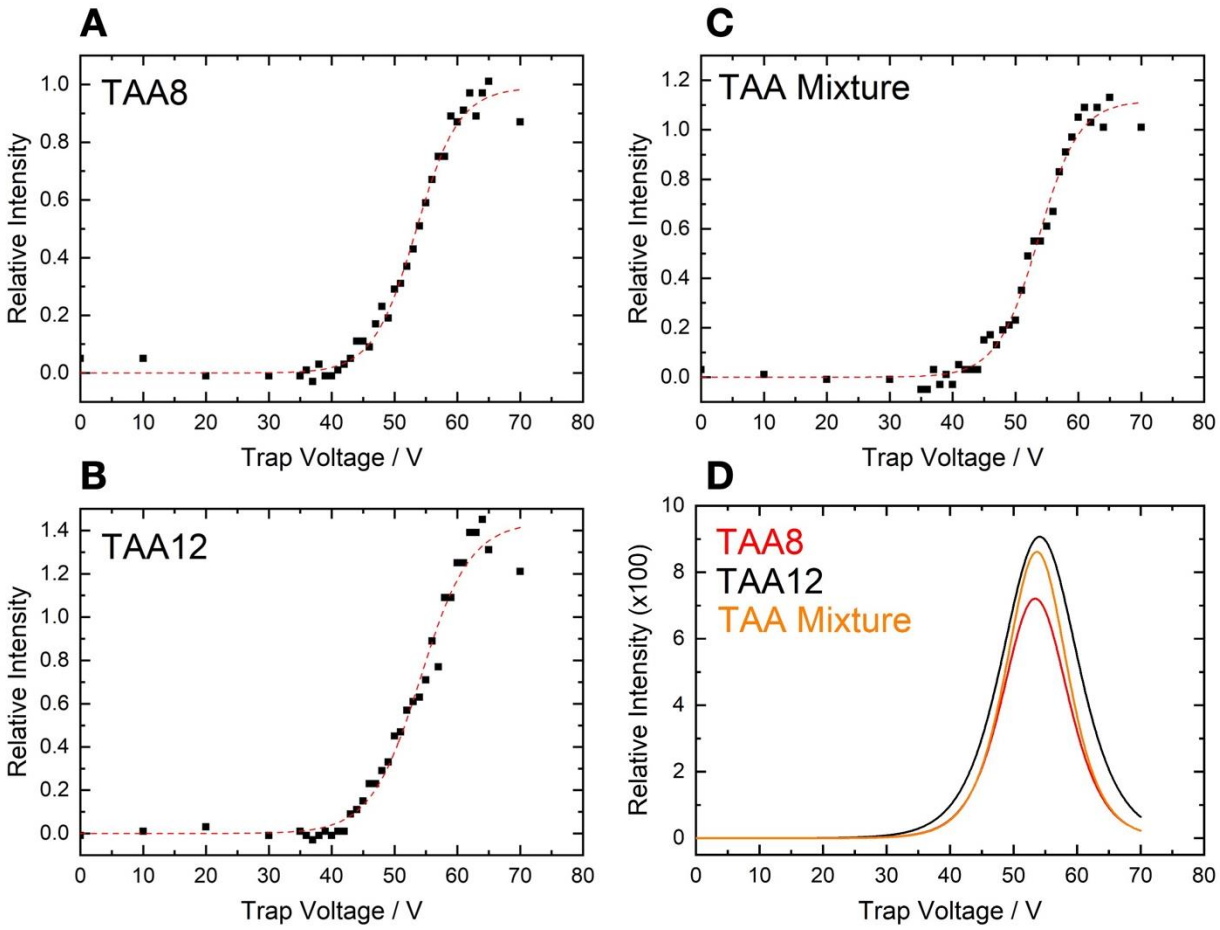

Figure 5-8. Mobility selective two-sector ion trapping. **(A)** Relative intensity of 25 µM TAA8 trapped in sector 4. **(B)** Relative intensity of 25 µM TAA12 trapped in sector 4. **(C)** Relative intensity of the 25 µM TAA mixture trapped in sector 4. **(D)** Fitted first derivative of data traces from panels **A – C**.

Somewhat unexpectedly, and contrary to our hypothesis, significant separation in the trapping voltage applied in sector 4 to trap the different ions was not achieved using the "optimal" set of conditions for ion trapping optimized previously. When the first derivative of the ion traces shown in panels A through C was plotted, it appears that the inflection point (*i.e.* where completely trapping had occurred) was essentially the same. This result does not entirely rule out that separation of different TAA species in a mixture is not possible with the vfTIMS, however more experimentation is clearly required to ascertain the optimal experimental conditions that are required to maximize separation. As shown in the first proof-of-concept,

introducing a slightly higher-pressure differential, or increasing the flow of N_2 into the source region of the instrument would likely improve the overall resolution, even at the detriment of reducing the overall intensity of the trapped ion populations. This result further underscores the fact that the overall functionality of TIMS instruments relies on the dynamic DC potential gradient to trap and separate ions, not a single high potential barrier.

5.5 Conclusions

In summary, the primary goal of the two proof-of-concept experiments described in Chapter 5 was to demonstrate the feasibility of separating different ions based on their mobility using the prototype vfTIMS. In the first proof-of-concept experiment, the critical trap voltage increased when applying a blocking potential in sectors 2, 3, or 4. This finding confirmed that as the gas velocity between sectors increased, a higher voltage was necessary to oppose the flow of ions. Furthermore, when comparing the critical trap voltage for ions with varying mobilities within the same sector, it became evident that larger ions required higher critical trap voltages for blocking. Collectively, these results confirmed that the prototype instrument was indeed functioning as a TIMS, relying on the equilibrium between the gas-induced force and the counteracting electric field to facilitate mobility separation. In the second proof-of-concept experiment, an attempt to demonstrate the interdependence of the trapping potential and ion mobility was attempted but was not completely successful. It is important to note that these experiments had a major limitation in that they relied on a single set of electrodes for blocking ion flow or trapping ions within the mobility region. Further research is needed to implement the capability of establishing an electric field gradient across the mobility region and reducing the potentials on all electrodes, rather than just one set. Although substantial work remains to fully validate the instrument, the preliminary evidence presented in Chapter 5, specifically the first proof-of-concept study underscores the feasibility of mobility separation.

Chapter 6: Summary, Future Perspectives, and Conclusions

6.1 Summary

The research presented in this thesis focused on the development of a new IMS instrument – the variable flow trapped ion mobility spectrometer. Over the course of this PhD work, the main objective was to reach operability of the vfTIMS – taking an idea and turning into a functioning instrument in the lab. Chapter 2 provided a detailed account of the commercial and in-house hardware used to construct the instrument accompanied by an *in-silico* assessment of the gas dynamics and flow profiles. Chapter 3 outlined the electrical components driving the system and included a second *in-silico* study focusing on the electric fields generated within the instrument. Chapter 4 presented the results of experimental optimization and the characterization of the prototype's performance, while Chapter 5 outlined two proof-of-concept studies that aim to provide evidence of ion mobility separation achieved by the constructed device.

6.2 Future Perspectives

At this stage, the instrument development has reached the point where a new set of eyes are needed. While initial operability of the instrument was accomplished, overall, a significant amount of work is still required to accomplish complete IMS functionality. Therefore, a roadmap of what comes next for the instrument is outlined below, separated into short-term, medium-term, and long-term objectives. The vfTIMS has immense potential as a novel analytical tool for rapid ion mobility separations, and much of the groundwork has been laid through my work. While this is surely not an exhaustive list, the objectives outlined below summarize most of the items that must be addressed.

6.2.1 Short Term (6 – 12 months)

The primary concern that requires immediate attention involves the DC EFG within the mobility region, responsible for trapping and separating ions. Specifically, the hardware set-up and MIPS ramp script for scanning down (field strength reduction) of the EFG to elute ions needs to be reconfigured. Currently, the

custom MIPS ramp sequence script (see Appendix C) sets the DC gradient and scans voltages across the defined electrode range to a final gradient (see Figure 6-1 – A). Although this functionality is in place, two unresolved issues require investigation. The first issue pertains to the voltage range for the DC EFG defined in the MIPS script. Addressing this involves continuing the work on two-sector trapping experiments, identifying the different voltages that selectively trap ions, and expanding this voltage range for use as the DC EFG. The second, more significant issue is how the MIPS script reduces the field strength. Presently, the voltage at the bottom of the DC EFG ramp remains constant, while potentials applied to the electrodes ramp down (see Figure 6-1 – A). My experiments and preliminary testing using this approach have been unsuccessful, so I propose reversing this functionality (see Figure 6-1 – B): keeping the voltage at the top of the ramp constant and ramping up the other voltages, akin to a teeter-totter. This mirrors the operation of conventional TIMS.

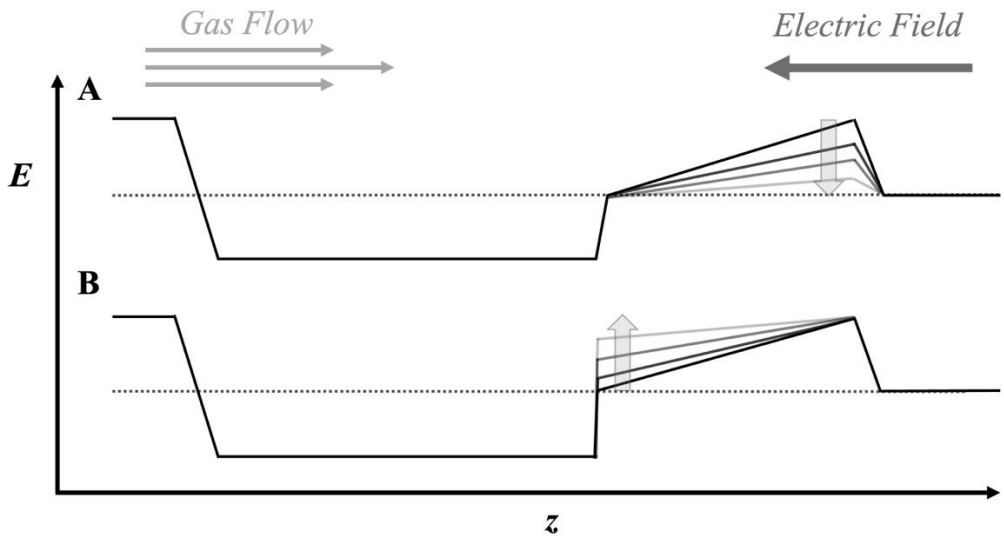

Figure 6-1. (A) Existing MIPS DC EFG scanning functionality. (B) Suggested improved MIPS DC EFG scanning functionality.

The next critical short-term objective is completing the development of a SIMION model for vfTIMS. While no computational model is perfect, an ion trajectory simulation model based on the existing prototype's specifications would offer valuable insights into the complex ion dynamics within the

instrument. This SIMION model would be used to validate experimental results in Chapters 4 and 5 and help refine the DC EFG scanning functionality.

From a hardware perspective, immediate attention is required for reconfiguring the RF amplifiers generating the radially confining RF field through the mobility region. Although having the capability to define the frequency and amplitude of the RF waveform is useful, the observed experimental issues described in Chapter 4 can likely be attributed to the phase-shift between the amplifiers. Running at low frequencies (~550 kHz) significantly impacts trapping small molecules, preventing the trapping of smaller molecules like TAA5 in the mobility region. I suggest maintaining a higher frequency and calibrating one amplifier to eliminate the phase shift, even if it means using only one frequency and amplitude. Alternatively, the second high-Q RF head that was initially going to be used to drive the exit funnel could be connected to the BNC inputs for the mobility region and controlled through the MIPS interface. While this approach would eliminate the ability to dynamically adjust the frequency and peak-to-peak voltage, it would ensure perfect balance between the two RF phases.

Once the other short-term objectives are addressed, more analytes, especially isobaric molecules, need to be analyzed to truly demonstrate the capabilities of the vfTIMS. While the small set of analytes I worked with was useful for developing the baseline instrumental conditions needed to run the instrument, more data needs to be collected to fully characterize the instrument. More specifically, an entire set of TAA molecules from TAA5 to TAA12 should be used, as well as several isobaric TAA molecules.

6.2.2 Medium Term (12 – 36 months)

The medium-term future objectives involve more intensive modifications and improvements to the hardware that encompass the various components of the vfTIMS. As discussed in Chapter 4, the most straightforward improvement would be to redesign the entrance funnel and the interface between the entrance funnel and the mobility region. Adding the biased grid to the conductance limit of the existing entrance funnel would add the ability to accumulate ions prior to injection into the mobility region. Alternatively, a second PCB “tunnel” ion guide with a uniform I.D. that matches the I.D. of the first sector

of the mobility region could be added in series after the existing entrance. This would ensure the gas flow profile would be properly defined through all four sectors of the mobility region with minimal turbulence. Furthermore, if a biased grid was added at the end of the additional PCB ion guide, ions could be accumulated there prior to injection into the analyzer, or potentially even collisionally activated.

Modifications to the mobility region have also been proposed, specifically, changing the design from four sectors with uniform I.D.s to a single funnel with a smooth taper. This design would result in a smooth gas velocity gradient through the instrument and would significantly improve both resolution and ion focusing. To effectively construct the tapered mobility region, the pin electrode design would have to be abandoned, and a PCB configuration would be utilized instead. The PCB design would also help to facilitate a smooth gas flow velocity gradient. The development of a SIMION model to evaluate what the optimal dimensions for the tapered mobility region would be critical for speeding up the development process and could be used to compare with the ion trajectory model built for the existing vfTIMS prototype.

6.2.3 Long Term (36 – 72 months)

The most significant limitation of the current vfTIMS prototype is the complete lack of detector selectivity. While the Faraday detector is useful for preliminary instrument development, its utility is significantly limited when compared to more powerful detector like a mass spectrometer. In the long term, the vfTIMS needs to be interfaced to a mass spectrometer. More specifically, the vfTIMS should be interfaced with a TOFMS. The TOFMS would have the requisite scan speed to provide the *m/z* information that is currently lacking from the first prototype. Presently, the MIPS power supplies have the built-in triggering capabilities to communicate directly with the TOFMS, so from a hardware perspective, that functionality is in place. The biggest challenge would be redesigning the vacuum chamber so it could be connected to the TOFMS, as well additional ion optics to transfer ions exiting from the vfTIMS into the TOFMS. Additionally, an extra vacuum chamber would need to be added between the vfTIMS and the TOFMS to facilitate the differential vacuum pumping that would be required.

Furthermore, the other long-term objective is determining the feasibility of utilizing the variable flow separation approach for an on-site/portable instrument. This is a loftier goal since considerable changes to the existing instrument would be required. An on-site/portable instrument would not be able to operate under the same vacuum conditions currently being used, so the radial RF confinement employed to minimize ion diffusion is not possible. Besides this, the electronics that power the instrument would need to be completely rebuilt and miniaturized. As PCB technology continues to improve, there is potential for the portability and on-site capabilities of the vfTIMS.

6.3 Conclusions

In conclusion, this thesis has laid the groundwork to continue building towards answering the hypothesis that was the motivation for this research:

> *"Can a multi-sector IMS instrument, referred to as the variable flow trapped ion mobility spectrometer (vfTIMS) be designed, and built, as a new tool for high resolution ion mobility separations?"*

The majority of the research objectives were completed, yet there are still several items that need to be studied further. To summarize, a prototype instrument was built that comprised of different commercial and in-house designed components. The electronics that drive the instrument have been designed and installed, and a custom-built interface that controls the system has been developed. All the baseline conditions needed to operate the instrument have been identified, and a considerable amount of research has been dedicated to characterizing the performance of the instrument. The most significant objective that has not been achieved is total functionality of the instrument to truly separate and detect mobility selected ions. The individual components (hardware, software, etc.) are all in place to perform full ion mobility separations, however, I was not able to reach this stage. Instrument development is an extremely arduous process, with many trials, tribulations, and challenging moments. In retrospect, if I knew what I know now, I believe more could have been accomplished. However, someone had to be the first to lay the foundation

for the vfTIMS, and I think I have achieved that. Ultimately, there is always another experiment that can be run, or hardware modification that can be made, so the work never stops.

References

(1) Thomson, J. J.; Rutherford, E. On the Passage of Electricity through Gases Exposed to Röntgen Rays. *The London, Edinburgh, and Dublin Philosophical Magazine and Journal of Science* **1896**, *42* (258), 392–407. https://doi.org/10.1080/14786449608620932.

(2) Thomson, J. J. On the Theory of the Conduction of Electricity through Gases by Charged Ions. *The London, Edinburgh, and Dublin Philosophical Magazine and Journal of Science* **1899**, *47* (286), 253–268. https://doi.org/10.1080/14786449908621258.

(3) Cumeras, R.; Figueras, E.; Davis, C. E.; Baumbach, J. I.; Gràcia, I. Review on Ion Mobility Spectrometry. Part 1: Current Instrumentation. *Analyst* **2015**, *140* (5), 1376–1390. https://doi.org/10.1039/C4AN01100G.

(4) Langevin, P. Researches on Ionized Gases. *Annales de Chimie et de Physique* **1903**, *7*, 289–384.

(5) Langevin, P. Une Formule Fondamentale de Théorie Cinétique. *Annales de Chimie et de Physique* **1905**, *8*, 245–288.

(6) Langevin, P. The Relations of Physics and Electrons to Other Branches of Science. *Congress of arts and science, universal exposition, St. Louis 1904* **1906**, *4*, 121–156.

(7) Cohen, M. J.; Karasek, F. W. Plasma Chromatography - A New Dimension for Gas Chromatography and Mass Spectrometry. *J Chromatogr Sci* **1970**, *8* (6), 330–337. https://doi.org/10.1093/chromsci/8.6.330.

(8) Wilkins, C. L.; Trimpin, S. *Ion Mobility Spectrometry - Mass Spectrometry - Theory and Applications*; CRC Press, 2010.

(9) Eiceman, G.; Karpas, Z.; Hill Jr., H. H. *Ion Mobility Spectrometry*, 3rd ed.; CRC Press, 2013.

(10) Gabelica, V.; Marklund, E. Fundamentals of Ion Mobility Spectrometry. *Curr Opin Chem Biol* **2018**, *42*, 51–59. https://doi.org/10.1016/j.cbpa.2017.10.022.

(11) Gabelica, V.; Shvartsburg, A. A.; Afonso, C.; Barran, P.; Benesch, J. L. P.; Bleiholder, C.; Bowers, M. T.; Bilbao, A.; Bush, M. F.; Campbell, J. L.; Campuzano, I. D. G.; Causon, T.; Clowers, B. H.; Creaser, C. S.; De Pauw, E.; Far, J.; Fernandez-Lima, F.; Fjeldsted, J. C.; Giles, K.; Groessl, M.; Hogan, C. J.; Hann, S.; Kim, H. I.; Kurulugama, R. T.; May, J. C.; McLean, J. A.; Pagel, K.; Richardson, K.; Ridgeway, M. E.; Rosu, F.; Sobott, F.; Thalassinos, K.; Valentine, S. J.; Wyttenbach, T. Recommendations for Reporting Ion Mobility Mass Spectrometry Measurements. *Mass Spectrom Rev* **2019**, *38* (3), 291–320. https://doi.org/10.1002/mas.21585.

(12) Mason, E. A.; McDaniel, E. W. *Transport Properties of Ions in Gases*; Wiley-VCH, 1988. https://doi.org/10.1002/3527602852.

(13) Mason, E. A.; Schamp, H. W. Mobility of Gaseous Lons in Weak Electric Fields. *Ann Phys (N Y)* **1958**, *4* (3), 233–270. https://doi.org/10.1016/0003-4916(58)90049-6.

(14) Viehland, L. A.; Mason, E. A. Gaseous Lon Mobility in Electric Fields of Arbitrary Strength. *Ann Phys (N Y)* **1975**, *91* (2), 499–533. https://doi.org/10.1016/0003-4916(75)90233-X.

(15) Viehland, L. A.; Lin, S. L. Application of the Three-Temperatue Theory of Gaseous Ion Transport. *Chem Phys* **1979**, *43* (1), 135–144. https://doi.org/10.1016/0301-0104(79)80112-3.

(16) Gandhi, V. D.; Hua, L.; Chen, X.; Latif, M.; Larriba-Andaluz, C. A Critical Review of the Two-Temperature Theory and the Derivation of Matrix Elements. High Field Ion Mobility and Energy Calculation for All-Atom Structures in Light Gases Using a 12-6-4 Potential. *Talanta Open* **2023**, *7*, 100191. https://doi.org/10.1016/j.talo.2023.100191.

(17) Haack, A.; Ieritano, C.; Hopkins, W. S. MobCal-MPI 2.0: An Accurate and Parallelized Package for Calculating Field-Dependent Collision Cross Sections and Ion Mobilities. *Analyst* **2023**, *148* (14), 3257–3273. https://doi.org/10.1039/D3AN00545C.

(18) Ridgeway, M. E.; Lubeck, M.; Jordens, J.; Mann, M.; Park, M. A. Trapped Ion Mobility Spectrometry: A Short Review. *Int J Mass Spectrom* **2018**, *425*, 22–35. https://doi.org/10.1016/J.IJMS.2018.01.006.

(19) Baker, E. S.; Clowers, B. H.; Li, F.; Tang, K.; Tolmachev, A. V.; Prior, D. C.; Belov, M. E.; Smith, R. D. Ion Mobility Spectrometry—Mass Spectrometry Performance Using Electrodynamic Ion Funnels and Elevated Drift Gas Pressures. *J Am Soc Mass Spectrom* **2007**, *18* (7), 1176–1187. https://doi.org/10.1016/j.jasms.2007.03.031.

(20) Kim, T.; Tolmachev, A. V.; Harkewicz, R.; Prior, D. C.; Anderson, G.; Udseth, H. R.; Smith, R. D.; Bailey, T. H.; Rakov, S.; Futrell, J. H. Design and Implementation of a New Electrodynamic Ion Funnel. *Anal Chem* **2000**, *72* (10), 2247–2255. https://doi.org/10.1021/ac991412x.

(21) Tang, K.; Shvartsburg, A. A.; Lee, H.-N.; Prior, D. C.; Buschbach, M. A.; Li, F.; Tolmachev, A. V.; Anderson, G. A.; Smith, R. D. High-Sensitivity Ion Mobility Spectrometry/Mass Spectrometry Using Electrodynamic Ion Funnel Interfaces. *Anal Chem* **2005**, *77* (10), 3330–3339. https://doi.org/10.1021/ac048315a.

(22) Kelly, R. T.; Tolmachev, A. V.; Page, J. S.; Tang, K.; Smith, R. D. The Ion Funnel: Theory, Implementations, and Applications. *Mass Spectrom Rev* **2010**, *29* (2), 294–312. https://doi.org/10.1002/mas.20232.

(23) Dodds, J. N.; Baker, E. S. Ion Mobility Spectrometry: Fundamental Concepts, Instrumentation, Applications, and the Road Ahead. *J Am Soc Mass Spectrom* **2019**, *30* (11), 2185–2195. https://doi.org/10.1007/s13361-019-02288-2.

(24) Larriba-Andaluz, C.; Chen, X.; Nahin, M.; Wu, T.; Fukushima, N. Analysis of Ion Motion and Diffusion Confinement in Inverted Drift Tubes and Trapped Ion Mobility Spectrometry Devices. *Anal Chem* **2019**, *91* (1), 919–927. https://doi.org/10.1021/acs.analchem.8b03930.

(25) Fernandez-Lima, F.; Kaplan, D. A.; Suetering, J.; Park, M. A. Gas-Phase Separation Using a Trapped Ion Mobility Spectrometer. *Int J Ion Mobil Spectrom* **2011**, *14* (2–3), 93–98. https://doi.org/10.1007/s12127-011-0067-8.

(26) Fernandez-Lima, F. A.; Kaplan, D. A.; Park, M. A. Note: Integration of Trapped Ion Mobility Spectrometry with Mass Spectrometry. *Rev Sci Instrum* **2011**, *82* (12), 1261061–1261063. https://doi.org/10.1063/1.3665933.

(27) Michelmann, K.; Silveira, J. A.; Ridgeway, M. E.; Park, M. A. Fundamentals of Trapped Ion Mobility Spectrometry. *J Am Soc Mass Spectrom* **2014**, *26* (1), 14–24. https://doi.org/10.1007/s13361-014-0999-4.

(28) Nahin, M.; Oberreit, D.; Fukushima, N.; Larriba-Andaluz, C. Modeling of an Inverted Drift Tube for Improved Mobility Analysis of Aerosol Particles. *Sci Rep* **2017**, *7* (1), 1–11. https://doi.org/10.1038/s41598-017-06448-w.

(29) Zeleny, J. On the Ratio of the Velocities of the Two Ions Produced in Gases by Röntgen Radiation; and on Some Related Phenomena. *The London, Edinburgh, and Dublin Philosophical Magazine and Journal of Science* **1898**, *46* (278), 120–154. https://doi.org/10.1080/14786449808621173.

(30) Fang, X.-H.; Adams, M.; Pawliszyn, J. A Model of Thermally Generated PH Gradients in Tapered Capillaries. *Analyst* **1999**, *124* (3), 335–341. https://doi.org/10.1039/a807951j.

(31) Pawliszyn, J.; Wu, J. Ampholyte-free Isoelectric Focusing of Proteins in Cone Shaped Capillaries. *J Microcolumn Sep* **1993**, *5* (5), 397–401. https://doi.org/10.1002/mcs.1220050502.

(32) Huang, Z.; Ivory, C. F. Digitally Controlled Electrophoretic Focusing. *Anal Chem* **1999**, *71* (8), 1628–1632. https://doi.org/10.1021/AC981160K.

(33) Silveira, J. A.; Michelmann, K.; Ridgeway, M. E.; Park, M. A. Fundamentals of Trapped Ion Mobility Spectrometry Part II: Fluid Dynamics. *J Am Soc Mass Spectrom* **2016**, *27* (4), 585–595. https://doi.org/10.1007/s13361-015-1310-z.

(34) Silveira, J. A.; Ridgeway, M. E.; Park, M. A. High Resolution Trapped Ion Mobility Spectrometery of Peptides. *Anal Chem* **2014**, *86* (12), 5624–5627. https://doi.org/10.1021/ac501261h.

(35) Spraggins, J. M.; Djambazova, K. V.; Rivera, E. S.; Migas, L. G.; Neumann, E. K.; Fuetterer, A.; Suetering, J.; Goedecke, N.; Ly, A.; Van de Plas, R.; Caprioli, R. M. High-Performance Molecular Imaging with MALDI Trapped Ion-Mobility Time-of-Flight (TimsTOF) Mass Spectrometry. *Anal Chem* **2019**, *91* (22), 14552–14560. https://doi.org/10.1021/acs.analchem.9b03612.

(36) Benigni, P.; Fernandez-Lima, F. Oversampling Selective Accumulation Trapped Ion Mobility Spectrometry Coupled to FT-ICR MS: Fundamentals and Applications. *Anal Chem* **2016**, *88* (14), 7404–7412. https://doi.org/10.1021/acs.analchem.6b01946.

(37) Bleiholder, C.; Liu, F. C.; Chai, M. Comment on Effective Temperature and Structural Rearrangement in Trapped Ion Mobility Spectrometry. *Anal Chem* **2020**, *92* (24), 16329–16333. https://doi.org/10.1021/acs.analchem.0c02052.

(38) Naylor, C. N.; Ridgeway, M. E.; Park, M. A.; Clowers, B. H. Evaluation of Trapped Ion Mobility Spectrometry Source Conditions Using Benzylammonium Thermometer Ions. *J Am Soc Mass Spectrom* **2020**, *31* (7), 1593–1602. https://doi.org/10.1021/jasms.0c00151.

(39) Morsa, D.; Hanozin, E.; Eppe, G.; Quinton, L.; Gabelica, V.; Pauw, E. De. Effective Temperature and Structural Rearrangement in Trapped Ion Mobility Spectrometry. *Anal Chem* **2020**, *92* (6), 4573–4582. https://doi.org/10.1021/acs.analchem.9b05850.

(40) Morsa, D.; Hanozin, E.; Gabelica, V.; De Pauw, E. Response to Comment on Effective Temperature and Structural Rearrangement in Trapped Ion Mobility Spectrometry. *Anal Chem* **2020**, *92* (24), 16334–16337. https://doi.org/10.1021/acs.analchem.0c03937.

(41) Hernandez, D. R.; DeBord, J. D.; Ridgeway, M. E.; Kaplan, D. A.; Park, M. A.; Fernandez-Lima, F. Ion Dynamics in a Trapped Ion Mobility Spectrometer. *Analyst* **2014**, *139* (8), 1913–1921. https://doi.org/10.1039/C3AN02174B.

(42) Bleiholder, C. Towards Measuring Ion Mobilities in Non-Stationary Gases and Non-Uniform and Dynamic Electric Fields (I). Transport Equation. *Int J Mass Spectrom* **2016**, *399–400*, 1–9. https://doi.org/10.1016/j.ijms.2016.01.003.

(43) Naylor, C. N.; Reinecke, T.; Ridgeway, M. E.; Park, M. A.; Clowers, B. H. Validation of Calibration Parameters for Trapped Ion Mobility Spectrometry. *J Am Soc Mass Spectrom* **2019**, *30* (10), 2152–2162. https://doi.org/10.1007/s13361-019-02289-1.

(44) Chai, M.; Young, M. N.; Liu, F. C.; Bleiholder, C. A Transferable, Sample-Independent Calibration Procedure for Trapped Ion Mobility Spectrometry (TIMS). *Anal Chem* **2018**, *90* (15), 9040–9047. https://doi.org/10.1021/acs.analchem.8b01326.

(45) Eiceman, G. A.; Nazarov, E. G.; Stone, J. A. Chemical Standards in Ion Mobility Spectrometry. *Anal Chim Acta* **2003**, *493* (2), 185–194. https://doi.org/10.1016/S0003-2670(03)00762-1.

(46) May, J. C.; Morris, C. B.; McLean, J. A. Ion Mobility Collision Cross Section Compendium. *Anal Chem* **2017**, *89* (2), 1032–1044. https://doi.org/10.1021/acs.analchem.6b04905.

(47) Naylor, C. N.; Cabrera, E. R.; Clowers, B. H. A Comparison of the Performance of Modular Standalone Do-It-Yourself Ion Mobility Spectrometry Systems. *J Am Soc Mass Spectrom* **2023**, *34* (4), 586–594. https://doi.org/10.1021/jasms.2c00308.

(48) Ridgeway, M. E.; Bleiholder, C.; Mann, M.; Park, M. A. Trends in Trapped Ion Mobility – Mass Spectrometry Instrumentation. *Trends Analyt Chem* **2019**, *116*, 324–331. https://doi.org/10.1016/j.trac.2019.03.030.

(49) McLuckey, S. A.; Wells, J. M. Mass Analysis at the Advent of the 21st Century. *Chem Rev* **2001**, *101* (2), 571–606. https://doi.org/10.1021/cr990087a.

(50) Hoffmann, E. De; Stroobant, V. *Mass Spectrometry Principles and Applications*, Third Ed.; John Wiley & Sons: West Sussex, England, 2007. https://doi.org/10.1002/9783527654703.ch11.

(51) Merenbloom, S. I.; Koeniger, S. L.; Valentine, S. J.; Plasencia, M. D.; Clemmer, D. E. IMS−IMS and IMS−IMS−IMS/MS for Separating Peptide and Protein Fragment Ions. *Anal Chem* **2006**, *78* (8), 2802–2809. https://doi.org/10.1021/ac052208e.

(52) Koeniger, S. L.; Merenbloom, S. I.; Valentine, S. J.; Jarrold, M. F.; Udseth, H. R.; Smith, R. D.; Clemmer, D. E. An IMS−IMS Analogue of MS−MS. *Anal Chem* **2006**, *78* (12), 4161–4174. https://doi.org/10.1021/ac051060w.

(53) Liu, F. C.; Ridgeway, M. E.; Park, M. A.; Bleiholder, C. Tandem Trapped Ion Mobility Spectrometry. *Analyst* **2018**, *143* (10), 2249–2258. https://doi.org/10.1039/C7AN02054F.

(54) Liu, F. C.; Ridgeway, M. E.; Park, M. A.; Bleiholder, C. Tandem-Trapped Ion Mobility Spectrometry/Mass Spectrometry (t TIMS/MS): A Promising Analytical Method for Investigating Heterogenous Samples. *Analyst* **2022**, *147* (11), 2317–2337. https://doi.org/10.1039/D2AN00335J.

(55) Silveira, J. A.; Ridgeway, M. E.; Laukien, F. H.; Mann, M.; Park, M. A. Parallel Accumulation for 100% Duty Cycle Trapped Ion Mobility-Mass Spectrometry. *Int J Mass Spectrom* **2017**, *413*, 168–175. https://doi.org/10.1016/j.ijms.2016.03.004.

(56) Hopper, J. T. S.; Oldham, N. J. Collision Induced Unfolding of Protein Ions in the Gas Phase Studied by Ion Mobility-Mass Spectrometry: The Effect of Ligand Binding on Conformational Stability. *J Am Soc Mass Spectrom* **2009**, *20* (10), 1851–1858. https://doi.org/10.1016/j.jasms.2009.06.010.

(57) Liu, F. C.; Ridgeway, M. E.; Winfred, J. S. R. V.; Polfer, N. C.; Lee, J.; Theisen, A.; Wootton, C. A.; Park, M. A.; Bleiholder, C. Tandem-trapped Ion Mobility Spectrometry/Mass Spectrometry Coupled with Ultraviolet Photodissociation. *Rapid Commun Mass Spectrom* **2021**, *35* (22), e9192. https://doi.org/10.1002/rcm.9192.

(58) Tolmachev, A. V.; Vilkov, A. N.; Bogdanov, B.; PĂsa-Tolić, L.; Masselon, C. D.; Smith, R. D. Collisional Activation of Ions in RF Ion Traps and Ion Guides: The Effective Ion Temperature

Treatment. *J Am Soc Mass Spectrom* **2004**, *15* (11), 1616–1628. https://doi.org/10.1016/j.jasms.2004.07.014.

(59) Brodbelt, J. S.; Morrison, L. J.; Santos, I. Ultraviolet Photodissociation Mass Spectrometry for Analysis of Biological Molecules. *Chem Rev* **2020**, *120* (7), 3328–3380. https://doi.org/10.1021/acs.chemrev.9b00440.

(60) Simon, A.-L.; Chirot, F.; Choi, C. M.; Clavier, C.; Barbaire, M.; Maurelli, J.; Dagany, X.; MacAleese, L.; Dugourd, P. Tandem Ion Mobility Spectrometry Coupled to Laser Excitation. *Rev Sci Instrum* **2015**, *86* (9), 0941011–0941019. https://doi.org/10.1063/1.4930604.

(61) Bayat, P.; Lesage, D.; Cole, R. B. Tutorial: Ion Activation in Tandem Mass Spectrometry Using Ultra-High Resolution Instrumentation. *Mass Spectrom Rev* **2020**, *39* (5–6), 680–702. https://doi.org/10.1002/mas.21623.

(62) Benigni, P.; Porter, J.; Ridgeway, Mark. E.; Park, Melvin. A.; Fernandez-Lima, F. Increasing Analytical Separation and Duty Cycle with Nonlinear Analytical Mobility Scan Functions in TIMS-FT-ICR MS. *Anal Chem* **2018**, *90* (4), 2446–2450. https://doi.org/10.1021/acs.analchem.7b04053.

(63) Ridgeway, M. E.; Wolff, J. J.; Silveira, J. A.; Lin, C.; Costello, C. E.; Park, M. A. Gated Trapped Ion Mobility Spectrometry Coupled to Fourier Transform Ion Cyclotron Resonance Mass Spectrometry. *Int J Ion Mobil Spectrom* **2016**, *19* (2–3), 77–85. https://doi.org/10.1007/s12127-016-0197-0.

(64) Benigni, P.; Thompson, C. J.; Ridgeway, M. E.; Park, M. A.; Fernandez-Lima, F. Targeted High-Resolution Ion Mobility Separation Coupled to Ultrahigh-Resolution Mass Spectrometry of Endocrine Disruptors in Complex Mixtures. *Anal Chem* **2015**, *87* (8), 4321–4325. https://doi.org/10.1021/ac504866v.

(65) Leyva, D.; Jaffe, R.; Fernandez-Lima, F. Structural Characterization of Dissolved Organic Matter at the Chemical Formula Level Using TIMS-FT-ICR MS/MS. *Anal Chem* **2020**, *92* (17), 11960–11966. https://doi.org/10.1021/acs.analchem.0c02347.

(66) Santos-Fernandez, M.; Jeanne Dit Fouque, K.; Fernandez-Lima, F. Integration of Trapped Ion Mobility Spectrometry and Ultraviolet Photodissociation in a Quadrupolar Ion Trap Mass Spectrometer. *Anal Chem* **2023**, *95* (22), 8417–8422. https://doi.org/10.1021/acs.analchem.3c01220.

(67) Skoog, D.; West, D.; Holler, F.; Crouch, S. *Fundamentals of Analytical Chemistry*; Brooks/Cole: Belmont, CA, 2013. https://doi.org/10.1080/01422419908228843.

(68) Harris, D. C. *Quantitative Chemical Analysis*, 9th ed.; 2016.

(69) Borotto, N. B.; Osho, K. E.; Richards, T. K.; Graham, K. A. Collision-Induced Unfolding of Native-like Protein Ions Within a Trapped Ion Mobility Spectrometry Device. *J Am Soc Mass Spectrom* **2022**, *33* (1), 83–89. https://doi.org/10.1021/jasms.1c00273.

(70) Panczyk, E. M.; Snyder, D. T.; Ridgeway, M. E.; Somogyi, Á.; Park, M. A.; Wysocki, V. H. Surface-Induced Dissociation of Protein Complexes Selected by Trapped Ion Mobility Spectrometry. *Anal Chem* **2021**, *93* (13), 5513–5520. https://doi.org/10.1021/acs.analchem.0c05373.

(71) Miller, S. A.; Jeanne Dit Fouque, K.; Ridgeway, M. E.; Park, M. A.; Fernandez-Lima, F. Trapped Ion Mobility Spectrometry, Ultraviolet Photodissociation, and Time-of-Flight Mass Spectrometry for Gas-Phase Peptide Isobars/Isomers/Conformers Discrimination. *J Am Soc Mass Spectrom* **2022**, *33* (7), 1267–1275. https://doi.org/10.1021/jasms.2c00091.

(72) Paizs, B.; Suhai, S. Fragmentation Pathways of Protonated Peptides. *Mass Spectrom Rev* **2005**, *24* (4), 508–548. https://doi.org/10.1002/mas.20024.

(73) Jeanne Dit Fouque, K.; Fernandez-Lima, F. Recent Advances in Biological Separations Using Trapped Ion Mobility Spectrometry – Mass Spectrometry. *Trends Analyt Chem* **2019**, *116*, 308–315. https://doi.org/10.1016/j.trac.2019.04.010.

(74) Zhou, M.; Wysocki, V. H. Surface Induced Dissociation: Dissecting Noncovalent Protein Complexes in the Gas Phase. *Acc Chem Res* **2014**, *47* (4), 1010–1018. https://doi.org/10.1021/ar400223t.

(75) Baglai, A.; Gargano, A. F. G.; Jordens, J.; Mengerink, Y.; Honing, M.; van der Wal, S.; Schoenmakers, P. J. Comprehensive Lipidomic Analysis of Human Plasma Using Multidimensional Liquid- and Gas-Phase Separations: Two-Dimensional Liquid Chromatography–Mass Spectrometry vs. Liquid Chromatography–Trapped-Ion-Mobility–Mass Spectrometry. *J Chromatogr A* **2017**, *1530*, 90–103. https://doi.org/10.1016/j.chroma.2017.11.014.

(76) Jeanne Dit Fouque, K.; Ramirez, C. E.; Lewis, R. L.; Koelmel, J. P.; Garrett, T. J.; Yost, R. A.; Fernandez-Lima, F. Effective Liquid Chromatography–Trapped Ion Mobility Spectrometry–Mass Spectrometry Separation of Isomeric Lipid Species. *Anal Chem* **2019**, *91* (8), 5021–5027. https://doi.org/10.1021/acs.analchem.8b04979.

(77) Di Poto, C.; Tian, X.; Peng, X.; Heyman, H. M.; Szesny, M.; Hess, S.; Cazares, L. H. Metabolomic Profiling of Human Urine Samples Using LC-TIMS-QTOF Mass Spectrometry. *J Am Soc Mass Spectrom* **2021**, *32* (8), 2072–2080. https://doi.org/10.1021/jasms.0c00467.

(78) Perez de Souza, L.; Alseekh, S.; Scossa, F.; Fernie, A. R. Ultra-High-Performance Liquid Chromatography High-Resolution Mass Spectrometry Variants for Metabolomics Research. *Nat Methods* **2021**, *18* (7), 733–746. https://doi.org/10.1038/s41592-021-01116-4.

(79) Paglia, G.; Smith, A. J.; Astarita, G. Ion Mobility Mass Spectrometry in the Omics Era: Challenges and Opportunities for Metabolomics and Lipidomics. *Mass Spectrom Rev* **2022**, *41* (5), 722–765. https://doi.org/10.1002/mas.21686.

(80) Moses, T.; Burgess, K. Right in Two: Capabilities of Ion Mobility Spectrometry for Untargeted Metabolomics. *Front Mol Biosci* **2023**, *10*, 1230282. https://doi.org/10.3389/fmolb.2023.1230282.

(81) Meier, F.; Park, M. A.; Mann, M. Trapped Ion Mobility Spectrometry and Parallel Accumulation–Serial Fragmentation in Proteomics. *Mol Cell Proteom* **2021**, *20*, 100138. https://doi.org/10.1016/j.mcpro.2021.100138.

(82) Mun, D.-G.; Bhat, F. A.; Ding, H.; Madden, B. J.; Natesampillai, S.; Badley, A. D.; Johnson, K. L.; Kelly, R. T.; Pandey, A. Optimizing Single Cell Proteomics Using Trapped Ion Mobility Spectrometry for Label-Free Experiments. *Analyst* **2023**, *148* (15), 3466–3475. https://doi.org/10.1039/D3AN00080J.

(83) Coughlan, N. J. A.; Carr, P. J. J.; Walker, S. C.; Zhou, C.; Guna, M.; Campbell, J. L.; Hopkins, W. S. Measuring Electronic Spectra of Differential Mobility-Selected Ions in the Gas Phase. *J Am Soc Mass Spectrom* **2020**, *31* (2), 405–410. https://doi.org/10.1021/jasms.9b00039.

(84) Kafader, J. O.; Melani, R. D.; Schachner, L. F.; Ives, A. N.; Patrie, S. M.; Kelleher, N. L.; Compton, P. D. Native vs Denatured: An in Depth Investigation of Charge State and Isotope Distributions. *J Am Soc Mass Spectrom* **2020**, *31* (3), 574–581. https://doi.org/10.1021/jasms.9b00040.

(85) Lanucara, F.; Holman, S. W.; Gray, C. J.; Eyers, C. E. The Power of Ion Mobility-Mass Spectrometry for Structural Characterization and the Study of Conformational Dynamics. *Nat Chem* **2014**, *6* (4), 281–294. https://doi.org/10.1038/nchem.1889.

(86) Bennett, J. L.; Nguyen, G. T. H.; Donald, W. A. Protein–Small Molecule Interactions in Native Mass Spectrometry. *Chem Rev* **2022**, *122* (8), 7327–7385. https://doi.org/10.1021/acs.chemrev.1c00293.

(87) Liu, F. C.; Cropley, T. C.; Bleiholder, C. Elucidating Structures of Protein Complexes by Collision-Induced Dissociation at Elevated Gas Pressures. *J Am Soc Mass Spectrom* **2023**, *34* (10), 2247–2258. https://doi.org/10.1021/jasms.3c00191.

(88) Jeanne Dit Fouque, K.; Sipe, S. N.; Garabedian, A.; Mejia, G.; Su, L.; Hossen, M. L.; Chapagain, P. P.; Leng, F.; Brodbelt, J. S.; Fernandez-Lima, F. Exploring the Conformational and Binding Dynamics of HMGA2·DNA Complexes Using Trapped Ion Mobility Spectrometry–Mass Spectrometry. *J Am Soc Mass Spectrom* **2022**, *33* (7), 1103–1112. https://doi.org/10.1021/jasms.2c00101.

(89) Liu, F. C.; Cropley, T. C.; Ridgeway, M. E.; Park, M. A.; Bleiholder, C. Structural Analysis of the Glycoprotein Complex Avidin by Tandem-Trapped Ion Mobility Spectrometry–Mass Spectrometry (Tandem-TIMS/MS). *Anal Chem* **2020**, *92* (6), 4459–4467. https://doi.org/10.1021/acs.analchem.9b05481.

(90) Jeanne Dit Fouque, K.; Garabedian, A.; Leng, F.; Tse-Dinh, Y.-C.; Ridgeway, M. E.; Park, M. A.; Fernandez-Lima, F. Trapped Ion Mobility Spectrometry of Native Macromolecular Assemblies. *Anal Chem* **2021**, *93* (5), 2933–2941. https://doi.org/10.1021/acs.analchem.0c04556.

(91) Benigni, P.; Marin, R.; Molano-Arevalo, J. C.; Garabedian, A.; Wolff, J. J.; Ridgeway, M. E.; Park, M. A.; Fernandez-Lima, F. Towards the Analysis of High Molecular Weight Proteins and Protein Complexes Using TIMS-MS. *Int J Ion Mobil Spectrom* **2016**, *19* (2–3), 95–104. https://doi.org/10.1007/s12127-016-0201-8.

(92) Jeanne Dit Fouque, K.; Garabedian, A.; Leng, F.; Tse-Dinh, Y.-C.; Fernandez-Lima, F. Microheterogeneity of Topoisomerase IA/IB and Their DNA-Bound States. *ACS Omega* **2019**, *4* (2), 3619–3626. https://doi.org/10.1021/acsomega.8b02887.

(93) Fenn, J. B.; Mann, M.; Meng, C. K.; Wong, S. F.; Whitehouse, C. M. Electrospray Ionization–Principles and Practice. *Mass Spectrom Rev* **1990**, *9* (1), 37–70. https://doi.org/10.1002/mas.1280090103.

(94) Gómez-Ríos, G. A.; Reyes-Garcés, N.; Bojko, B.; Pawliszyn, J. Biocompatible Solid-Phase Microextraction Nanoelectrospray Ionization: An Unexploited Tool in Bioanalysis. *Anal Chem* **2016**, *88* (2), 1259–1265. https://doi.org/10.1021/acs.analchem.5b03668.

(95) Hu, B.; Zheng, B.; Rickert, D.; Gómez-Ríos, G. A.; Bojko, B.; Pawliszyn, J.; Yao, Z.-P. Direct Coupling of Solid Phase Microextraction with Electrospray Ionization Mass Spectrometry: A Case Study for Detection of Ketamine in Urine. *Anal Chim Acta* **2019**, *1075*, 112–119. https://doi.org/10.1016/j.aca.2019.05.044.

(96) Raab, S. A.; El-Baba, T. J.; Laganowsky, A.; Russell, D. H.; Valentine, S. J.; Clemmer, D. E. Protons Are Fast and Smart; Proteins Are Slow and Dumb: On the Relationship of Electrospray Ionization Charge States and Conformations. *J Am Soc Mass Spectrom* **2021**, *32* (7), 1553–1561. https://doi.org/10.1021/jasms.1c00100.

(97) Shaffer, S. A.; Prior, D. C.; Anderson, G. A.; Udseth, H. R.; Smith, R. D. An Ion Funnel Interface for Improved Ion Focusing and Sensitivity Using Electrospray Ionization Mass Spectrometry. *Anal Chem* **1998**, *70* (19), 4111–4119. https://doi.org/10.1021/ac9802170.

(98) Ibrahim, Y. M.; Baker, E. S.; Danielson, W. F.; Norheim, R. V.; Prior, D. C.; Anderson, G. A.; Belov, M. E.; Smith, R. D. Development of a New Ion Mobility Time-of-Flight Mass Spectrometer. *Int J Mass Spectrom* **2015**, *377*, 655–662. https://doi.org/10.1016/j.ijms.2014.07.034.

(99) Reinecke, T.; Clowers, B. H. Implementation of a Flexible, Open-Source Platform for Ion Mobility Spectrometry. *HardwareX* **2018**, *4*, e00030. https://doi.org/10.1016/j.ohx.2018.e00030.

(100) Moore, J. H.; Davis, C. C.; Coplan, M. A. *Building Scientific Apparatus*; Cambridge University Press, 2009.

(101) Skoog, D. A.; Crouch, S. R.; Holler, F. J. *Instrumental Analysis Principles, 7th Edition*; 2016.

(102) Paultre, A. *Considerations on high q capacitors*. https://www.powerelectronicsnews.com/considerations-on-high-q-capacitors/.

(103) Clowers, B. H.; Ibrahim, Y. M.; Prior, D. C.; Danielson, W. F.; Belov, M. E.; Smith, R. D. Enhanced Ion Utilization Efficiency Using an Electrodynamic Ion Funnel Trap as an Injection Mechanism for Ion Mobility Spectrometry. *Anal Chem* **2008**, *80* (3), 612–623. https://doi.org/10.1021/ac701648p.

(104) Hopkins, S.; Pawliszyn, J. B. ION MOBILITY SPECTROMETER AND METHOD OF ANALYZING IONS. 20210048411, 2021.

(105) Chen, Y.; Leach, F. E.; Kaiser, N. K.; Dang, X.; Ibrahim, Y. M.; Norheim, R. V.; Anderson, G. A.; Smith, R. D.; Marshall, A. G. Improved Ion Optics for Introduction of Ions into a 9.4-T Fourier Transform Ion Cyclotron Resonance Mass Spectrometer. *J Mass Spectrom* **2015**, *50* (1), 280–284. https://doi.org/10.1002/jms.3523.

(106) Shao, Q.; Zhao, J. Ion Trajectory Simulations of a Conical Octopole Ion Guide and Its Comparison with a Parallel One in Chemical Ionization Mass Spectrometric Applications. *Rapid Commun Mass Spectrom* **2018**, *32* (12), 965–972. https://doi.org/10.1002/RCM.8129.

(107) COMSOL Multiphysics. *Quadrupole Mass Filter*. https://www.comsol.com/model/quadrupole-mass-filter-12039.

(108) Kinlein, Z. R.; Anderson, G. A.; Clowers, B. H. Accelerating Prototyping Experiments for Traveling Wave Structures for Lossless Ion Manipulations. *Talanta* **2022**, *244*, 123446. https://doi.org/10.1016/j.talanta.2022.123446.

(109) Raffaelli, A.; Bruins, A. P. Factors Affecting the Ionization Efficiency of Quaternary Ammonium Compounds in Electrospray/Ionspray Mass Spectrometry. *Rapid Commun Mass Spectrom* **1991**, *5* (6), 269–275. https://doi.org/10.1002/rcm.1290050605.

(110) Ude, S.; de la Mora, J. F. Molecular Monodisperse Mobility and Mass Standards from Electrosprays of Tetra-Alkyl Ammonium Halides. *J Aerosol Sci* **2005**, *36* (10), 1224–1237. https://doi.org/10.1016/j.jaerosci.2005.02.009.

(111) Hines, K. M.; May, J. C.; McLean, J. A.; Xu, L. Evaluation of Collision Cross Section Calibrants for Structural Analysis of Lipids by Traveling Wave Ion Mobility-Mass Spectrometry. *Anal Chem* **2016**, *88* (14), 7329–7336. https://doi.org/10.1021/acs.analchem.6b01728.

(112) Stow, S. M.; Causon, T. J.; Zheng, X.; Kurulugama, R. T.; Mairinger, T.; May, J. C.; Rennie, E. E.; Baker, E. S.; Smith, R. D.; McLean, J. A.; Hann, S.; Fjeldsted, J. C. An Interlaboratory Evaluation of Drift Tube Ion Mobility–Mass Spectrometry Collision Cross Section Measurements. *Anal Chem* **2017**, *89* (17), 9048–9055. https://doi.org/10.1021/acs.analchem.7b01729.

(113) Rickert, D.; Gómez-Ríos, G. A.; Singh, V.; Pawliszyn, J. Understanding the Effect of Spatial Positioning of Coated Blade Spray Devices Relative to the Mass Spectrometry Inlet on Different Instrument Platforms and Its Application to Quantitative Analysis of Fentanyl and Related Analogs. *Rapid Commun Mass Spectrom* **2022**, *36* (22), e9388. https://doi.org/10.1002/rcm.9388.

(114) Ibrahim, Y.; Tang, K.; Tolmachev, A. V.; Shvartsburg, A. A.; Smith, R. D. Improving Mass Spectrometer Sensitivity Using a High-Pressure Electrodynamic Ion Funnel Interface. *J Am Soc Mass Spectrom* **2006**, *17* (9), 1299–1305. https://doi.org/10.1016/j.jasms.2006.06.005.

(115) Page, J. S.; Tolmachev, A. V.; Tang, K.; Smith, R. D. Theoretical and Experimental Evaluation of the Low m/z Transmission of an Electrodynamic Ion Funnel. *J Am Soc Mass Spectrom* **2006**, *17* (4), 586–592. https://doi.org/10.1016/j.jasms.2005.12.013.

(116) Page, J. S.; Tolmachev, A. V.; Tang, K.; Smith, R. D. Variable Low-Mass Filtering Using an Electrodynamic Ion Funnel. *J Mass Spectrom* **2005**, *40* (9), 1215–1222. https://doi.org/10.1002/JMS.900.

(117) Tolmachev, A. V.; Kim, T.; Udseth, H. R.; Smith, R. D.; Bailey, T. H.; Futrell, J. H. Simulation-Based Optimization of the Electrodynamic Ion Funnel for High Sensitivity Electrospray Ionization Mass Spectrometry. *Int J Mass Spectrom* **2000**, *203* (1–3), 31–47. https://doi.org/10.1016/S1387-3806(00)00265-7.

(118) Garcia, L.; Saba, C.; Manocchio, G.; Anderson, G. A.; Davis, E.; Clowers, B. H. An Open Source Ion Gate Pulser for Ion Mobility Spectrometry. *Int J Ion Mobil Spectrom* **2017**, *20* (3–4), 87–93. https://doi.org/10.1007/s12127-017-0223-x.

(119) Chen, C.; Tabrizchi, M.; Li, H. Ion Gating in Ion Mobility Spectrometry: Principles and Advances. *Trends Analyt Chem* **2020**, *133*, 116100. https://doi.org/10.1016/j.trac.2020.116100.

(120) Puton, J.; Knap, A.; Siodłowski, B. Modelling of Penetration of Ions through a Shutter Grid in Ion Mobility Spectrometers. *Sens Actuators B Chem* **2008**, *135* (1), 116–121. https://doi.org/10.1016/j.snb.2008.08.011.

(121) Baykut, G.; von Halem, O.; Raether, O. Applying a Dynamic Method to the Measurement of Ion Mobility. *J Am Soc Mass Spectrom* **2009**, *20* (11), 2070–2081. https://doi.org/10.1016/j.jasms.2009.07.013.

Appendices

Appendix A: Summary of Additional Research Contributions

This section serves as a summary of the other research projects I was involved in throughout my PhD that have been published to date. They are listed in chronological order, with the most recent publication listed first. Included in each entry is the citation, a copy of the abstract as it appears in the published version of the manuscript, and a summary of my contributions to the manuscript.

1. Nazdrajić, E., **Rickert, D.,** & Pawliszyn, J. (2023). Rapid Analysis of Fentanyl and Fentanyl Analogues from Whole Blood using SPME coupled to Microfluidic Open Interface. *Analytical Chemistry, 96(2), 821-827.*

Abstract: Fentanyl and its analogues are potent opioids that pose a significant threat to society. Over the last several years, considerable focus has been on the disturbing increasing trend of their usage as street drug. Fentanyl analogues are mainly synthesized to evade analytical detection or increase their potency; thus, very low concentrations are sufficient to achieve the therapeutic effect. In an effort to help combat the synthetic opioid epidemic, developing targeted mass spectrometric methods for quantifying fentanyl and its analogues at ultra-low concentrations is incredibly important. Most methods used to analyze fentanyl and its analogues from whole blood require manual sample preparation protocols (solid phase extraction or liquid-liquid extraction) followed by chromatographic separation and mass spectrometric detection. The main disadvantages of these methods are the tedious sample preparation workflows resulting in lengthy analysis times. To mitigate these issues, we present a targeted method capable of analyzing 96 samples containing fentanyl, several fentanyl analogues, and a common fentanyl (analogue) precursor simultaneously in 2.4 min per sample. This is possible by using a high-throughput semi-automated solid phase microextraction (SPME) workflow followed by direct-to-mass spectrometry determination facilitated by the microfluidic open interface. Our

quantitative method is capable of extremely sensitive analysis, with limits of quantification ranging from 0.002 – 0.031 ng mL^{-1} and linearity ranging from 0.010 – 25.0 ng mL^{-1}. The method shows very good reproducibility (1 – 18 %), accuracy (81 – 100 %) of calibration and validation points and good inter-day reproducibility (6 – 15 %).

Contribution: Equal first authorship. EN and I planned and executed the experiments together. EN processed the data, and both of us worked equally on data interpretation. EN wrote the first draft of the manuscript, and both of us were responsible for edits and changes to the final version submitted to the journal.

2. Nazdrajić, E., Murtada, K., **Rickert, D. A.,** & Pawliszyn, J. (2023). Coupling of Solid-Phase Microextraction Directly to Mass Spectrometry via an Improved Microfluidic Open Interface to Facilitate High-Throughput Determinations. *Journal of the American Society for Mass Spectrometry, 34(6), 1006 – 1014.*

Abstract: Mass spectrometry analysis can be performed by introducing samples directly to mass spectrometry, allowing the increase of the analysis throughput; however, some disadvantages of direct-to-mass spectrometry analysis include susceptibility to matrix effects and risk of instrument contamination from inadequate sample preparation. Solid-phase microextraction is one of the most suitable sample preparation methods for direct-to-mass spectrometry analysis, as it offers matrix-compatible coatings which ensure analyte enrichment with minimal or no interference from matrix. One of the ways solid-phase microextraction can be coupled directly to mass spectrometry is via a microfluidic open interface. This manuscript reports improvements made to the initial microfluidic open interface design, where the system components have been simplified to mostly commercially available materials. In addition, the analysis of samples has been automated by implementing software that fully controls the analysis workflow, where the washing procedure is optimized to completely reduce the carryover. Herein, the extraction and desorption time profiles from thin and thick SPME

devices was studied where the overall workflow consisted of high-throughput sample preparation of 1.3 min per 96 samples and <1 min per sample instrumental analysis.

Contribution: Assisted EN with experiments with acetylfentanyl to assess reproducibility of the system. Assisted with data interpretation. Assisted with preparation of the manuscript and provided edits/input into the final accepted version.

3. **Rickert, D.,** Gómez-Ríos, G. A., Singh, V., & Pawliszyn, J. (2022). Understanding the effect of spatial positioning of coated blade spray devices relative to the mass spectrometry inlet on different instrument platforms and its application to quantitative analysis of fentanyl and related analogs. *Rapid Communications in Mass Spectrometry, 36(22), e9388.*

Abstract: We evaluated the effect that the spatial positioning of coated-blade spray (CBS) devices with respect to the mass spectrometry (MS) inlet has when coupling to diverse MS platforms (i.e., triple quadrupole, linear ion trap and time of flight). Furthermore, as a proof of concept, we evaluated CBS-MS as a tool for quantitation of fentanyl and four analogues on said instruments. Custom-made MS interfaces were made to accurately position the blade in front of the MS inlet. CBS devices, coated with hydrophilic–lipophilic balanced particles, were used for both the optimization of the CBS position and the quantitation of fentanyl and analogues in urine and plasma samples on all instruments. The SCIEX triple quadrupole instrument was the most sensitive to the position of the blade due to the presence of a curtain gas flowing laminarly out of the MS inlet. After optimization, the analytical capabilities of CBS on each instrument were assessed and the results obtained on both SCIEX and Waters platforms matched the performance obtained using a more advanced instrument by ThermoFisher Scientific. Furthermore, excellent figures of merit were attained for the quantitation of fentanyl and analogues on both triple quadrupole and linear ion trap platforms. We demonstrated that optimization of MS parameters on different instrument vendors and front ends, such as the position of the CBS tip regarding the MS inlet, is vital to exploit the full quantitative potential of this technology. Application of the

technology to screen and quantify fentanyl and analogues showed great potential when considering its coupling with portable mass spectrometers for therapeutic drug monitoring and point-of-care applications.

Contribution: First author. Responsible for all experiments and data processing. Worked with GAGR and VS on data interpretation. Prepared first draft of manuscript and was solely responsible for submission and revision of final accepted manuscript.

4. Chen, L., Singh, V., **Rickert, D.,** Khaled, A., & Pawliszyn, J. (2021). High throughput determination of free biogenic monoamines and their metabolites in urine using thin-film solid phase microextraction. *Talanta, 232, 122438.*

Abstract: UPLC-MS/MS methods are the gold standard for routine, high-throughput measurements of biogenic monoamines for the diagnosis of catecholamine-producing tumors. However, this cannot be achieved without employing efficient sample pretreatment methods. Therefore, two pretreatment methods, thin-film solid phase microextraction (TF-SPME) and packed fibers solid phase extraction (PFSPE), were developed and evaluated for the analysis of biogenic monoamines and their metabolites in urine. A hydrophilic-lipophilic balance (HLB) coating was chosen for the thin-film blade format SPME method and compared with a Polycrown ether (PCE) composite nanofiber used as an adsorbent for the PFSPE method. Under optimal conditions, the absolute extraction recovery and relative matrix effect of the newly developed TF-SPME method were determined to be 35.7–74.8% and 0.47–3.63%, respectively. The linearity was 0.25–500 ng mL^{-1} for norepinephrine, epinephrine, dopamine, normetanephrine 3-methoxytyramine, serotonin, histamine, and 0.1–500 ng mL^{-1} for metanephrine. The intra-and inter-assay coefficients of variation were 0.7–8.7%, and the respective accuracies were calculated to be 90.8–104.7% and 89.5–104.5% for TF-SPME. Compared with the PFSPE method, the TF-SPME method had a higher extraction efficiency, lower matrix effects and a wider linear range for eight target substances, which ensured higher accuracy of

simultaneous detection of all compounds of interest. Therefore, the proposed TF-SPME method can be employed for the high throughput screening for neuroendocrine tumors in a routine clinical setting and other relative research by simultaneous quantitation of urine eight biological monoamines in a single run.

Contribution: Assisted LC with design and execution of experiments. Assisted with preparation of the manuscript and subsequent revisions prior to acceptance by the journal.

5. Ieritano, C., **Rickert, D.,** Featherstone, J., Honek, J. F., Campbell, J. L., Blanc, J. Y. L., Schneider, B.B., & Hopkins, W. S. (2021). The charge-state and structural stability of peptides conferred by microsolvating environments in differential mobility spectrometry. *Journal of the American Society for Mass Spectrometry, 32(4), 956-968.*

Abstract: The presence of solvent vapor in a differential mobility spectrometry (DMS) cell creates a microsolvating environment that can mitigate complications associated with field-induced heating. In the case of peptides, the microsolvation of protonation sites results in a stabilization of charge density through localized solvent clustering, sheltering the ion from collisional activation. Seeding the DMS carrier gas (N_2) with a solvent vapor prevented nearly all field-induced fragmentation of the protonated peptides GGG, AAA, and the Lys-rich Polybia-MP1 (IDWKKLLDAAKQIL-NH_2). Modeling the microsolvation propensity of protonated *n*-propylamine $[PrNH_3]^+$, a mimic of the Lys side chain and N-terminus, with common gas-phase modifiers (H_2O, MeOH, EtOH, *i*PrOH, acetone, and MeCN) confirms that all solvent molecules form stable clusters at the site of protonation. Moreover, modeling populations of microsolvated clusters indicates that species containing protonated amine moieties exist as microsolvated species with one to six solvent ligands at all effective ion temperatures (T_{eff}) accessible during a DMS experiment (*ca.,* 375–600 K). Calculated T_{eff} of protonated GGG, AAA, and Polybia-MPI using a modified two-temperature theory approach were up to 86 K cooler in DMS environments seeded with solvent vapor compared to pure N_2 environments. Stabilizing effects were largely driven

by an increase in the ion's apparent collision cross section and by evaporative cooling processes induced by the dynamic evaporation/condensation cycles incurred in the presence of an oscillating electric separation field. When the microsolvating partner was a protic solvent, abstraction of a proton from $[MP1 + 3H]^{3+}$ to yield $[MP1 + 2H]^{2+}$ was observed. This result was attributed to the proclivity of protic solvents to form hydrogen-bond networks with enhanced gas-phase basicity. Collectively, microsolvation provides analytes with a solvent "air bag," whereby charge reduction and microsolvation-induced stabilization were shown to shelter peptides from the fragmentation induced by field heating and may play a role in preserving native-like ion configurations.

Contribution: Worked together with CI to collect and process all experimental data. Worked with CI to interpret experimental results. Assisted CI with first draft of the manuscript and helped with revisions prior to the final version being accepted by the journal.

6. **Rickert, D. A.,** Singh, V., Thirukumaran, M., Grandy, J. J., Belinato, J. R., Lashgari, M., & Pawliszyn, J. (2020). Comprehensive analysis of multiresidue pesticides from process water obtained from wastewater treatment facilities using solid-phase microextraction. *Environmental Science & Technology*, *54(24), 15789-15799.*

Abstract: A novel magnetic blade spray–tandem mass spectrometry (MBS-MS/MS) assay was developed and optimized, and its performance was characterized for the analysis of 204 pesticides from wastewater treatment facility (WWTF) process water. These results were compared and experimentally validated with an untargeted, high-resolution MS (HRMS) approach that employed liquid chromatography (LC)-amenable thin-film microextraction (TFME) devices to further elucidate the fate of pesticides through the WWTF process. As a result of our optimizations, we report an optimized workflow with an extraction time of 10 min, 150 μg of magnetic HLB particles, and 5 s of desorption. Excellent linearity was obtained for 168 of the 204 pesticides in deionized water, where 90% of the

quantifiable pesticides had a determination coefficient (R^2) of 0.99 across 3 orders of magnitude and 80% had limits of quantification below 0.5 ng/mL. We subsequently applied our optimized MBS-MS/MS method for the analysis of samples collected during the various stages of wastewater treatment from two WWTFs in Southern Ontario. This article presents a new streamlined methodology with a fast turnaround time for analyzing a large panel of pesticides, ultimately providing us the opportunity to evaluate the performance of two WWTFs for their efficacy in removing these toxic chemicals.

Contribution: Equal contribution first author. Responsible for all experiments and data processing along with VS and MT. Interpretation of results along with VS and MT. Wrote first draft of manuscript, and incorporated edits and revisions by other coauthors prior to submission. Revised manuscript and prepared final version that was accepted by the journal.

Appendix B: Sample .cfg File

```
# MIPS Control Panel configuration file example.
# All the lines that start with # are comments.
#
# The following command sets the size of your control panel in pixels.
# This should be the first command in the config file.
size,1500,900
# Load the background image. I have commented this like out because the path
# will likely be different on your system and you will need an image specific
# to you syste.
image,/Users/pftimsmain/MIPS/PFTIMS.jpg
# Help file for this custom control panel
Help,/Users/GAA/GAACE/Products/MIPS/MIPSapp/MIPS/ExampleHelp.txt
# Text labels
TextLabel,PFTIMS,24,680,10
# The following command enables the system shutdown button
Shutdown,System shutdown,20,50
#TCPserver,9999
# Save and load methods buttons
SaveLoad,Save method,Load method,20,90
# Enable MIPS communication button
MIPScomms,20,170
# Enable Script
Script,20,210

# Define the RF channels
RFchannel,RF F1,MIPS-2,1,350,650
RFchannel,RF F2,MIPS-2,2,1280,110

ESIchannel,ESI,MIPS-2,1,10,470

DCBchannel,Inlet,MIPS-2,4,150,315

TextLabel,Funnel #1,14,220,340
DCBchannel,F1in,MIPS-2,9,150,360
DCBchannel,F1out,MIPS-2,10,150,380
DCBchannel,F1cl,MIPS-2,11,150,400

TextLabel,Sector #4,14,1100,110
DCBchannel,TubeLens,MIPS-1,1,1030,130
DCBchannel,CH 33,MIPS-1,2,1030,150
DCBchannel,CH 32,MIPS-1,3,1030,170
DCBchannel,CH 31,MIPS-1,4,1030,190
DCBchannel,CH 30,MIPS-1,5,1030,210
DCBchannel,CH 29,MIPS-1,6,1030,230
DCBchannel,CH 28,MIPS-1,7,1030,250
DCBchannel,CH 27,MIPS-1,8,1030,270
DCBchannel,CH 26,MIPS-1,9,1030,290

TextLabel,Sector #3,14,800,110
DCBchannel,CH 25,MIPS-1,10,730,130
DCBchannel,CH 24,MIPS-1,11,730,150
DCBchannel,CH 23,MIPS-1,12,730,170
DCBchannel,CH 22,MIPS-1,13,730,190
DCBchannel,CH 21,MIPS-1,14,730,210
DCBchannel,CH 20,MIPS-1,15,730,230
DCBchannel,CH 19,MIPS-1,16,730,250
DCBchannel,CH 18,MIPS-1,17,730,270
```

```
TextLabel,Sector #2,14,950,590
DCBchannel,CH 17,MIPS-1,18,880,610
DCBchannel,CH 16,MIPS-1,19,880,630
DCBchannel,CH 15,MIPS-1,20,880,650
DCBchannel,CH 14,MIPS-1,21,880,670
DCBchannel,CH 13,MIPS-1,22,880,690
DCBchannel,CH 12,MIPS-1,23,880,710
DCBchannel,CH 11,MIPS-1,24,880,730
DCBchannel,CH 10,MIPS-1,25,880,750

TextLabel,Sector #1,14,650,590
DCBchannel,CH 9,MIPS-1,26,580,610
DCBchannel,CH 8,MIPS-1,27,580,630
DCBchannel,CH 7,MIPS-1,28,580,650
DCBchannel,CH 6,MIPS-1,29,580,670
DCBchannel,CH 5,MIPS-1,30,580,690
DCBchannel,CH 4,MIPS-1,31,580,710
DCBchannel,CH 3,MIPS-1,32,580,730
DCBchannel,CH 2,MIPS-2,1,580,750
DCBchannel,CH 1,MIPS-2,2,580,770

TextLabel,Funnel #2,14,1250,590
DCBchannel,F2in,MIPS-2,12,1180,610
DCBchannel,F2out,MIPS-2,13,1180,630
DCBchannel,F2cl,MIPS-2,14,1180,650
DCBchannel,Grid,MIPS-2,15,1180,670

TextLabel,MIPS-1 offsets,14,120,680
DCBoffset,CH27-TL,MIPS-1,1,50,700
DCBoffset,CH19-26,MIPS-1,9,50,720
DCBoffset,CH11-18,MIPS-1,17,50,740
DCBoffset,CH3-10,MIPS-1,25,50,760

TextLabel,MIPS-2 offsets,14,120,780
DCBoffset,CH1-8_MIPS2,MIPS-2,1,50,800
DCBoffset,CH9-16_MIPS2,MIPS-2,9,50,820

# ADCchannel,Det,MIPS-2,0,1180,770,1.70,0,pA,%.1f
Ccontrol,Det,Det,LineEdit,,Ion current,,pA,1180,770
ScriptButton,Plot,Plot.scrpt,1180,800
ScriptButton,Load,Load.scrpt,1180,830
ScriptButton,Update,Update.scrpt,1180,1000
CallOnUpdate,TRUE

# Set channel values
GroupBox,Set values,180,135,450,20
Ccontrol,Start CH,Set,LineEdit,,Start channel,,,20,25,String
Ccontrol,Stop CH,Set,LineEdit,,Stop channel,,,20,45
Ccontrol,Start V,Set,LineEdit,,Start voltage,,,20,65
Ccontrol,Stop V,Set,LineEdit,,Stop voltage,,,20,85
ScriptButton,Fill,Fill.scrpt,20,105
GroupBoxEnd
```

```
# Generate ramp
GroupBox,Ramp,180,175,450,150
Ccontrol,Start CH,Set,LineEdit,,Start channel,,,20,25,String
Ccontrol,Stop CH,Set,LineEdit,,Stop channel,,,20,45
Ccontrol,Start V,Set,LineEdit,,Start voltage,,,20,65
Ccontrol,Stop V,Set,LineEdit,,Stop voltage,,,20,85
Ccontrol,Steps,Number,LineEdit,,of steps,,,20,105
Ccontrol,Dwell,Dwell,LineEdit,,time in mS,,,20,125
ScriptButton,Generate,Generate.scrpt,20,145
GroupBoxEnd


# Plotting function
GroupBox,Sweep,180,290,200,20
Ccontrol,Param,Sweep,LineEdit,,Parameter name,,,20,25,String
Ccontrol,Start,Sweep,LineEdit,,Start value,,,20,45
Ccontrol,Stop,Sweep,LineEdit,,Stop value,,,20,65
Ccontrol,Step,Sweep,LineEdit,,Step size,,,20,85
GroupBox,At each step,160,140,10,105
Ccontrol,Enable,At each step,CheckBox,,,,,10,25
Ccontrol,Param,At each step,LineEdit,,Parameter name,,,10,45,String
Ccontrol,Start,At each step,LineEdit,,Start value,,,10,65
Ccontrol,Stop,At each step,LineEdit,,Stop value,,,10,85
Ccontrol,Step,At each step,LineEdit,,Step size,,,10,105
GroupBoxEnd
ScriptButton,Start,Sweep.scrpt,15,250
GroupBoxEnd


#Send setup command to MIPS-2 for the ADC averaging
SendCommand,MIPS-2,ADCABORT
SendCommand,MIPS-2,SADCSAMPS,1000
SendCommand,MIPS-2,ADCCHG,0,100


# Define the DIO channels
DIOchannel,DIO A-1,MIPS-1,A,20,250
DIOchannel,DIO B-1,MIPS-1,B,20,280
DIOchannel,DIO A-2,MIPS-2,A,20,310
DIOchannel,DIO B-2,MIPS-2,B,20,340
# Initial parameters file. This ini file contains a list of MIPS commands that
# you can use to perform startup initialization.
#InitParms,/Users/GAA/GAACE/Products/MIPS/MIPSapp/MIPS/Initalize.ini
TIMING,TG MIPS-1,MIPS-1,20,520
TIMING,TG MIPS-2,MIPS-2,200,520
```

Appendix C: Standard Operating Procedure for MIPS Ramp Script

On the control panel, *set values* (at the top) works by simply inputting the channel number for the start and stop CH. This defines the initial gradient across the mobility region. Example of a 5V to 25V gradient from channel 18 to 25 (sector 3):

Start: CH 18

Stop: CH 25

Start: V 5

Stop: V 2

Ramp needs to have some values inputted in reverse order to correct for the DC wiring problem that was been corrected in the .cfg file. Example of a 5V to 6V final gradient (after the ramp script has run from channel 18 to 25 (sector 3)):

Start: CH 25

Stop: CH 18

Start: V 6

Stop: V 5

Steps: 15

Dwell: 10

Use the TG MIPS1 to specify the timing parameters that are part of the generate.scrpt functionality.

Event editor:

- The ramp event must be named Ramp.

- No signal channel is defined. All voltages and channels that are part of the ramp event is done using the Ramp box at the top of the control panel.
- Start – this is the delay time after MIPS1 gets the trigger signal from MIPS2 to start ramping down the voltages across the specified channels.
- Width – This is the time from the start of the trigger signal from MIPS2 to the point when the MIPS resets the voltages to the original gradient and prepares for the next accumulation event.
- Value – leave this set to 0.
- Value, off – leave this set to 0.

Frame Parameters:

- Start – this should be set to 0 so that it starts as soon as it receives the trigger signal from MIPS2.
- Width – this must be larger than the width in the event editor, but shorter than the width defined in MIPS2. MIPS1 is the slave and MIPS 2 is the master that defines the triggers. MIPS1 is running specific events with triggers defined by MIPS2.
- Accumulations – set to 1. Only 1 ramp event occurs per trigger signal from MIPS2.

Time mode needs to be checked, external clock frequency set to 6135, clock source 656250.

MIPS1 (which runs the ramp) will have a trigger source of Pos (accept the trigger from MIPS2), and MIPS2 trigger source will be set to software.

MIPS2 will have two trigger events – one will trigger the scope to start collecting data, and the other will trigger MIPS1. These both have the exact same time settings except for the signal channel. The scope trigger uses DIO-A2, and the trigger from MIPS2 to MIPS1 uses DIO-B2.

How to run the ramp script:

1. Define the initial gradient using set values.
2. Set the ramp values using the provisios mentioned above.
3. Press generate button. MIPS1 will enter table mode and wait for trigger signal from MIPS2.

4. Press trigger on MIPS2 to initiate the sequence.

Appendix D: COMSOL Modelling Details – Gas Dynamics

Table 4. Summary of COMSOL Multiphysics input parameters for gas dynamics simulations.

Model Wizard	
2D	
Single Phase Flow/Laminar Flow	
Time-dependent Study	
Parameters	
T; Temperature	293.15 K
Laminar Flow	
Initial condition; bulk pressure*	3.0 Torr
Inlet; pressure controlled	3.0 Torr
Outlet; pressure controlled	1.5 Torr
Wall	Slip condition
Material	
Bulk material	Nitrogen
Mesh	
Physics controlled	
Fine	
Density	
Material controlled	
Dynamic viscosity	
Material controlled	

The model was built using the COMSOL Multiphysics wizard tool. Table 3 summarizes the parameters modified after creating a model using the wizard: 2D, single phase flow > laminar flow; and time dependent study. Bulk material density and viscosity are taken from default values. *With funnel attached, the inlet condition is set at the funnel entrance, otherwise and the mobility region entrance boundary.

Appendix E: COMSOL Modelling Details – Electric Fields

Table 5. Summary of COMSOL Multiphysics input parameters for electric field simulations.

Model Wizard	
2D	
Electric Fields and Currents/Electric Currents	
Time-dependent study	
Parameters	
V; peak-to-peak voltage	100 V
ω; Frequency	750 kHz
Variables	
Positive radio frequency	RF (+) = V sin(ωt)
Negative radio frequency	RF (–) = – V sin(ωt)
Materials	
Electrodes	Stainless steel
Bulk medium	Perfect vacuum
Mesh	
Physics controlled	
Fine	

The model was built using the COMSOL Multiphysics wizard tool. Table 4 summarizes the parameters that have been modified from COMSOL Wizard tool using 2D geometry; electric fields and currents > electric currents, and a time-dependent study.

Appendix F: Detailed Electronics Summary